

SYNTHETIC APERTURE LADAR TECHNIQUES

by

Stephen Capdepon Crouch

A thesis submitted in partial fulfillment  
of the requirements for the degree

of

Masters of Science

in

Physics

MONTANA STATE UNIVERSITY  
Bozeman, Montana

July 2012

©COPYRIGHT

by

Stephen Capdepon Crouch

2012

All Rights Reserved

APPROVAL

of a thesis submitted by

Stephen Capdepon Crouch

This thesis has been read by each member of the thesis committee and has been found to be satisfactory regarding content, English usage, format, citation, bibliographic style, and consistency and is ready for submission to The Graduate School.

Dr. Randy Babbitt

Approved for the Department of Physics

Dr. Dick Smith

Approved for The Graduate School

Dr. Carl A. Fox

STATEMENT OF PERMISSION TO USE

In presenting this thesis in partial fulfillment of the requirements for a master's degree at Montana State University, I agree that the Library shall make it available to borrowers under rules of the Library.

If I have indicated my intention to copyright this thesis by including a copyright notice page, copying is allowable only for scholarly purposes, consistent with "fair use" as prescribed in the U.S. Copyright Law. Requests for permission for extended quotation from or reproduction of this thesis in whole or in parts may be granted only by the copyright holder.

Stephen Capdepon Crouch

July 2012

## ACKNOWLEDGMENTS

I would like to acknowledge Zeb Barber for freely sharing his expertise and for his patience in working with me on this fascinating topic. I would also like to thank the rest of the folks at Spectrum Lab: Randy Babbitt, Jason Dahl, Cal Harrington, Tia Sharpe, Sue Martin, Christoffer Renner, Krishna Rupavatharam, Warren Coulomb, Cooper McCann, and Ana Baselga, for their help in all aspects. The previous work on SAL by Bridger Photonics should also be acknowledged. I would like to thank Margaret Jarrett and Sarah Barutha for their help in navigating much more than just paperwork. To my classmates in MSU physics, Chat Chantjaroen, Orion Bellorado, Ben Rosemeyer, Frank Borawski, Bret Davis, and Mark Stalnaker for their friendship.

On the home-front, tack till Märtha Welander - världens bästa.

## TABLE OF CONTENTS

1. INTRODUCTION .....	1
Background .....	1
Motivation.....	2
Outline.....	3
2. MATHEMATICAL PRELIMINARIES.....	4
Overview .....	4
Common Functions in SAL Theory.....	4
Signal Processing Operations .....	6
Discrete Implementation.....	7
Signal Analysis Examples.....	8
Windowing Example.....	8
Convolution Theorem Example.....	9
3. CHIRP RANGING .....	11
Overview .....	11
What Is a Chirp? .....	11
Mathematical Description of Heterodyne Beat Detection.....	12
Chirp Linearization .....	14
Range Resolution.....	16
Description of CR System .....	17
Laser Source.....	17
Fiber Set-Up.....	18
Auto-Balance Detector.....	20
4. SYNTHETIC APERTURE LADAR BASICS .....	21
History and Philosophy.....	21
Photon Budget.....	21
Collection Geometry.....	24
Various Fundamentals.....	27
Derivation of Fourier Relationship .....	27
Tomographic .....	29
Cross Range Resolution Derivation.....	30
Fourier Optics Explanation.....	31
Analysis of the Angular Spectrum Approach.....	32
Experimental Set Up.....	33

## TABLE OF CONTENTS - CONTINUED

Aperture Stepper Stage .....	33
Dimensions .....	34
Optical Power .....	34
Sample Rate .....	36
HCN Cell .....	36
MATLAB Code Description .....	37
Previous Experimental Set-Up Variations .....	38
Phase Error.....	39
Effects .....	40
Piston Error.....	40
Inconsistent Stepping Analysis .....	42
Twisting Error .....	43
Polar Formatting and Quadratic Phase Errors .....	44
Residual Phase Error.....	45
Phase Error Correction.....	46
Phase to Retro Algorithm.....	46
Phase Gradient Autofocus.....	47
Text Book.....	48
Point Spread Function.....	50
5. SAL RESULTS .....	51
An Early SAL Image.....	51
The Dragonfly.....	52
PGA Success .....	53
Correction of Large Phase Errors .....	53
Further Processing .....	54
Electronic Chip .....	57
Discussion .....	58
6. INTERFEROMETRIC SAL.....	59
History and Introduction.....	59
IFSAL Geometry.....	59
Textbook Explanation.....	60
Zero-Phase Plane Model.....	60
Collection Set-Up .....	62
Two Pass .....	62
One Pass with Fiber Array .....	63
Scene Background .....	64
Post-Processing and MATLAB Code .....	65

## TABLE OF CONTENTS - CONTINUED

""Image Registration.....	65
""Two Dimensional Phase Unwrapping.....	66
""Least Squares ....0.....	67
""Network Flow .....	67
""Flat Earth Effect.....	68
""Baseline Considerations.....	68
7. IFSAL RESULTS.....	70
Two Pass vs. One pass .....	70
Target Considerations .....	70
Registration of SAL Images for Interference.....	71
Lincoln Penny Results .....	71
Multilook IFSAL Processing .....	72
IFSAL Unwrap Methods Results.....	72
Least Squares IFSAL Unwrap Result .....	73
Network Flow IFSAL Unwrap Result .....	74
Sea Shell Result .....	75
Discussion .....	77
8. PROJECTIVE SAL .....	78
PSAL Concept.....	78
SAL Images as Projections .....	78
Surface Reconstruction from Projections .....	79
Proof of Concept.....	80
Collection Geometry.....	81
MATLAB Code.....	82
Result of Toothpick Demo .....	82
9. SPOTLIGHT SAL .....	84
Overview.....	84
Considerations.....	88
Sampling .....	88
Polar Formatting .....	88
Spotlight Cross Range Resolution .....	88
Photon Budget.....	89
Polar Format Implementation .....	90
Spotlight Mode Experiment.....	92
Spotlight Collection Mechanics .....	92

TABLE OF CONTENTS - CONTINUED

MATLAB Code Used .....	95
Spotlight Results .....	95
10. CONCLUSION.....	98
Successes.....	98
Shortcomings .....	98
Prospects for SAL .....	99
REFERENCES .....	100
APPENDIX A: MATLAB CODE.....	104

## LIST OF FIGURES

Figure		Page
1	Windowing Example.....	9
2	Convolution Example .....	10
3	Chirp .....	12
4	Chirp/Beat .....	14
5	Effect of Poor Chirp.....	15
6	Chirp Linearization.....	18
7	Circulator Vs Fiber Array .....	19
8	SAL Geometry .....	25
9	Overhead Photo.....	25
10	Stripmap Vs Spotlight.....	26
11	Angular Spectrum Idea .....	32
12	Experimental Setup Photo and Schematic .....	35
13	HCN Data.....	37
14	Piston Error .....	41
15	Step Error .....	42
16	Twist Error .....	44
17	Smiley Image .....	51
18	MSU Lapel Pin .....	52
19	Unfocused Dragonfly.....	54
20	Phase Error.....	55

## LIST OF FIGURES

Figure	Page
21 Associated PSF .....	55
22 Dragonfly .....	56
23 RAM Chip.....	57
24 ZPP .....	61
25 Set Up with Fiber Array .....	614
26 Penny Image and Interference Pattern .....	72
27 Least Squares Unwrapped.....	73
28 Network Flow Unwrapped.....	74
29 Sea Shell Photo .....	76
30 Sea Shell Unwrapped.....	77
31 PSAL A .....	79
32 PSAL B .....	80
33 PSAL Photo.....	81
34 PSAL Result.....	83
35 STRIPMAP VS SPOTLIGHT .....	84
36 Stripmap/Bistatic Geometry.....	86
37 Photon Budget.....	90
38 Spotlight Mechanics.....	93
39 Spotlight Photos .....	94
40 Bar Target Results.....	96

LIST OF FIGURES

Figure	Page
41 RAM Chip Spotlight.....	97

## ABSTRACT

Synthetic Aperture Ladar (SAL) system performance is generally limited by the chirp ranging sub-system. Use of a high bandwidth linearized chirp laser centered at 1.55 microns enables high resolution ranging. Application of Phase Gradient Autofocus (PGA) to high resolution, stripmap mode SAL images and the first demonstration of Interferometric SAL (IFSAL) for topography mapping are shown in a laboratory setup with cross range resolution commensurate with the high range resolution. Projective SAL imaging is demonstrated as a proof of concept. Finally spotlight mode SAL in monostatic and bistatic configurations is explored.

## INTRODUCTION

### Background

Synthetic Aperture Ladar (SAL) is a coherent measurement technique mathematically identical to Synthetic Aperture Radar (SAR) but operating at optical frequencies which are at least three orders of magnitude higher than those of cutting edge SAR systems. SAL produces complex, two-dimensional images of scene reflectivity via coherent sampling in range (parallel to beam) and cross range (perpendicular to beam). Range sampling is often performed via linear chirp waveforms and requires targets with range diversity. Cross range sampling requires a set of range records with angular diversity achieved by recording the range profile to the scene from points along a track – the synthetic aperture. Ranging acts as a phase measurement and the synthetic aperture synthesis tracks the evolution of this phase. The synthesis of information in range and cross range axes results in a coherent history of the scene that is related to the image under ideal conditions by the two dimensional Fourier Transform.

SAR was first proposed in June of 1951 by Carl Wiley as a means to improve cross range resolution in radar imaging systems [1]. Since its inception, SAR systems improvement has represented a major research effort in geophysical (and extraterrestrial) mapping science and the defense industry [1,2]. In the case of radar systems, a synthetic aperture system onboard an aircraft can deliver cross range resolution that would require a real antenna aperture of several kilometers –not a feasible engineering requirement. Synthetic aperture imaging only offers a means to improve the cross range resolution [1].

Therefore the design of a synthetic aperture system with the best angular resolution invites high resolution ranging methods.

Experimental groups successfully demonstrated SAL as early as 2002 [3]. Early SAL experiments were greatly limited by laser chirp nonlinearities. Complicated resampling algorithms were employed to correct for these detrimental effects. When Bridger Photonics and Spectrum Lab introduced their broad bandwidth linear chirp laser source with application to spectral hole burning experiments, Ladar applications such as SAL were recognized [4].

### Motivation

Ladar chirp ranging has experienced success in other applications. Range finding is the most basic application of chirp ranging. A more advanced example is the use of range measurements in rastering setups to produce surface profiles of small targets. Surface profiles of custom contact lenses on the order of tens of microns were produced with the same ranging system used in this research. The historical success of SAR coupled with the promise of Ladar is the basis of research interest in SAL. Despite the previous research in SAL, several motivating questions remained. How robust is the Phase Gradient Autofocus (PGA) algorithm in dealing with phase errors? Are the registration and phase coherence requirements of interferometric synthetic imaging too large to demonstrate the technique in the optical regime? What are the power requirements of high resolution imaging? These and other questions needed to be answered to start to understand SAL's role in Ladar imaging.

The stated goal of the project funding the work contained in this thesis is, “To use the very high resolution and accuracy ranging provided by these ultra-broadband chirped laser sources to demonstrate a novel method of high resolution 3D part inspection and accurate large scale 3D metrology.” [5] This investigation of SAL has focused on understanding the uses and shortcomings of the technique from as many perspectives as possible with a broader 3D metrology system in mind.

### Outline

The second chapter includes mathematical preliminaries that will be vital to a discussion of SAL. The third chapter introduces chirp ranging Ladar (“Laser Radar”) – the fundamental tool that facilitates SAL imaging. The fourth and fifth chapters describe SAL from theoretical and experimental perspectives, respectively. The sixth and seventh chapters deal with Interferometric SAL from theoretical and experimental perspectives. The eighth chapter demonstrates, as proof of concept, Projective SAL imaging and the role of SAL in a broader three dimensional metrology system. The ninth explores the advantages and difficulties of spotlight mode SAL. The tenth chapter is the conclusion.

The vast majority of the literature and processing techniques pertaining to the work in this thesis come from the SAR community. This research area has naturally developed its own description and lingo for synthetic aperture theory. In some cases, this will be the avenue of choice when discussing SAL. In other instances, models developed in the course of this study and techniques from Fourier optics are more effective.

## MATHEMATICAL PRELIMINARIES

### Overview

A thorough understanding of SAL hinges on several mathematical techniques used to describe the image formation process. A quick review of mathematical operations and their discrete counterparts helps to ensure a more cohesive discussion in subsequent chapters. This chapter serves to set notation to prevent downstream confusion. Specific SAL concepts are not explored here but points of contact to downstream discussion are made.

SAL demands an understanding of basic signal processing operations. Fourier analysis is indispensable in both the theoretical description and experimental post processing. The Taylor expansion is required to approximate complicated models into more workable forms. SAL processing requires working with both one and two dimensional data sets so definitions extend to both cases where applicable. Latin letters describe spatial coordinates while corresponding Greek letters describe the frequency domain coordinates.

### Common Functions in SAL Theory

A complex signal  $E$  can be separated into magnitude,  $E_0$ , and phase,  $\phi$ , components as in Equation 2.1. A SAL image is a two dimensional, complex data set.

$$E = E_0 e^{i\phi} \quad (2.1)$$

The Dirac delta function  $\delta(u - u')$  is nonzero for  $u = u'$ . Integrating the delta function over an interval containing  $u'$  gives unity. This can be extended to three dimensions by considering,  $\delta(u - u', v - v', w - w') = \delta(u - u')\delta(v - v')\delta(w - w')$ . For simplicity, most SAL models are derived using a single point scatterer best described as a delta function.

The comb function is defined as an infinite train of delta functions [6]. This turns out to be a convenient way to represent, after limiting the summation, the discrete sampling of a signal.

$$comb(u) = \sum_{n=-\infty}^{\infty} \delta(u - n) \quad (2.2)$$

Harmonic functions have the form of Equation 2.3 describing a linear evolution of the phase as a function of position [6].

$$\psi_{har} = e^{i2\pi u} \quad (2.3)$$

Chirp functions have the form of Equation 2.4 describing quadratic phase evolution [6].

$$\psi_{chirp} = e^{i\pi u^2} \quad (2.4)$$

The form of a Gaussian function peaked at a point  $a$  is defined in Equation 2.5 where  $\sigma$  is a width parameter [7].

$$\psi_{Gauss} = e^{-(u-a)^2 / 2\sigma^2} \quad (2.5)$$

The rectangle function, defined in Equation 2.6, is useful to describe hard cutoffs

for signals or sampling [7].

$$\text{rect}(u) = \left\{ \begin{array}{l} 1, |u| < \frac{1}{2} \\ 0, \text{else} \end{array} \right\} \quad (2.6)$$

### Signal Processing Operations

A handful of operations and their respective relationships constitute the bedrock of Fourier signal analysis. Below several forms are defined for these operations so that derivations of SAL models may make contact with these forms so as to justify signal manipulations with the discrete version of these operations.

Convolution is defined in Equation 2.7. The convolution of two functions is denoted by the (\*) symbol. The convolution integral describes the inner product of two functions as one of the functions is shifted through all possible locations relative to the other function [7].

$$f(u) * g(u) = \int_{-\infty}^{\infty} f(u')g(u-u')du' \quad (2.7)$$

The complex Fourier transform of a function  $f(u)$  is defined, along with its inverse [7]. The Fourier transform is a linear decomposition of a signal into its inherent frequency components with a phase associated with each harmonic component with the form of Equation 2.3. The Fourier transform of a real signal is therefore, in general, complex. The character  $\mathfrak{F}^a$  will denote the Fourier transform with  $a=1$  and the inverse transform with  $a=-1$ .

$$\mathfrak{F}^1 \{f(u)\} = \int_{-\infty}^{\infty} f(u)e^{-i2\pi u\mu} du = F(\mu) \quad (2.8)$$

$$\mathfrak{F}^{-1}\{F(\mu)\} = \int_{-\infty}^{\infty} F(\mu)e^{i2\pi u\mu} d\mu = f(u) \quad (2.9)$$

The Fourier transform is related to convolution via the convolution theorem [7].

$$f(u) * g(u) \xleftrightarrow[\mathfrak{F}^{-1}]{\mathfrak{F}^!} F(\mu)G(\mu) \quad (2.10)$$

The two-dimensional analog of Equations 2.7, 2.8, and 2.10 is also defined [7].

Note the use of (\*\*) to denote two dimensional convolution. Also, note the use of subscript 2 in  $\mathfrak{F}_2^!$  to denote the two dimensional Fourier transform.

$$f(u, v) ** g(u, v) = \int_{-\infty}^{\infty} \int_{-\infty}^{\infty} f(u', v') g(u - u', v - v') du' dv' \quad (2.11)$$

$$\mathfrak{F}_2^!\{f(u, v)\} = \int_{-\infty}^{\infty} \int_{-\infty}^{\infty} f(u, v) e^{-2\pi i(u\mu + v\nu)} dudv = F(\mu, \nu) \quad (2.12)$$

$$f(u, v) ** g(u, v) \xleftrightarrow[\mathfrak{F}_2^{-1}]{\mathfrak{F}_2^!} F(\mu, \nu)G(\mu, \nu) \quad (2.13)$$

The Taylor expansion of a function about a point  $a$  is defined in Equation 2.14 [8].

This does not pertain specifically to the above layout of Fourier analysis but it will be useful in making contact with the above forms, among other derivations.

$$f(u) \approx f(a) + (u - a)f'(a) + \frac{(u - a)^2}{2!} f''(a) + \dots \quad (2.14)$$

### Discrete Implementation

While the above expressions will prove helpful in connecting the SAL model with practical application, the above operations are not useful unless they are available in a discrete sense on the computer. MATLAB was the mathematical software supporting the

processing in this thesis. MATLAB is able to process complex numbers. A standard function library supports the discrete Fast Fourier Transform algorithm (FFT). MATLAB also has functions supporting convolution, windowing, and curve fitting that will be mentioned as used.

### Signal Analysis Examples

A study of Fourier signal analysis is not at the onset wholly intuitive. A few examples will help to reinforce the notions of time and frequency spaces as well as display the utility of MATLAB in the study of this topic. The examples below utilize MATLAB to create the figures in much the same way SAL image formation takes place.

#### Windowing Example

Windowing a signal is one way to mitigate unwanted effects of discrete and finite signal analysis. The FFT of a finite signal will often produce “side-lobes”. Side-lobes represent frequency content away from a central peak that arise due to edges in the signal caused by its finite nature. Applying a proper windowing function to the finite signal gradually weakens the signal near the edges and acts to suppress these sharp edges and associated side-lobes. The cost of this operation is a broadened central lobe. The Hanning window function, Equation 2.15, used in Figure 1 is very similar in shape to a Gaussian and is commonly used in signal processing. MATLAB has a Hanning window function in its library [9].

$$hanning(n) = \frac{1}{2} \left[ 1 - \cos\left(2\pi \frac{n}{N}\right) \right], 0 \leq n \leq N \quad (2.15)$$

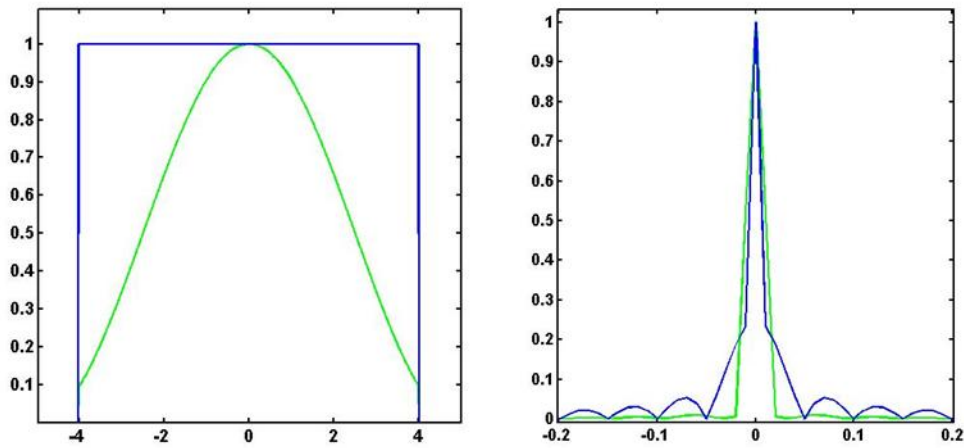


Figure 1: Windowing Example At left a rect function in blue and the product of the rect function and Hanning Window in green. At right, the magnitude of the FFT of the rect function in blue and the FFT of the window/rect product function in green.

### Convolution Theorem Example

The convolution theorem is central to understanding the generation and removal of various errors in SAL image formation. Figure 2 shows a signal consisting of two time/spatial domain delta functions in green overlaid with a degraded version of the signal where the degradation can be viewed as a windowing of the frequency content of the delta functions with the rect function. Such a frequency/spatial-frequency domain windowing function is in general known as a transfer function denoted by  $H$ .

Alternatively, and perhaps easier to “see”, one can regard the blurring as the convolution of the FFT of the rect window with the two delta functions. This time/spatial domain “blurring” function is known as an impulse response or point spread function denoted by  $h$ . The point spread function  $h$  is related to  $H$  by the FFT. The blurred delta functions in blue were produced by taking the product of the box transfer function with the FFT of the delta functions and inverse transforming. This result is equivalent to the

convolution of the delta function signals with the impulse response function. This demonstrates the utility of the convolution theorem.

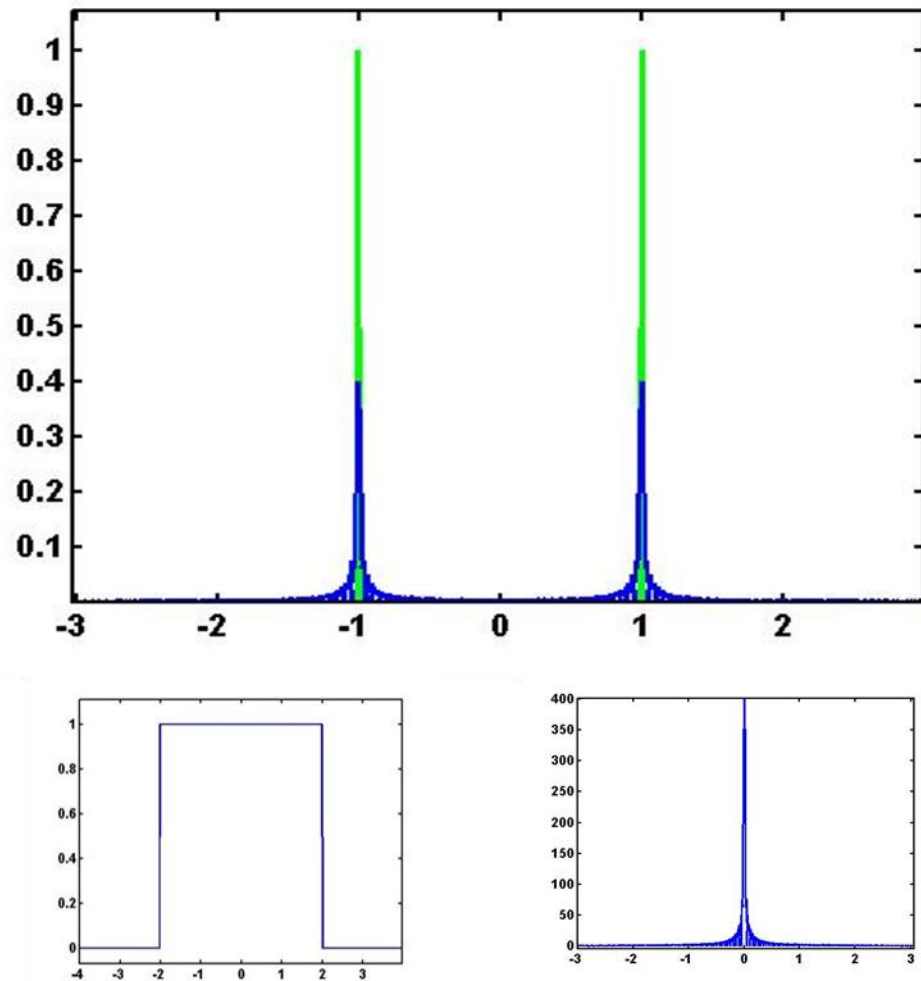


Figure 2: Convolution Example At top a signal consisting of two delta functions in green and the signal degraded with the rect transfer function in blue. Bottom left shows the rect transfer function and bottom right shows the magnitude of the FFT of the rect transfer function (also known as the “impulse response” or “point spread” function).

## CHIRP RANGING

### Overview

The tool that facilitates the study of SAL in this thesis is a Ladar chirp ranging (CR) system. CR systems are not the only way to implement SAL. Pulsed methods and advanced coded signal methods have also been effectively demonstrated [10]. However, CR systems have certain advantages - chiefly reduced peak laser power output and reduced sampling bandwidth requirements. A time of flight pulsed system would require a sampling bandwidth on the order of THz to realize the same range resolution of the CR system described below. Therefore, CR systems are the most effective way to achieve high resolution without high bandwidth sampling [2].

### What Is a Chirp?

CR systems rely on a highly linear “chirp” or change in the frequency of the output laser light with respect to time. A chirp in the visual part of the electromagnetic spectrum would appear as a steady change of colors across the spectrum of the rainbow. As derived below, the chirp itself is essentially a way of encoding information in a signal that can be used to extract information from the return signal.

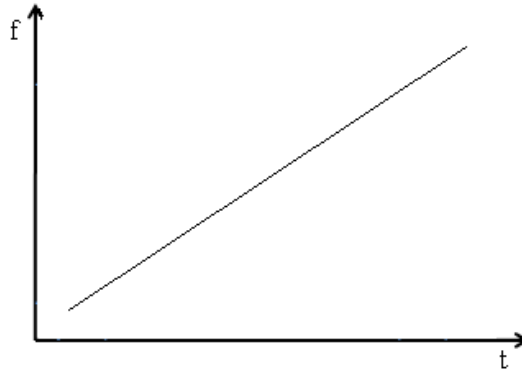


Figure 3: Chirp A graphic reinforcing the linear increase of frequency versus time of chirps.

### Mathematical Description of Heterodyne Beat Detection

A model of a CR system examines the signal of interest in the context of its phase evolution. A complex exponential function is used for this task. In the CR system in use, the return signal  $E_{signal}$  is optically mixed with a local oscillator (LO) path signal,  $E_{LO}$ . This creates a beat note containing target range information that depends on the range dependent time delay  $\tau$  and the chirp rate  $\kappa$ . The optical mixing is described mathematically as complex conjugate multiplication of the two complex exponential functions. The return signal from the target is described using a time delay  $\tau$  that is introduced to describe the difference in time of flight to and from the target versus the LO path.

The delay is related to the range by Equation 3.1.

$$\tau = \frac{2R}{c} \quad (3.1)$$

The LO is described by 3.2. The proportionality sign avoids the question of magnitude in considering these signals, which will be studied in the next chapter in the context of the SAL photon budget.

$$E_{LO} \propto \exp[-i(\omega t + \frac{1}{2} \kappa t^2)] \quad (3.2)$$

The signal is described by 3.3.

$$\begin{aligned} E_{signal} &\propto \exp\{-i[\omega(t - \tau) + \frac{1}{2} \kappa(t - \tau)^2]\} \\ &\propto \exp\{-i[\omega t - \omega\tau + \frac{\kappa t^2}{2} - \kappa t\tau + \frac{\kappa\tau^2}{2}]\} \end{aligned} \quad (3.3)$$

The mixing process is described by Equation 3.4. The two terms  $\omega t$  and  $\frac{\kappa t^2}{2}$  exactly cancel. For the basis of comparison, relative magnitudes of terms are  $\kappa = 10\text{THz}/\text{sec}$ ,  $\omega \sim 10^{15}$ , and  $\tau \sim 1\text{ns}$ . By comparing the terms in 3.3 ( $\kappa t\tau \sim 0 \rightarrow 10000$ ,  $\omega\tau \sim 10000$ , and  $\frac{\kappa\tau^2}{2} \sim .0001$ ),  $\frac{\kappa\tau^2}{2}$  is therefore small and can be ignored. This yields the approximation in Equation 3.4 where only a linear dependence of phase on time delay remains.

$$\begin{aligned} E_{LO} E_{signal}^* &\propto \exp[-i(\omega t + \frac{\kappa t^2}{2})] \exp\{i[\omega t - \omega\tau + \frac{\kappa t^2}{2} - \kappa t\tau + \frac{\kappa\tau^2}{2}]\} \\ &\approx \exp[-i(\omega\tau + \kappa t\tau)] \end{aligned} \quad (3.4)$$

Equation 3.1 is substituted into Equation 3.4 to yield Equation 3.5.

$$E_{LO} E_{signal}^* \propto \exp[-i(\frac{2R\omega}{c} + \frac{2R\kappa t}{c})] \quad (3.5)$$

The exponential of Equation 3.5 has two defining characteristics, a constant phase

term that is not time dependent but depends on range and laser frequency and an oscillating component with a frequency that depends on the range to the target and the chirp rate. The second term begins with  $t = 0$  for each chirp so the first term sets the phase of the signal. Fourier transforming the signal can reveal, with exact knowledge of the chirp rate, a very precise time delay (and hence range) measurement [4].

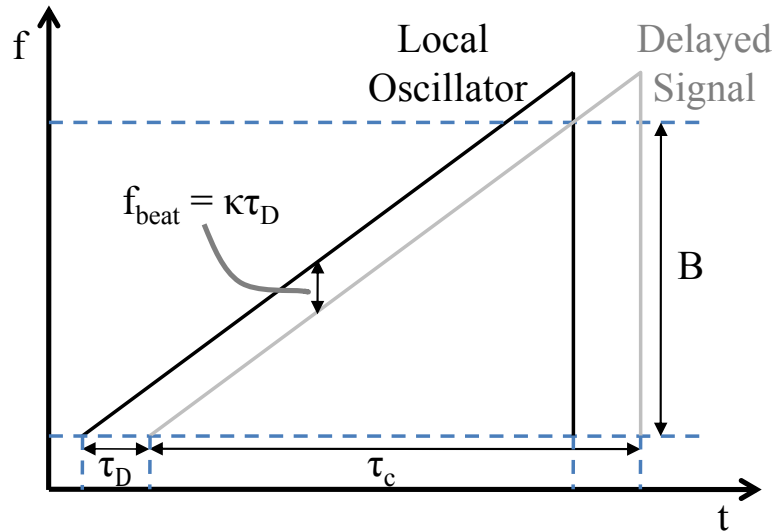


Figure 4: Chirp/Beat A visual relating the time delay to the beat note and chirp rate. The time delay between the LO and return path is denoted by  $\tau_D$ . The overall chirp length is denoted by  $\tau_c$ . The bandwidth of the chirp is denoted by  $B$ .

### Chirp Linearization

The above derivation strongly depends on the linearity of the chirp. If the chirp is not linear then the frequency in the interference term will spread depending on the chirp's deviation from linearity. The model then fails to describe the CR system. The sub 100 kHz linearity of the chirp puts the uncertainty from chirp nonlinearity for the  $\sim 3$  THz

chirp bandwidth in the 1ppm range [11]. Thus the nonlinearity is a non-issue compared to other sources of error in the overall SAL system.

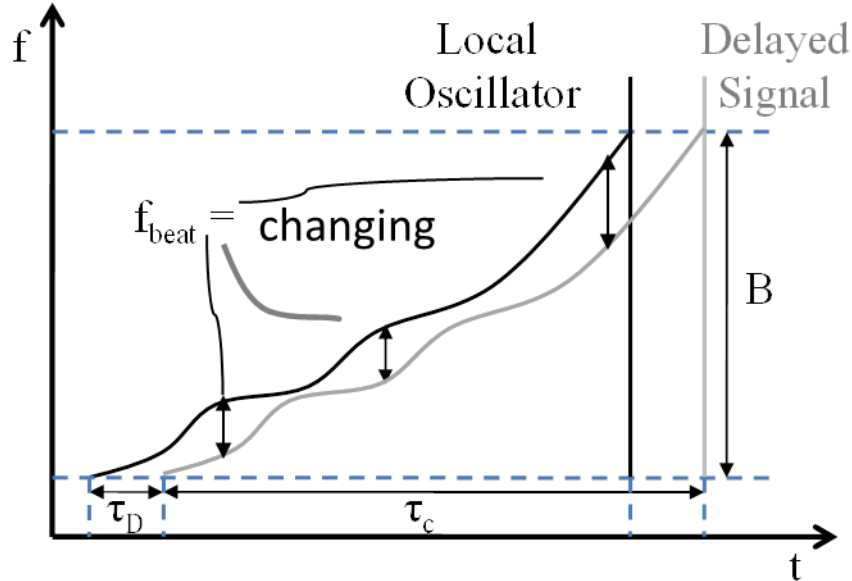


Figure 5: Effect of Poor Chirp The detrimental effect of chirp nonlinearity. The frequency separation between the LO and the delayed signal is not consistent in the frequency-time representation.

Previous demonstrations of SAL have suffered greatly from chirp nonlinearity and have resorted to complicated reference schemes to circumvent the problem [12]. The quoted linearity of [13] was, “Not better than 1%”. The work contained in this thesis is therefore extremely simplified by the availability of the linearized laser chirp source [4] with linearity better than 1ppm. While the resampling procedure in previous research was effective, using a highly linear chirp is the ideal scenario versus resampling a noisy signal. With this tool, the mathematical model for CR above is in fact a very good approximation to the action of the CR system in reality.

### Range Resolution

The range resolution of the CR system is theoretically governed by the bandwidth of the chirp,  $B$ . Equation 3.6 describes this relationship [2].

$$\Delta R = \frac{c}{2B} \quad (3.6)$$

The SAR literature states, “From signal theory, a pulse of bandwidth  $B$  can be compressed to a time duration of approximately  $1/B$  [1].” This statement suggests the inverse relationship between bandwidth and time of flight (range) resolution (larger bandwidth implies finer resolution). Equation 3.6 is derived in Equation 3.7. As is shown, the derivation begins by expressing the beat frequency  $f$  in terms of the chirp rate  $\kappa$  and the time delay  $\tau$ . The time delay is then re-expressed in terms of range,  $R$ , and the speed of light,  $c$ . In line 2, the range resolution is then related to the frequency resolution (defined in line 3) in terms of the chirp length  $T$ . Finally the chirp rate, chirp length product is identified as the chirp bandwidth,  $B$ , yielding Equation 3.6.

$$f = \kappa\tau = \frac{2\kappa R}{c}$$

$$df = \frac{2\kappa}{c} dR$$

$$df = \frac{1}{T}$$
(3.7)

$$dR = \frac{cdf}{2\kappa} = \frac{c}{2\kappa\tau} = \frac{c}{2B}$$

The experiments in this thesis generally employed a 3 THz bandwidth chirp yielding a theoretical range resolution of 50 microns.

In terms of resolving two closely spaced targets, the definition is not as concrete. Rayleigh's criterion of a  $\sim 27\%$  dip between peak intensities of two target returns is one method [14]. As [2] notes, however, "While [Equation 3.6] does provide a certain useful and practical measure of resolution, the issue of resolvability [for two targets] is more complicated than the formula might suggest." One example of this complication is that the relative phases of two closely spaced point targets affects their resolution when the magnitude square of the signal is taken [2,14].

### Description of CR System

The CR system used for the research in this thesis consists of a chirp source, appropriate optics for organizing the signal, and a detector. The result is then processed on a computer. A more detailed description of these components is given below.

#### Laser Source

It should be noted, as a point of interest, that the chirp laser source was originally designed for spectral hole burning studies. CR was then realized as another application of the chirp laser source. The laser used is a broadband tunable laser centered around 1.55 microns. If the laser were rapidly scanned across its available range of frequencies, the resultant chirp would contain severe nonlinearities. An active feedback system is in place to force the laser to chirp linearly.

The linearization of the chirp in fact relies on interference techniques employed similarly to CR. In short, a fiber delay serves as a length reference for interferometric beatnote phase locking. A feedback system forces the chirp to maintain linearity [4].

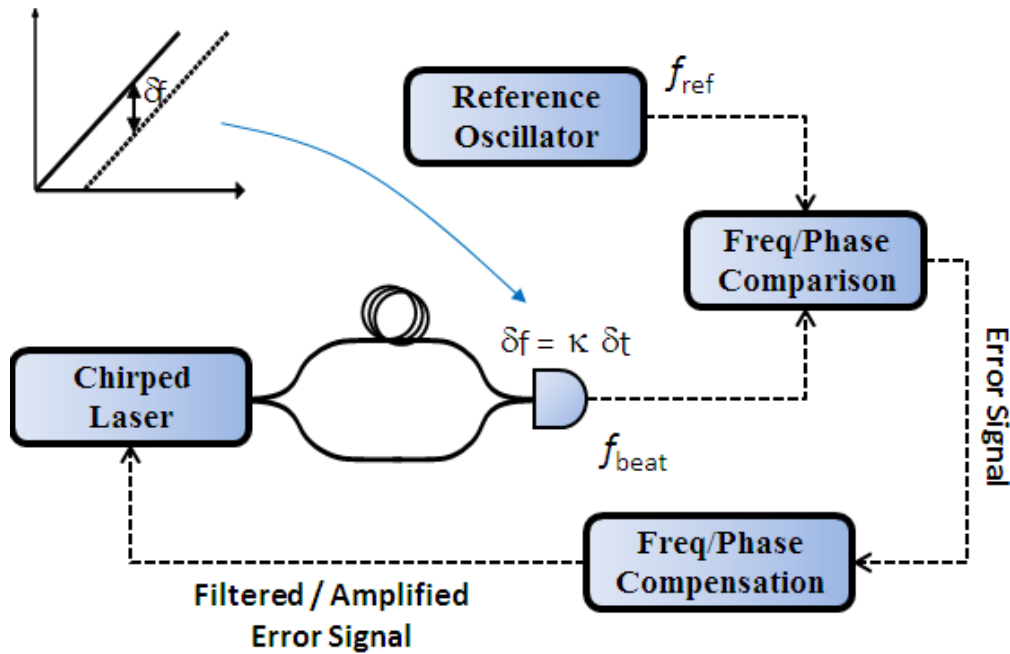


Figure 6: Chirp Linearization Schematic of the chirp linearization process. The loops in the top path after the chirped laser source serve as the fiber length reference.

### Fiber Set-Up

The fiber set-up is described below. It has room for more complicated deployment that will be described as needed. Initially, the laser output is split with a 99/1 fiber splitter into a transmit and an LO path respectively. The transmit path then goes to a circulator to allow for transmission and reception in the same fiber. A fiber circulator has three ports. One port serves as the “in” point. The second port serves to transmit and receive light in and out of the same fiber. The third point serves as an out for the light received by the second port. The function of the circulator is to force the light received into the second port out of the third port (not back into the first).

The circulator showed significant power induced backscatter above 200 mW optical power. For this reason a 4x1 fiber array (multiple, separate fibers sitting side by side with faces in the same direction) was sometimes used to allow for transmission and reception at fibers with 125 micron separation and complete optical isolation. The 4x1 was the cheapest array of this kind while still offering several options attractive for later experimentation such as IFSAL. The received signal is then optically mixed with the LO path using a 2X2 fiber coupler. The two outputs of the coupler then go to the auto-balance detector [15]. See Figure 12 for full set up. A schematic of the circulator and fiber array are shown below in Figure 7.

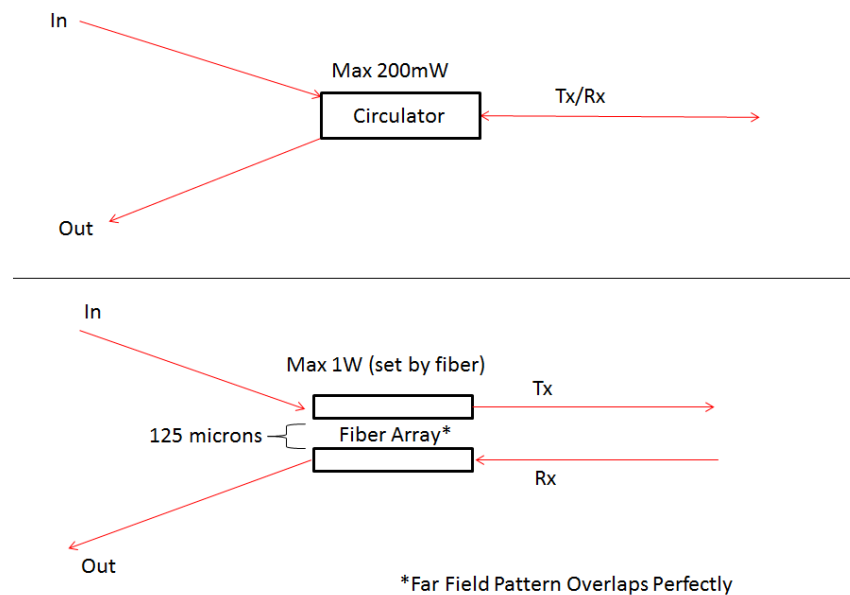


Figure 7: Circulator Vs Fiber Array The circulator uses internal optics to allow Tx/Rx in and out of the same port with different input / output ports. The maximum power allowed before nonlinearities occurred was 200mW. The fiber array optically isolates Tx and Rx paths by aligning multiple fibers resting next to each other in a machined holder. The maximum allowable fiber is then increased to the fiber tolerance of 1W.

### Auto-Balance Detector

A photodiode detector is used to convert the signal from optical to electrical. This electrical signal is then recorded on the computer using a digitizer card operating at up to 5 MHz. The detector ensures that signal is shot noise limited using a technique to remove other noise sources such as, "...vibration, Johnson (thermal) noise, dark current noise...excess laser noise, and extinction noise from aerosols...", from the signal using an auto-balance technique [16].

## SYNTHETIC APERTURE LADAR BASICS

Synthetic Aperture Ladar (SAL) is not, at the onset, an intuitive way to form an image. The idea of forming high resolution images of a scene using a diffraction limited system is not entirely obvious. Studying the basics of the subject from various perspectives will help to reveal the mechanics of SAL.

### History and Philosophy

As stated in the introduction, SAL is directly descendent from Synthetic Aperture Radar (SAR) imaging. SAR is a radar technique that uses airborne and satellite platforms to sweep out a “synthetic aperture” in order to image terrestrial surfaces of interest. In 1951, Carl Wiley realized the cross range resolution of radar imaging systems could be improved by recording range information of a scene on a small antenna from locations along an invisible track similar to a long antenna. The basic scheme is to record a set of information about a target from different locations and use it to enhance the cross range resolution [1,2].

### Photon Budget

A photon budget describes the economy of photons required to form an image given a limited availability. A photon budget revolves around two questions. How much light can be transmitted to the scene? And how much light can be retrieved from the scene? The primary weakness of SAL is its extremely poor photon budget, especially in stripmap mode – see Figure 10 for mode distinction.

The answer to the first question was addressed experimentally by measuring the power output to the scene after amplification by a diode amplifier and then calculated the diffraction of that beam. In the images in this thesis, between 100mW and 1W of optical power were used. Specific powers will be noted for each experimental result in subsequent chapters.

The second question can be addressed with a model to predict the amount of collected light from a certain range and surface material of interest. Three general types of material are available. Specular materials cannot be imaged by the systems studied here as they do not return any light to the transmit / receive (Tx/Rx) stage. Diffuse materials can be studied as they diffusely reflect light and in general enough of this light is collected to form an image. Retro-reflective targets are the easiest to image as all incident light is returned to the Tx/Rx stage causing a strong return signal. The model for return signal power is described by Equation 4.1a, valid in the far field of the aperture [17]. The returned optical power, including beam divergence, is modeled in terms of the transmitted power  $P_{transmit}$ , the target cross section  $\sigma$ , target reflectivity  $\rho$ , line target thickness  $d$ , the aperture diameter  $D$ , the range  $R$ , the illumination wavelength  $\lambda$  and the material absorption parameter  $\eta$  [17].

$$P_{return} = \frac{P_{transmit} \sigma D^4}{16R^4 \lambda^2} \eta \quad (4.1a)$$

$$\sigma_{line} = 4\rho R d \frac{\lambda}{D} \quad (4.1b)$$

$$\sigma_{point} = 4\rho d A \quad (4.1c)$$

The  $R^{-4}$  dependence is detrimental to signal strength as is the  $D^4$ . The severity is somewhat mitigated by the target cross-section factor  $\sigma$ . Equations for the scattering cross section of a line target and a point target are above in Equations 4.1 b and c. Reasonable target cross section factors would be between a solid line target and a point scatter. Thus the range dependence of the return power for a diffusely scattering target is likely at the very best  $R^{-3}$  for stripmap mode.

Also apparent is that a smaller aperture size will decrease the collected power. However, smaller real aperture size also improves the achievable cross range resolution in stripmap mode— discussed in detail in this chapter under “Cross Range Resolution Derivation” and “Fourier Optics Explanation” [2]. This is the primary tradeoff of SAL. In most cases images were formed with the minimum size real aperture, a 10 micron diameter single mode fiber optic. At larger ranges, larger apertures may be required to collect an acceptable return signal.

Studies were conducted on a qualitative basis to characterize the target reflectivity  $\rho$  of several different materials. The Lambertian qualities of the diffuse test material Spectralon was verified with the CR system. Aluminum, paper, and organic surfaces were all studied as well. Organic surfaces were often the best targets for their highly uniform diffusivity. Some metallic surfaces such as anodized aluminum were surprisingly diffuse. This allowed for imaging of anodized aluminum surfaces. Plastics were particularly tricky as they often yield a range return that exponentially decays into the semi-transparent surface. A plastic surface rarely served as a good SAL target.

For a transmit optical power of 1W, a single point target (i.e. smaller than the resolution of 100 micron<sup>2</sup> resolved pixel) needs to provide a return of approximately 1 nW of optical power in order for the SNR between the LO shot noise and the return signal to be unity [16]. The photon budget Equations set 4.1 suggest the return for a diffuse point target (range 1m, output power 1W, real aperture 1 microns) is at least three orders of magnitude lower than the calculated requirement above. However, hundreds of point targets at each range (enhancing signal return at that range) and the coherent integration over thousands of shots help to explain how weak scatterers are imaged “out of the noise floor.” Further, the chirp duration affects the integration time of a single shot which also affects noise. More specific analysis of this problem would require assumptions specific to an imaging situation of interest.

### Collection Geometry

The geometry of the experiment is essential as a starting point for mathematical models. Figure 8 below will serve as a primary reference and describes the SAL geometry for a single point scatterer. The aperture locations are indexed with  $n$  and the point scatters (in this case there is only one) are indexed with  $j$ . The Equation in the figure describes the range  $R_{n,j}$  to scatter  $j$  from aperture location  $n$ . The range Equation for  $R_{n,j}$  will help to describe the phase evolution sufficiently to derive a model for the Fourier relationship required for image formation.

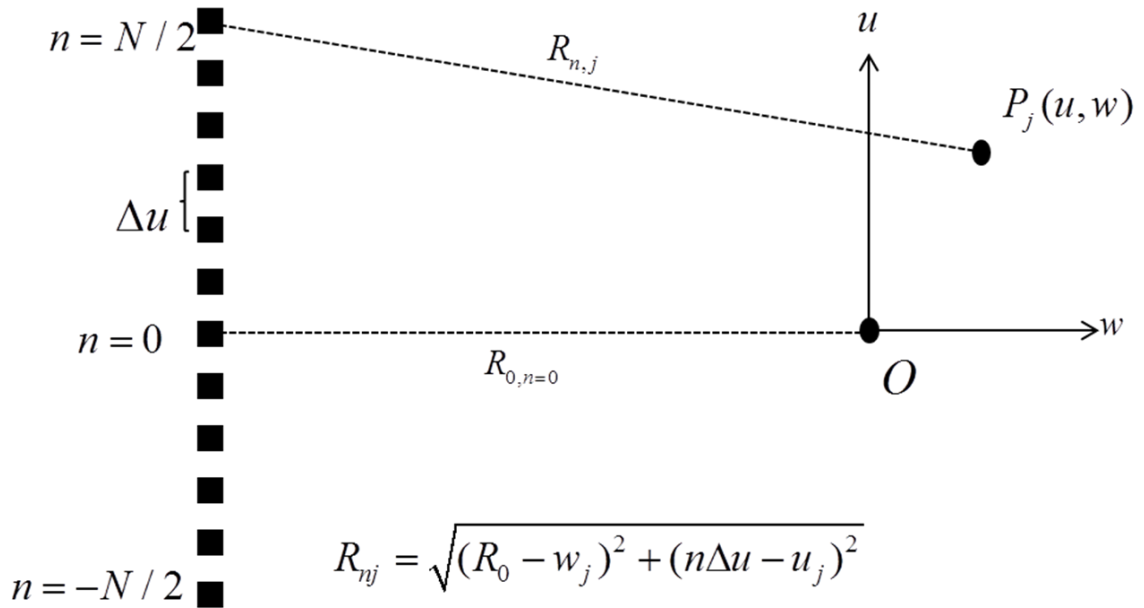


Figure 8: SAL Geometry Collection geometry and definition of variables. Range  $R_{n,j}$  to scatter  $j$  from aperture location  $n$ .  $R_{0,n=0}$  is the range from the center of the aperture to the center of the scene.  $u, w$  are the cross range and range coordinates, respectively, of a point scatterer relative to scene center/origin  $O$ .  $R_{n,j}$  is shown as a function of shot  $n$ .

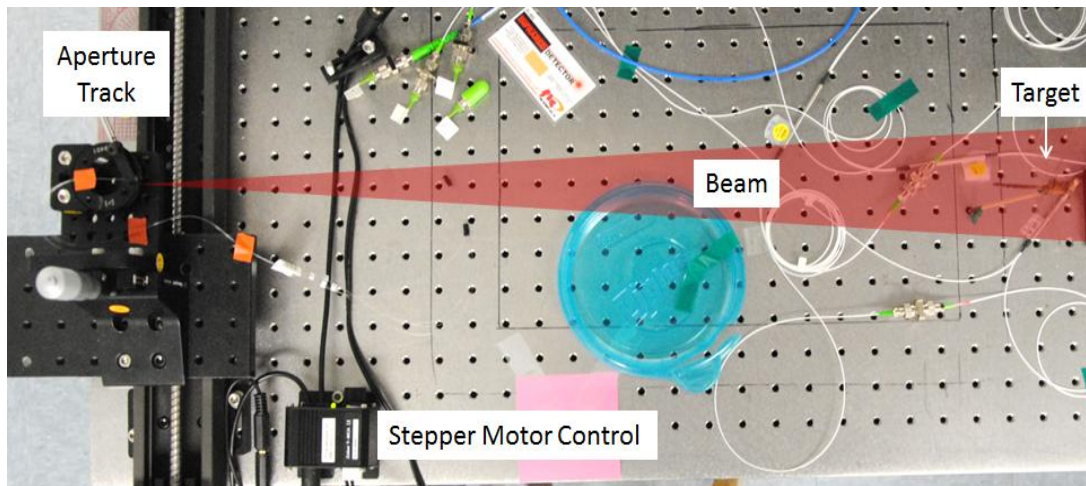


Figure 9: Overhead Photo Overhead view of experiment corresponding to the model geometry above. Beam is allowed to diverge from fiber aperture at left.

Note that the transmit direction in Figure 9 is orthogonal to the aperture track for this derivation. This is called broadside mode, as opposed to squint mode collection where the transmit direction of the beam may not be orthogonal to the aperture track. Monostatic SAL implies that the transmit and receive aperture are at the same location versus a split bistatic configuration. Stepping the real aperture along the track without steering the beam is known as stripmap mode. This mode differs from the more challenging engineering task of spotlight mode where the beam is steered to always illuminate the target. The difference is graphically shown in Figure 10. The remainder of Chapter 3 and subsequent results will focus on stripmap whereas Chapter 9 will discuss spotlight mode.

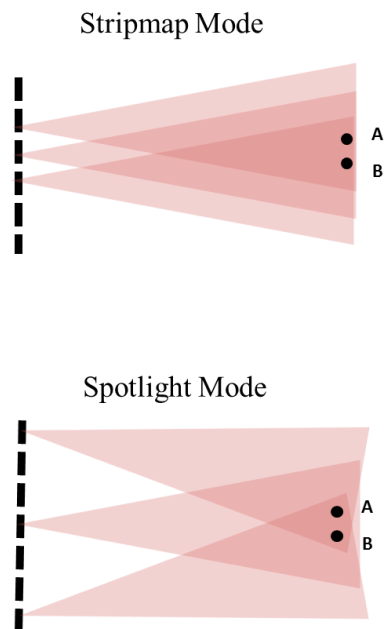


Figure 10: Stripmap Vs Spotlight Spotlight and stripmap synthetic aperture modes. Stripmap – the beam is always broadside to the track as the real aperture is stepped. Spotlight, the beam is steered to keep the beam illumination on the targets center.

### Various Fundamentals

SAL employs a variety of concepts from different perspectives. A model of SAL is followed by mention of tomographic and Fourier optics approaches, all related. The approach in this thesis (which proved to be a very powerful modeling tool) was to derive the range evolution, put that into the CR Equation 3.5, and then study the form relative to a Fourier kernel for removable errors.

#### Derivation of Fourier Relationship

Equation 3.5 showed the dependence of the CR signal on range to target. The above expression for  $R_{n,j}$  can be approximated using Taylor expansions and ignoring small terms relative to the range to the target  $R_0$ . The last line of Equation 4.2 excludes the constant range to target  $R_0$  common to all scatterers and includes the variable term in cross range position  $u_j$  (the dynamic cross range term that depends changes with  $n$ ) and  $w_j$  (to include down range dependence). These approximations rely on the dimensions of the target ( $\sim 2\text{cm}$ ) being small compared to the range to scene ( $\sim 1.5\text{m}$ ).

$$\begin{aligned}
 R_{n,j} &= \sqrt{(R_0 - w_j)^2 + (n\Delta u - u_j)^2} \\
 &\approx (R_0 - w_j) \sqrt{1 + \frac{(n\Delta u - u_j)^2}{(R_0 - w_j)^2}} \\
 &\approx R_0 - w_j + \frac{n^2 \Delta u^2 - 2nu_j \Delta u + u_j^2}{2(R_0 - w_j)} \\
 &\approx \frac{-nu_j \Delta u}{R_0} - w_j
 \end{aligned} \tag{4.2}$$

This approximation of Equation 4.2 for  $R_{n,j}$  can then be put into Equation 3.5 to yield Equation 4.3 where  $\mu$  and  $\xi$  are spatial frequency variables and P is the signal amplitude

from each scatterer on each shot.

$$\begin{aligned}
 E_{n,j} &= E_{LO} E_{signal}^* = P_{n,j} \exp[-i(\mu u + \xi w)] \\
 \mu &= \frac{-n\Delta u}{R_0} \left( \frac{2\omega}{c} + \frac{2\kappa t}{c} \right) \\
 \xi &= -\left( \frac{2\omega}{c} + \frac{2\kappa t}{c} \right)
 \end{aligned} \tag{4.3}$$

The variables  $\mu$  and  $\xi$  can be further simplified as in Equation 4.4. The  $\frac{2\kappa t}{c}$  term in  $\mu$  is ignored as  $(\frac{2\omega}{c} \sim 10^6) \gg (\frac{2\kappa t}{c} \sim 0 \rightarrow 10^{-5})$ . The  $\frac{2\kappa t}{c}$  term is allowed to remain in  $\xi$  as it includes  $t$ , the only dynamic variable in  $\xi$ . The dynamic variables in Equation 4.4 are  $n$  (for  $\mu$ ) and  $t$  (for  $\xi$ ). In some literature,  $n$  is referred to as the shot to shot “slow time” and  $t$  as the intra-shot “fast time”.

$$\begin{aligned}
 \mu_n &\approx \frac{-n\Delta u}{R_0} \left( \frac{2\omega}{c} \right) \\
 \xi &\approx -\left( \frac{2\omega}{c} + \frac{2\kappa t}{c} \right)
 \end{aligned} \tag{4.4}$$

The resultant collected dataset over all  $j$  point scatters at each aperture location  $n$  is then described by Equation 4.5.

$$E_n = \sum_j P_{n,j} \exp[-i(\mu u_j + \xi w_j)] \tag{4.5}$$

The form of Equation 4.4 is equivalent to the kernel in the two dimensional Fourier transform of Equation 4.12. This implies collected data constitutes a harmonic basis set with scatterer location modulating the basis functions. This derivation

establishes the collected data as an approximation of the Fourier transform of the target reflectivity.

The approximations made in the above derivation may seem both severe and unfounded. In practice, however, the Fourier relationship between the collected data and the image is indeed a very effective description. The approximations rely on the range to the scene being much larger than the size of the scene. This point allows the derivation to make contact with the physical interpretation that the synthetic aperture is effectively a sampling of the far field, Fraunhofer diffraction pattern of the image. From another perspective, the Taylor expansion step included only the linearly evolving phase terms. This allowed us to assume a harmonic basis set and make contact with the Fourier Transform.

### Tomographic

Another way to view SAL is from a tomographic perspective. Tomography is the process of recovering an image from collected cross sections. This view of synthetic aperture systems was popularized by the SAR researcher Charles Jackowatz in the early 1990s. The mathematics of the tomographic perspective can become cumbersome relative to the models outlined in this chapter and are not necessary for a complete description of SAL. However, it is important that this perspective be mentioned as a means to inform the reader suspecting a connection between tomography and SAL that one does indeed exist [2].

The most common tomographic technique is computed tomography, “CT scans”, so widely used in medical imaging. Despite the long term existence of the CT since the

1970s, the mathematical connection was not made until the 1980s. It should also be noted that the tomographic perspective is more pertinent to spotlight mode synthetic apertures – another reason why the extensive formalism will be avoided.

### Cross Range Resolution Derivation

A derivation of cross range resolution of stripmap SAL starts with the angular beam width (angular resolution) of a synthetic aperture length  $L$  at a wavelength  $\lambda$  shown in Equation 4.6 [18]. An optical analogy would be to think of the effective “synthetic lens diameter”  $L$  of a cylindrical lens and the related minimum resolvable spot width.

$$\theta_{SA} = \frac{\lambda}{2L} \quad (4.6)$$

Equation 4.7 gives a spatial beam width (spatial cross range resolution) approximately for small angles.

$$\delta y = R\theta_{SA} \quad (4.7)$$

Combining Equations 4.6 and 4.7 yields Equation 4.8 for the cross range resolution of the synthetic aperture.

$$\delta y = \frac{R\lambda}{2L} \quad (4.8)$$

The maximum spatial extent  $S$  that the target can remain in the real aperture beam spot is defined by Equation 4.9. From diffraction theory, the diffraction angle  $\theta$  of the real aperture diameter  $D$  is also related in Equation 4.9.

$$S = R\theta_{\max} = \frac{R\lambda}{D} \quad (4.9)$$

Assuming the diffraction angle defines a hard cutoff for the beam (i.e. points inside a cone defined by the diffraction angle are fully illuminated and outside are dark), the maximum synthetic aperture length  $L$  can be equated to  $S$ . Under this condition, Equations 4.8 and 4.9 can be combined to estimate the physical limit on cross range resolution of a point target positioned normal to the midpoint of the aperture track in Equation 4.10.

$$\delta y = \frac{D}{2} \quad (4.10)$$

The resolution of an extended target for a synthetic aperture length  $S$  (i.e. full real aperture beam width is utilized for a centered target) will be degraded depending on the cross range position  $u$  of individual scatters relative to the line normal to the midpoint of the synthetic aperture track (i.e.  $R_{0,n=0}$  in Figure 8). As Equation 4.11 shows, when  $u = L$  the scatter is not resolved – it was never in the beam [18].

$$\delta y_{real} = \frac{\delta y}{1 - \frac{u}{L}} \quad (4.11)$$

One practical requirement for Equation 4.10 to hold is that the real aperture be stepped in increments of  $D/2$  to avoid Nyquist related aliasing [2]. Sample spacing below this limit causes the real aperture to act as a low pass spatial filter – so there is no added benefit.

#### Fourier Optics Explanation

The angular spectrum is a concept often used in Fourier optics [14]. One explanation of the above derivation is that SAL essentially samples the angular spectrum

(again the Fraunhofer far-field diffraction pattern) of a target. The imaging situation of mono-static SAL is unique as it ensures the maximum angular spread of the illumination of the target and return signals are the same. The counter-intuitive result of 4.10 shows the resolution improves with decreasing aperture size  $D$ . By maximizing the diffraction, the angular extent that the target can remain in the beam is increased. This allows for more of the angular spectrum to be sampled and the resolution to be improved [14].

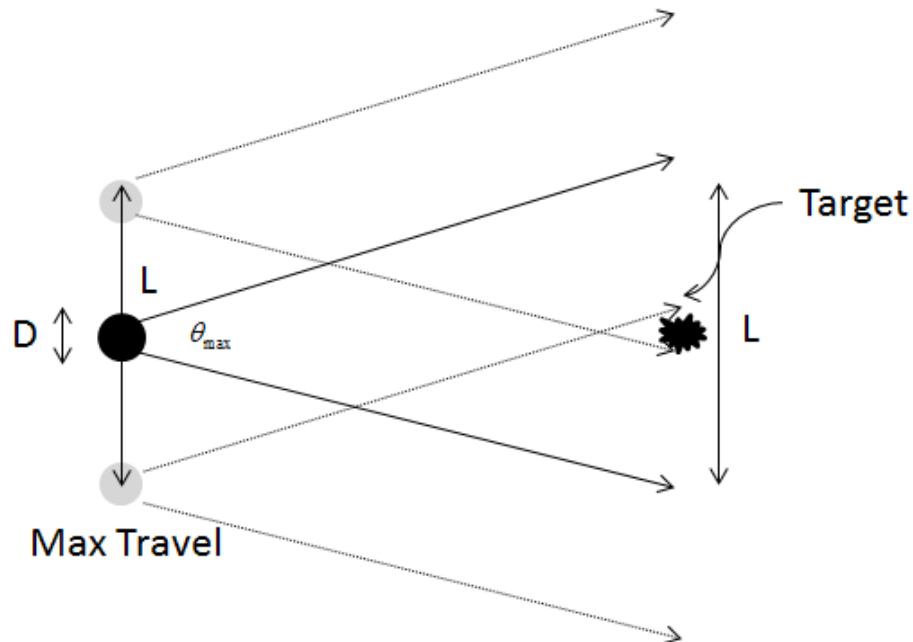


Figure 11: Angular Spectrum Idea Increasing the diffraction angle  $\theta$  increases the maximum synthetic aperture length  $L = S$  (length where centered target will remain in beam coverage area) is increased which in turn improves resolution. This is analogous to having more angular spectrum available for sampling.

### Analysis of the Angular Spectrum Approach

The cross range resolution limit can be explained in an angular spectrum context successfully as shown above. The derivation of Equation 4.10 was for a point scatterer with a range closest when the real aperture is at the midpoint of its synthetic aperture

track. The  $L = S$  requirement ensures the sampling is done with the entire available angular spectrum. Considering Equation 4.11, longer ranges are preferable as the target size to spot width ratio  $u/L$  decreases and accordingly mitigates resolution degradation as a function of off central axis position. The  $u/L$  term implies off axis targets offer less of their angular spectrum for sampling. Extending range for this reason opposes the range dependence of the photon budget of SAL and a trade-off will always be present. Also, extending the range for the above reasons will require length of the synthetic aperture track  $L$  to increase to achieve maximum resolution so the practicality of this approach would begin to suffer for larger ranges.

### Experimental Set Up

For an “optics imaging” experiment, the setup is strange for its overall lack of optics! From a hardware perspective, the only difference between the SAL set-up and the CR set-up is the addition of a lead screw driven by a stepper motor. The transmit/receive station of the CR system sits on a cart atop the lead screw platform. The station is then discretely stepped by the platform to create a synthetic aperture as range profiles are collected at each location.

### Aperture Stepper Stage

The stepper stage used was driven by a Zaber stepper motor with angular resolution in combination with the lead screw pitch adequate to provide calibrated 10 micron linear steps. The motor was computer driven through a USB to Serial converter port using serial commands. MATLAB was able to interface with this device allowing

for integration into the collection program. Thus the process of collecting SAL data could be optimized to take less time and prevent timing errors. The time consideration was especially important as a full SAL scan could take up to one hour.

### Dimensions

Targets sat anywhere from half a meter to two meters away. The steps taken along the aperture track were 10 microns in order to match the fiber mode field diameter of 10.5 microns. Any smaller steps and the width of the real aperture fiber core would act as a low pass filter on the collected phase evolution. Any larger steps and high frequency content in the phase evolution would be under-sampled resulting in aliasing.

### Optical Power

The optical power output ranged from 30mW to almost 1W. The amplifier used to get to 1W was shared with another experiment. Further, the optical circulator was only rated to 200mW. Only when the fiber array, providing complete optical isolation, and the amplifier were both in use was 1W of optical power available. The photon budget shows that increasing the output power provides Signal-to-Noise Ratio (SNR) enhancement with the square root of power. So while the magnitude of the return signal is much more dependent on real aperture diameter and range than on optical power as in Equation 4.1, increased output power does provide improved in SNR.

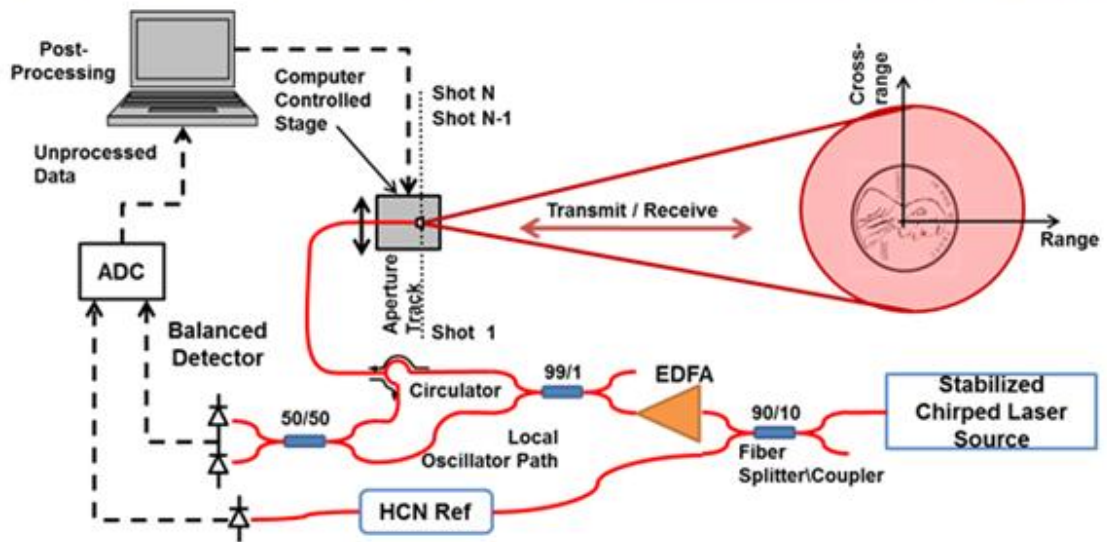
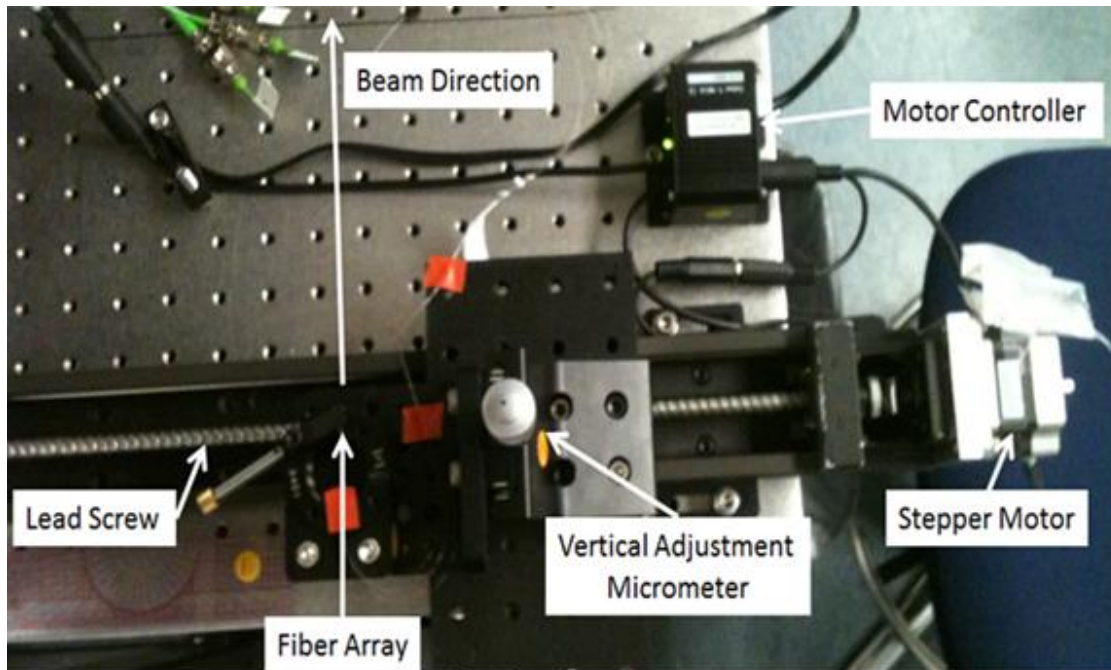


Figure 12: Experimental Setup Photo and Schematic Photo of SAL transmit/receive stage (top) and overall system schematic (bottom). The transmit/receive station is stepped along the direction parallel to the lead screw.

### Sample Rate

A maximum of 0.5 Msamples per shot were allowed before memory became an issue in MATLAB. The sample rate of the digitizer card used was generally 4.67 MHz in order to match the 300 ms length of the chirp to reach 0.5 Msamples. The sample rate was changed inversely with chirp length to maintain 0.5 Msamples per shot.

### HCN Cell

An Hydrogen Cyanide (HCN) cell was employed to track the frequency of the laser. The chirp of the laser is not entirely consistent in its starting frequency. This leads to uncertainty in the instantaneous frequency of the chirp laser relative to the trigger for each shot. The temporal variation in the location of a spectral feature relative to shot trigger was on the order of a millisecond. A chirp rate of 10 THz/sec yields an instantaneous starting frequency uncertainty  $\sim 10$  GHz. HCN provides a comb of sharp spectral features. By recording the intensity of laser light through the HCN cell as the laser chirps, the spectral features can be used to correct the collected range data so it corresponds to the same range of frequencies of the chirp for each range shot. This is important to help ensure coherence of the shots and phase stability [13].

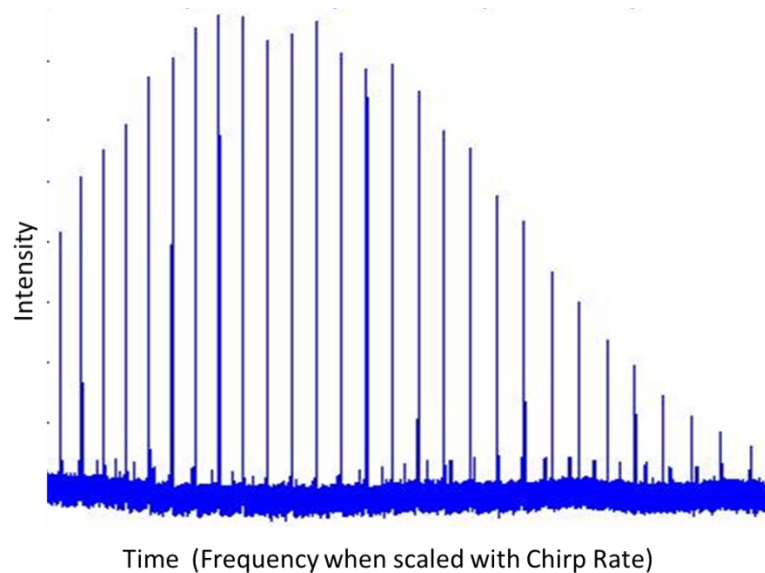


Figure 13: HCN Data Data from HCN cell used for triggering digitizer collection. The sharp spectral features across the chirp are evident. The horizontal axis was collected in time but when scaled with the chirp rate would represent frequency profile of HCN absorption spectrum.

#### MATLAB Code Description

The MATLAB code used is included in Appendix A but is briefly described here. The script was required to manage data collection, stepper motor control, and data size management. To minimize run time, the program records shot data and then moves the stepper motor while processing the previous shot. Beyond recording the range and HCN cell data into MATLAB, the program is required to fit a specific spectral feature, generally the first, of the HCN cell in order to find its peak in time. This time stamp is then used to trim the collected range data so that the first point of range data always corresponds to the same frequency in the chirp. This trimming accounts for less than one percent of the total collected data. The fit of the single spectral line is performed using a nonlinear fit algorithm to a Lorentzian line shape function. The range data is optionally

windowed for side lobe suppression and the range profile is computed using the FFT function. The portion of range of interest, generally 2048 points, is then cut out of the range profile and saved. This is done to avoid saving and processing range profiles consisting of several hundred thousand data points with each shot. The 2048 points correspond to different ranges depending on the chirp but in general 2048 points is less than one percent of the total range data collected – a significant reduction in memory usage and necessary considering an uncompressed 2048x2048 complex image is roughly 60 MB. For stripmap SAL, each shot corresponds to a column in the matrix of collected data. The column dimension is perpendicular to the aperture track. The rows therefore correspond to a common range over all shots. The row dimension is parallel to the aperture track.

#### Previous Experimental Set-Up Variations

The set up described above was not the first iteration of SAL experimentation. Originally, the stepper motor was attached to a micrometer stage that served as a platform for the target with the Tx/Rx station remaining stationary. While the travel length of the stage was sufficient for SAL, the stage did not provide sufficient rigidity for smooth linear motion. A modulation in the track manifested itself in the image as significant ghosting. Ghosting describes the replication of the main body of the image in weaker forms at other cross range locations in the image field due to harmonics of the modulation. The second SAL set up (Figure 9 and Figure 12) with the lead screw serving as the motion platform eliminated the ghosting effect. This indicates the likely cause was in fact the poor track for the platform. The previous configuration was technically

Inverse SAL (ISAL) as the target, not the aperture, moves. The mathematics of ISAL is identical to SAL.

Much of the SAL data was taken using fiber collimated light that was then focused down to a point and sent through a 100 micron pinhole. A cage system was used to mount and align this finicky system. In this configuration the real aperture diameter was much larger than a bare fiber - mode field diameter 10.5 microns. This was necessary because it allowed more signal and at the time the system was operating on 20mW of optical power which provided poor SNR. The drawback of the larger aperture was degraded cross range resolution relative to a bare fiber.

When an optical amplifier allowing power output up to 200mW (circulator maximum) became available the setup went to a bare fiber as the real aperture. The increase in optical power (~10 times increase) helps to offset the massive decrease in the real aperture collection area (~100 times decrease). The resolution of the SAL images did improve dramatically and this configuration was used for the rest of the experiments. The bare fiber was desirable as it eliminated the need for free space optics. The use of the bare fiber defined the real aperture and proved the absolute “synthetic-ness” of SAL (i.e. vastly exceeding the diffraction limit of the fiber). The necessary alignment was to steer the beam to be orthogonal to the aperture track. This was done with an IR card.

### Phase Error

The primary source of poor SAL image quality is shot to shot phase error. Phase error can be modeled as a noise term added to the exponential term of Equation 3.5.

Phase errors are inevitable as vibrations in the experimental set up and air or temperature fluctuations will lead to path length differences greater than the wavelength of light used. Aluminum hardware, common in this set up, has an expansion coefficient (23 microns/m/K) large enough for any component (~ 1 cm length) to shift the range (with an expansion parallel to beam direction) over a tenth of a wavelength with a temperature fluctuation of just 1 C [19]. A few meter of fiber optics (thermal expansion coefficient ~0.1 microns/m/K) such as those used in the ranging set up would experience the same magnitude range shift with only 1C temperature fluctuation as well [20]. Phase error should therefore be expected.

### Effects

The primary effect of phase error is to blur a SAL image which can also prevent Interferometric SAL (IFSAL) image formation (uses multiple SAL images) via phase decoherence [1,2]. The effect is often so severe that SAL images are essentially meaningless before the removal of phase error and interference patterns of IFSAL images is impossible. The severity of the defocus is rooted in the high frequency nature of the errors which causes a broader point spread function.

### Piston Error

Piston error is the most basic cause of phase error. This is a modulation of the position of the aperture location in a direction orthogonal to the aperture track. This amplitude of this modulation can be on the order of tens of microns. Thus the phase error can be on the order of hundreds of radians. A phase error as small as a tenth of a

wavelength can affect SAL image focus, so the expected phase errors can be detrimental. A schematic of piston phase error is shown in Figure 14. Another way to think about piston error is as a deviation from sampling the phase along a flat wave front.

Piston error shows up in the derived Fourier kernel as a phase error  $\phi(n)$  in Equation 4.12 that depends only on the shot, not range or cross range coordinates. Further, piston error is assumed to be constant during a shot.  $PistonError(n)$  is the constant deviation in meters of each shot from the flat wave front (i.e. ideal synthetic aperture track motion).

$$E_n \propto \exp[-i\phi(n)] * \sum_j \exp[-i(\mu u_j + \xi w_j)]$$

$$\phi(n) = PistonError(n) * \left(\frac{2\pi}{\lambda}\right) \quad (4.12)$$

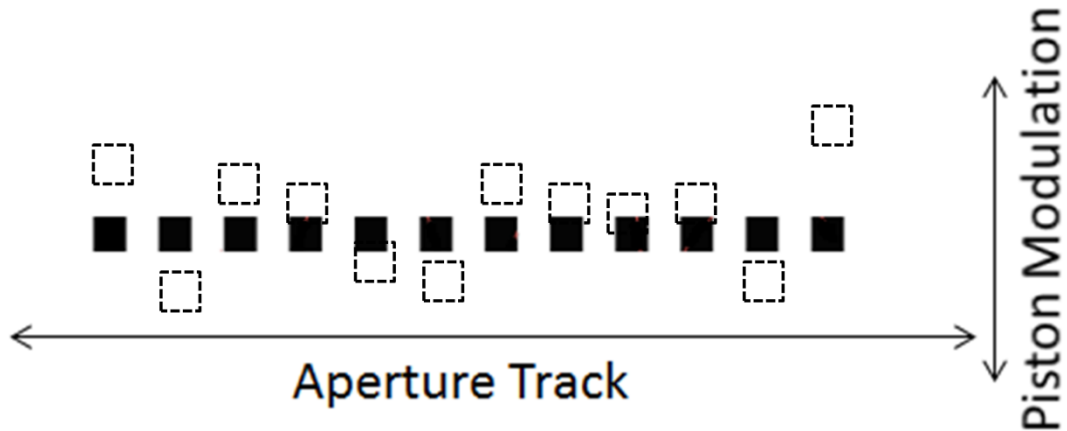


Figure 14: Piston Error Random piston error (dashed aperture positions) is orthogonal to ideal aperture track positions (solid). Squares are real aperture locations.

### Inconsistent Stepping Analysis

If the spacing between shots in the direction parallel to the aperture track is not entirely consistent, the effect is minimal. Figure 15 shows the general picture of the error. The sources of this error mode include vibration, lead screw imperfections, and stepper motor inconsistencies or noise.

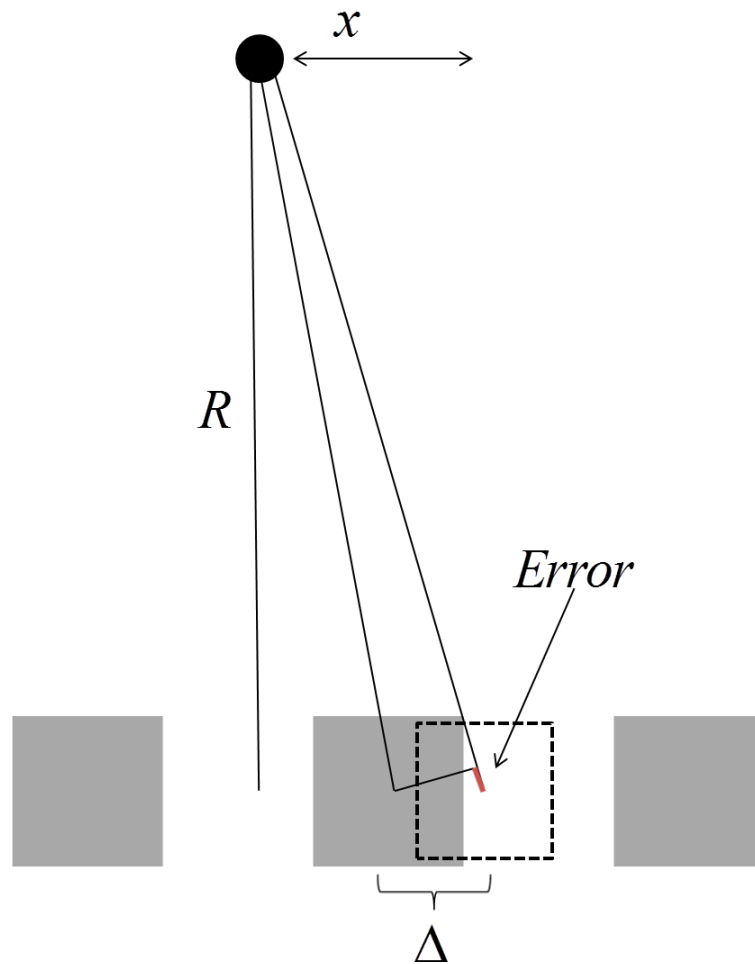


Figure 15: Step Error The step uncertainty  $\Delta$  is shown to be an uncertainty of the location of the real aperture along the synthetic aperture track. The geometry for estimating the magnitude and effects of this error (little red portion) is shown as well with  $x$  representing the cross range location of a point target relative to the aperture and  $R$

the range (large compared to  $x$  and  $\Delta$ ) from the aperture track to the point target.

$$\phi \approx \frac{2\pi x \Delta}{\lambda R} \quad (4.13)$$

Estimated values for Equation 4.13 are  $x=1\text{cm}$  (likely scene width),  $\Delta=2.5$  microns (one quarter of experimental step size),  $\lambda=1.55\text{microns}$ ,  $R=1\text{m}$  yield a phase difference of only 0.1 radians – the upper limit of acceptable phase error. This analysis shows the primary concern is therefore piston error considering the likely magnitude of step uncertainty.

### Twisting Error

Another possible error mode is a rotation of the fiber tip by a small angle. If the twisting occurred on an axis through the fiber tip, no errors would result. If the rotation axis did not align with the fiber tip, the effect could be decoupled into effective piston and step uncertainty errors. The piston component is correctable even for errors on the order of tens of wavelengths. Assuming a distance between rotation axis and fiber tip on the order of a centimeter, the step uncertainty error component could cause phase errors well over a radian for a milliradian rotation. However, there is no experimental evidence (such as a large scale uncorrectable blurring) in the SAL images to support the existence of appreciable twisting errors. A more “real world” SAL demonstration might encounter twisting errors due to target or track motion.

An experiment was conducted with the fiber array to prove the lack of twisting errors. By mounting the fiber array with constituent fibers spaced parallel to the track, an interferogram was formed between adjacent apertures. The overall linearity of the

interference in Figure 16 implies that twisting errors are not prevalent. The effect here is further explained in the IFSAL Chapter.

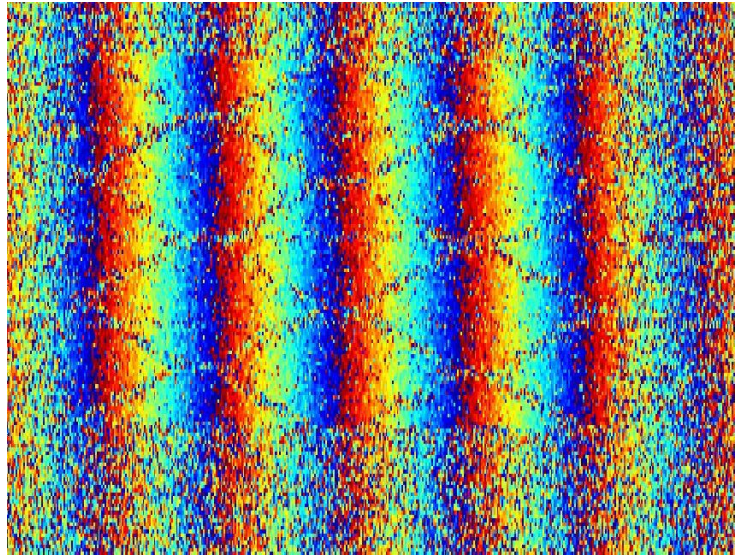


Figure 16: Twist Error The clean interference fringes (no filtering) between the adjacent apertures imply that twisting errors are not a major concern in these experiments. The sharp box of fringes comes from retro-reflective tape used to provide a strong signal for the interference pattern.

### Polar Formatting and Quadratic Phase Errors

Two related effects that are detrimental to SAL image formation are the polar formatting and quadratic phase error [1,2]. In the derivation of the SAL signal and the Fourier relationship, the quadratically evolving phase terms were neglected. In reality, a slight quadratic curvature along the sampled wave front does exist. This curvature has dual implications.

First, the curvature implies that the sampled diffraction pattern is in fact being sampled to a polar, not a Cartesian grid. In the case of the small angles used, the polar grid sampling can be well approximated as a Cartesian grid. This procedure is not

admissible in SAR systems as the angles used there are much larger or spotlight SAR/SAL systems where the aperture motion is not linear. In general, the polar formatting problem manifests itself as a slight migration of shot to shot target location in a quadratic sense from those quadratic terms in  $u$  dropped in linearizing Equation 4.2. This is localized to within about ten pixels for the experimental set up used.

The second remnant of this approximation is the existence of a quadratic term in the phase evolution of the sampled signal stemming from quadratic  $w$  terms dropped in linearizing Equation 4.2. This quadratic phase term exists in the cross range dimension of the collected data in phase of the complex pixel values. Thus the distinction from the polar formatting phenomenon is rather nuanced. This term is corrected as part of phase correction as seen below.

### Residual Phase Error

Residual phase error, those that cannot be removed by any means, will always be present in a SAL image. High frequency vibrations that occur during a shot dwell time will result in blurring in the range dimension. This can be removed with a sharpness metric, discussed below [21]. In the phase error correction section below, the correction is understood to always be an estimate of the actual phase error. In many cases the correction is sufficient to show dramatic improvement in image quality. The Phase Gradient Autofocus algorithm estimates the phase error to within a tenth of a wavelength – a cutoff recommended by [2]. This is generally sufficient to show good focusing of images.

Another means to deal with spatially varying phase error that occur differently at each range (row in the data matrix) is to assign the data in that bin a “sharpness” by means of a sharpness metric algorithm. Phase errors can then be removed by maximizing the sharpness of each range (row) by optimizing the coefficients of a set of orthogonal polynomials (such as Legendre polynomials) that model the phase error [21]. This method was investigated with mixed results (largely due to its huge computational complexity) and no substantial improvement. Speckle (a coherent imaging effect) was likely the reason that sharpness metric based focusing failed. Speckle introduces small (varying over a few pixels), high contrast features in the image which might have confused the algorithm as it tried to sharpen both the speckle and the image.

### Phase Error Correction

With the presence of large phase errors, a means for consistent error correction is necessary. Phase error correction qualitatively translates to focusing an image. Two means were primarily used to correct for phase errors. The Phase to Retro Algorithm uses a cooperative target such as a retro reflector in the scene for correction. The Phase Gradient Autofocus Algorithm is more robust as it does not require a cooperative scene, it is defined below [2].

### Phase to Retro Algorithm

The Phase-to-Retro Algorithm (PRA) is the most basic way to correct phase errors. The idea is derived from prominent point processing, a SAR technique that attempts to utilize exceptionally bright scatterers [1]. In a sense PRA can be considered

“cheating” as it requires the presence of a retro-reflective target in the scene. The retro-reflector was generally a 5mm diameter Ohara glass sphere from Edmund Optics with index of refraction  $\sim 2.0$ . This index for a glass ball sphere leads to complete retro-reflection of light – a valuable tool for this technique. This type of imaging is also called cooperative target imaging as the scene has been “prepared” to cooperate with post processing techniques.

The retro-reflective target in a PRA prepared scene is generally the brightest scatterer in each range profile shot. In parenthesis will be “matrix coordinates” for comparison to the MATLAB code. First, the retro position (index) in each shot (column) was found. Then the phase of each shot (column) was adjusted so that the phase at each retro position (within column) across all shots (across common row) was consistent. This amounts to using the retro as a reference point for correcting piston error. A short MATLAB script for this task is provided in Appendix A.

PRA worked for essentially every scene with a retro reflector. The only drawback is that image focus is often greatest near the retro reflector and often gets poorer further from it. This is because the correction uses the local information of the retro versus phase errors global to the image and fails to address polar formatting issues.

### Phase Gradient Autofocus

Phase Gradient Autofocus (PGA) is a robust technique for phase error correction originally developed by the SAR community. The textbook description of PGA is conceptually difficult due to its lack of physical relevance [1,2]. Here the standard description is outlined for completeness. This is followed by a more physically insightful

description of the PGA as a means to estimate the range-invariant point spread function of the image in cross range.

PGA distinguishes itself from PRA as it does not require a cooperative scene. This is of interest as any real world application of SAL would in general be more robust if cooperative scenes were not required.

### Text Book

The SAR textbook explanation is outlined here for completeness [1,2]. The MATLAB code used to implement the PGA is included in Appendix A. Again, in parenthesis will be “matrix coordinates” for comparison to the MATLAB code. PGA relies on the assumption that phase error is considered to be range independent. This restricts the phase correction to be the same for each range (each row). This also implies that the phase error is primarily the result of piston error as it is common to all ranges.

The algorithm input set is the phase error degraded complex image where  $m$  denotes cross range pixel indexing (row) and  $k$  range (column). For a set of ranges (rows) in the neighborhood of the target, the brightest scatterer is identified at each range (in each row). Each row is then circularly-shifted (MATLAB function to rotate arrays) to align the brightest scatterers in a central column of the image. A window is then applied in cross range (across each row) to isolate those scatterers. A square window is applied to the circ-shifted image set  $g(k,n)$  with  $w$  width decreased at each iteration,  $q$ , as in Equation 4.14. Parameter  $\xi = 1.1$  corresponds to a slowly decreasing window rate relative to  $\xi = 2$  (i.e. halving the window at each iteration) suggested by [2]. This choice of  $\xi$

produced better results in correcting fast errors.

$$g_q(k, n) \rightarrow g_q(k, n) \text{rect}\left(\frac{m\xi^q}{W}\right), q = 0, 1, 2, 3 \dots \quad (4.14)$$

Dropping iterative subscript  $q$ ,  $g(k, n)$  is Fast Fourier Transformed in cross range (across rows), Equation 4.15.

$$g(k, m) = \mathfrak{F}_n \{g(k, n)\} \quad (4.15)$$

$g(k, m)$  is then discretely differentiated in cross range (across rows) and then all bins summed in the range dimension (along columns) as in Equation 4.16. This can be visualized as a phasor sum.

$$\Delta\phi(m) = \angle \sum_{k=1}^m \{g^*(k, m-1) \bar{g}(k, m)\} \quad (4.16)$$

Integration of the now one dimensional  $\Delta\phi(m)$  in Equation 4.17 gives the maximum-likelihood (maximum likelihood metric discussed in broader derivations, [2]) phase error estimate  $\phi(m)$ , example in Fig. 3. The first term in the phase estimation is zero.

$$\phi(m+1) = \sum_{l=1}^m \Delta\phi(l) \quad (4.17)$$

The phase error estimate is then used to correct the out of focus image, Fig. 3. Iteration can provide convergence to a satisfactory phase error correction, Fig. 4. Iteration ceases after the decreasing window size becomes too small or the phase correction becomes negligible – a typical lower limit is  $\pi/10$ .

### Point Spread Function

The PGA is physically explained as an estimate of the range (column) invariant point spread function (PSF) in cross range (rows). By singling out the bright points the assumption is made that they should each be delta functions. Thus any width that the bright point has is present due to the convolution in cross range (across rows) of that point with its PSF. The process of circularly shifting the bright points sets a standard phase for each PSF. Windowing removes the contribution of other scatters at each range (each row). Each row is Fourier transformed and differentiated. The differentiated signal contains only the relative phase differences and removes constant offsets. Thus the summation in the range (column) dimension leads to the estimate of the phase derivative common to all ranges (rows). Integration of this one dimensional signal then reveals the phase estimate. In short, the PGA seeks to make the energy distribution around bright scatterers increasingly narrow by assuming they are all delta functions that are blurred by the same PSF in cross range (across rows).

Some shortcomings of the PGA include its inability to focus scenes lacking prominent bright scattering points. Evenly diffuse objects are often poor candidates for the PGA whereas bright, isolated targets (better modeled as delta functions) are often phase corrected with great success. A delta function is not a good model of a scatterer evenly surrounded by equally bright diffuse scatterers.

## SAL RESULTS

An Early SAL Image

Example of a SAL image from early in the experimentation process is shown below. The targets were retro reflective tape with a “smiley face” stencil, Figure 17, and a US quarter sized Montana State University lapel pin, Figure 18. The optical powers used were 25mw (smiley) and 200mW (MSU lapel) with 100 micron steps for each. The real aperture, set by a pinhole, was 100 microns – this explains the poor resolution relative to the later example of the dragonfly and RAM chip where a 10 micron bare fiber was used. Other reasons for the poor performance were the wobbly aperture stage in use and the specular nature of the target. The smiley was focused with the PRA and the lapel pin with the PGA. The chirp bandwidth was 3THz over 300 ms giving a chirp rate of 10 Thz/sec.

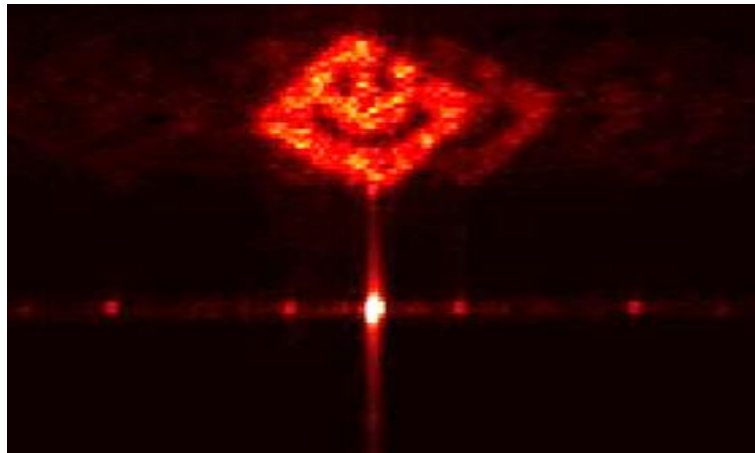


Figure 17: Smiley Image One of the first SAL images formed as part of this project. The target is only a few millimeters in dimension. The retro reflector target is the bright spot for PRA focusing. Severe ghosting is present in the image.

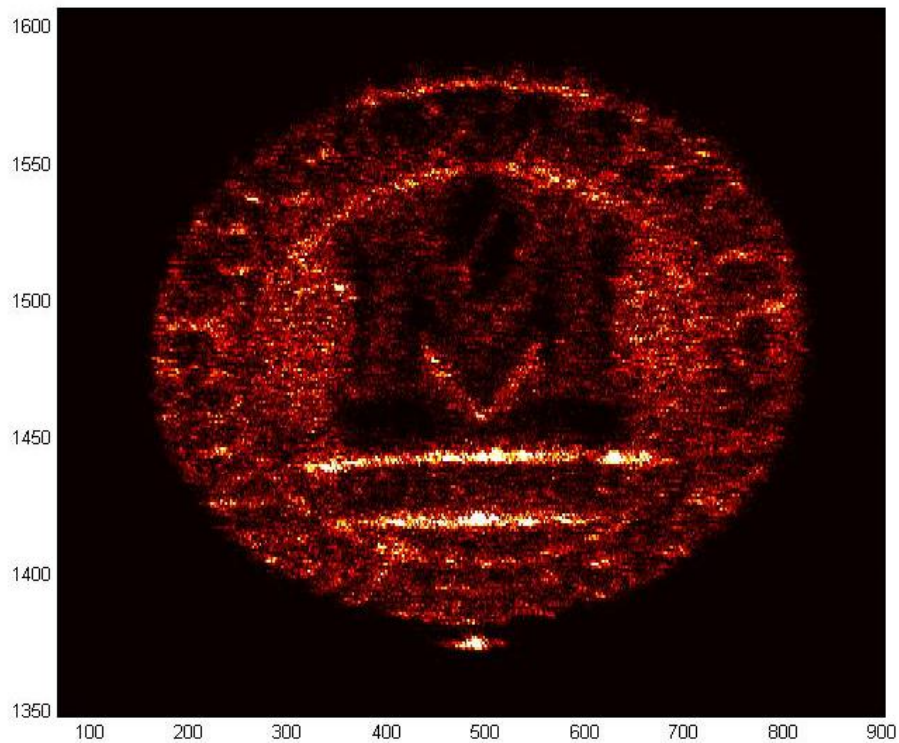


Figure 18: MSU Lapel Pin A SAL image form early in the research focused with PGA. False orange coloring. Some lettering can be seen around the border. This was the best result obtained at this portion of the experimentation with the imaging process.

### The Dragonfly

The most remarkable example of SAL imaging performed during the work of this thesis was a dried dragonfly specimen, Figure 22. The dragonfly was mounted using a needle on the end of a wooden stick. This allowed the dragonfly to remain off of any surface. A cardboard housing was then put around the dragonfly to keep it from moving as its gossamer wings were very sensitive to airflow.

Images were formed of the dragonfly using a circulator operating at 168mW and a fiber array operating at 900mW. The two imaging set ups produced essentially identical

images shown in Figure 22. The dragonfly was imaged at a distance of 1.5m. 2048 shots were taken with the SAL collection program outlined in the previous chapter with steps of 10 microns. The range and cross range parameters give a pixel size of ~50 microns by 50 microns before filtering.

### PGA Success

The PGA was used with great success on the dragonfly specimen. Several hundred rows of the image were used corresponding to the ranges of the location of the dragonfly. The maximum cross range window was used in order to include the highest frequency errors in the correction possible. Up to seven iterations of the PGA were necessary to obtain a quality result. Overall, the performance of the PGA on a completely diffuse target was a powerful demonstration of its utility. Figure 19 shows the dragonfly image before any phase correction – the image is worthless!

### Correction of Large Phase Errors

The phase error estimate for the dragonfly is shown in Figure 20. The large amplitude of the phase error correction is evident as well as the high frequency content of the error. The associated point spread function is shown in Figure 21. The width of the point spread function is seen to extend up to one hundred pixels in width. This explains the defocus in the uncorrected SAL image.

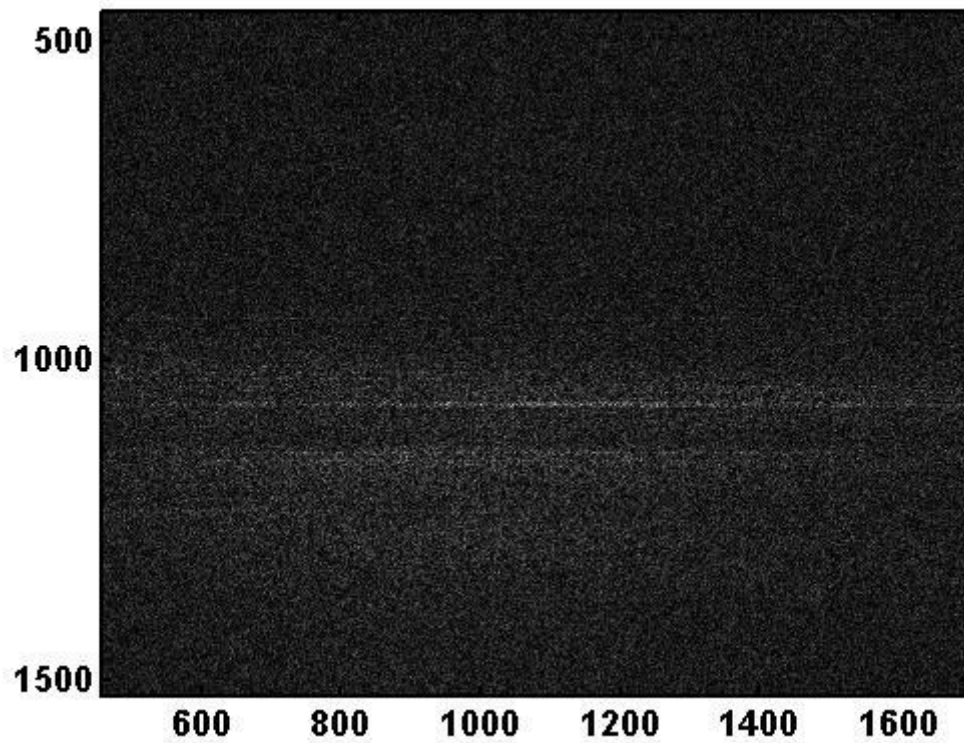


Figure 19: Unfocused Dragonfly The compressed SAL data for the dragonfly before the PGA is basically noise.

#### Further Processing

The post processing of the dragonfly provided some improvement in the image quality. This included a 2x2 filtering of the pixel magnitude to remove some speckle effects and also adjusting the color map to improve the contrast.

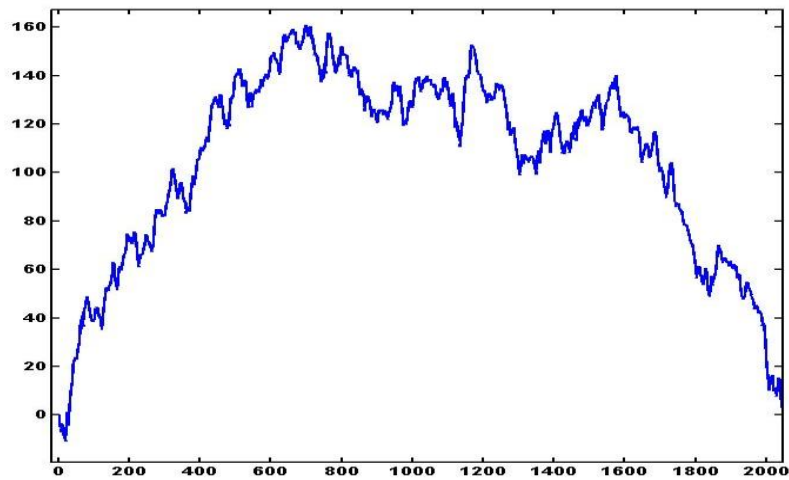


Figure 20: Phase Error The large phase correction is shown. Note the generally quadratic phase error underlying the higher frequency errors. The left axis shows radians – variation of several hundred radians is evident.

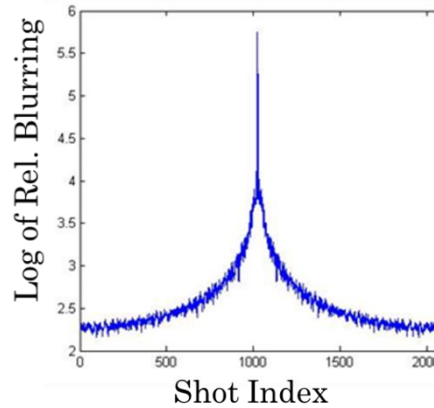


Figure 21: Associated PSF The point spread function associated with the corrected phase error (FFT of Figure 20 data) on a log scale.

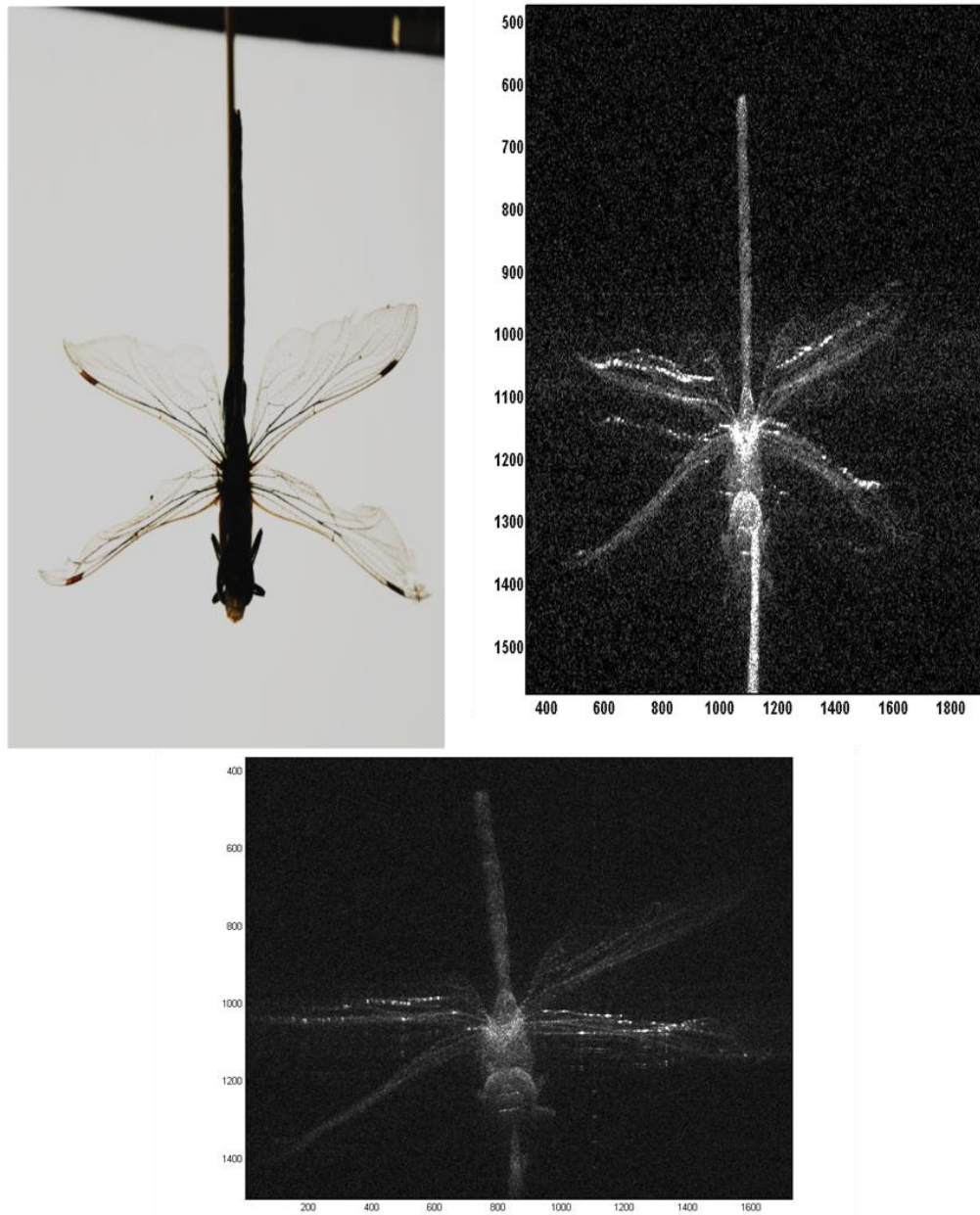


Figure 22: Dragonfly A high-resolution photograph (left) taken of the dragonfly for comparison and the finished circulator based SAL image (right) of dry dragonfly specimen and array based (allowing higher optical power) SAL image (bottom).

### Electronic Chip

Another example of SAL imaging, under the exact same conditions as the dragonfly, was the imaging of an electronic chip, Figure 23. The different image quality is an example of SAL performance when dealing with plastic surfaces and more specular metallic surfaces. The weaker return signal off of those surfaces explains the decrease in contrast. The image is shown below in Figure 23.

This image serves as a reminder that the magnitude of any pixel in a SAL image is related to reflectivity. The four chunky black squares in the image were made of black plastic – which reflects poorly. The hash marks on the bottom and the bright spots throughout were metal connectors or surface mount chips and therefore provided strong return. The rest of the chip, in hazy gray, is the green plastic substrate material.

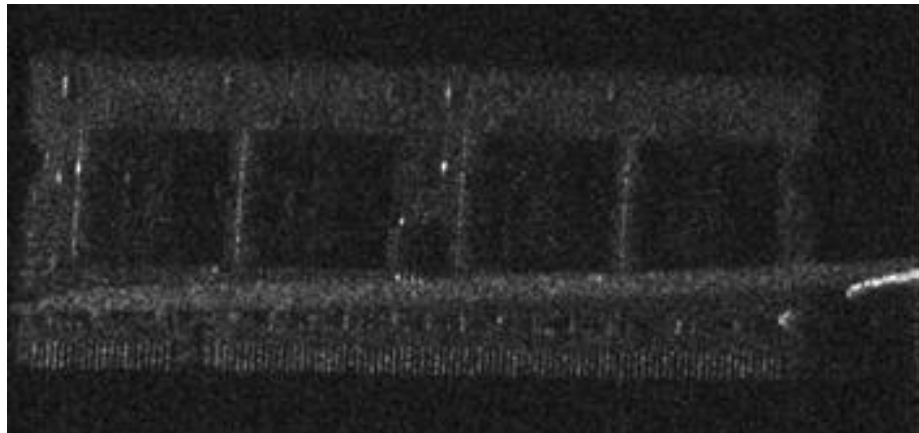


Figure 23: RAM Chip SAL image of electronic chip demonstrating SAL performance with plastic and metallic surfaces. The hash marks on the bottom of the image are electrical connection leads approximately 0.5mm in width with 0.5mm spacing between them.

Discussion

The dragonfly example is the culmination of several months of SAL imaging experimentation. The dragonfly relative to the smiley face demonstrates how far the SAL imaging process has come as part of this project. The RAM chip shows that SAL can work on a variety of materials. Minimal filtering was done on the images to improve image quality beyond the PRA or PGA correction. The success of the PGA on the dragonfly and chip target provided the confidence to begin experimenting with IFSAL, described in the next chapter.

## INTERFEROMETRIC SAR

### History and Introduction

Interferometric SAR (IFSAR) was first proposed by L. Graham in 1974 as a way to extend SAR imaging to support the re-construction of three dimensional surfaces. By the 1980s, IFSAR was beginning to mature into a go-to terrestrial mapping technique [2]. While IFSAR has scaled well to shorter radar wavelengths, the technique has not been demonstrated in the optical regime as Interferometric Synthetic Aperture Ladar (IFSAL). This chapter will introduce, to the author's knowledge, the first demonstration of this technique.

IFSAL uses the interference pattern of two SAR images taken from parallel synthetic apertures separated by a baseline to reconstruct a surface topography. The connection between the interference pattern and topography is explained below. The primary difficulties of IFSAL include phase coherence between the two images (to yield a quality interferogram) and two dimensional phase unwrapping (a difficult problem necessary to derive the topography from the interference pattern) [1,2].

### IFSAL Geometry

The textbook discussion of IFSAL, in the opinion of the author, fails to efficiently explain the physics behind IFSAL [1,2]. The Zero-Phase Plane Model, developed as part of this thesis, is a simple tool for demonstrating the principles at work in IFSAL.

### Textbook Explanation

The textbook descriptions rely on complex collection geometries to describe the effect. For this reason, the literature on IFSAR was marginally beneficial. Much of the difficulty in the literature is likely due to Equations attempting to account for the complexity added by parameters of satellite or aircraft flight paths. Nonetheless, the difficulty prompted a search for better ways to understand IFSAL.

### Zero-Phase Plane Model

The Zero-Phase Plane (ZPP) model was developed as a way to more directly access the physics of IFSAL. The basic schematic describing the ZPP concept is shown in Figure 24. This model acts to describe how the interference pattern of two SAL images separated by a baseline encodes information about height of the scene off of the ZPP. As discussed further in the Projective SAL chapter, a SAL image is essentially a projection of a three dimensional scene into a two dimensional plane defined by the aperture track and the beam direction. In the ZPP model, the ZPP and the two SAL imaging planes are parallel. Further, the ZPP sits between and equidistant from the two SAL imaging planes.



This Equation implies that any point target a height  $h$  off of the ZPP will result in a differential phase measurement (mod  $\pm\pi$ ) that will manifest in the interference of the two SAL images.

### Collection Set-Up

Two different collection methods were used based on equipment available. Initially only a single fiber Tx/Rx station in the circulator configuration was used to image the penny. This configuration required two passes. Later the fiber array allowed for one pass collection of IFSAL data for the sea shell.

### Two Pass

The synthetic aperture track was parallel to the surface of the table requiring a baseline in the dimension normal to the surface of the table. Thus the two pass collection method required two SAL images of the same object to be formed from different heights relative to the optical table during two different scans. Compared to a single pass collection, this method has the disadvantages of requiring twice as long to take the data, the introduction of different shot to shot phase errors between the scans, and image registration errors in both range and cross range. Despite these shortcomings, the ability to adjust vertical height of the fiber with a linear stage allowed for control of the vertical baseline,  $B$ , offset between the apertures relative to the one pass collection with the fixed distances of the fiber array. This adjustment was useful for tuning the baseline.

### One Pass with Fiber Array

The fiber array was used to facilitate one pass collection. This allowed two SAL images separated by a baseline to be formed simultaneously during one scan. The stack of the fiber array was oriented normal to synthetic aperture track. The baseline in this case was set as a multiple of the 250 micron distance between fibers in the array. The beam was transmitted out of one of the central ports while the collection was performed on the end ports of the fiber array. A patch cable was used to add range (time delay) to one of the collection paths before the two signals were combined and subsequently mixed with the LO path (time delay results in beat frequency separation). The resultant signal was put on the detector with the range data from the two channels separated in frequency. The two range profiles were then cut out of their respective locations in the overall range profile to construct two independent datasets. An update for the fiber array experiment is shown in Figure 25.

The one pass collection has the advantage that the two images formed are subject to the common piston phase error. Errors such as fiber length fluctuation would remain different for the two paths. Overall the phase errors are more common mode. The drawback of this technique was the lack of adjustability in the baseline which ultimately limited the height sensitivity. This could be overcome with a larger fiber array (arrays of up to 96 ports are available).

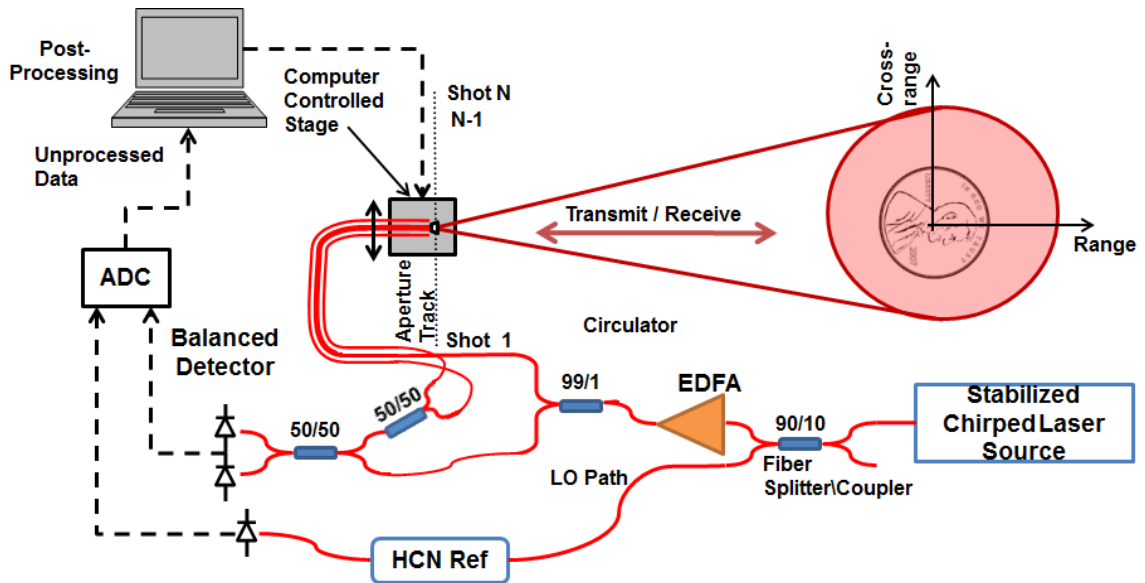


Figure 25: Set Up with Fiber Array The updated experimental set up including fiber array. The 99% transmit path is sent to one output of the fiber array (represented by thicker center line of path to the Tx/Rx). The two thinner, outer paths represent the two return channels, separated by a baseline, from the fiber array. The two channels are then combined (50/50 2x1), mixed with the LO (50/50 2x2) and the signal is detected.

### Scene Background

For basic SAL images, a background to the target providing no return is preferable to increase the contrast of the target against the background. The issue of scene background is more nuanced for IFSAL. IFSAL relies on the ability to unwrap the phase of a target over the extent of that target to derive its topography. Thus a return from all points on the target above the noise floor is ideal. If this condition is not met inside the target, averaging of the phase will help to smooth the interferogram and may still allow for a decent unwrap. Outside of the target, there are two methods to deal with poor return that may degrade unwrap performance. The first method is to introduce a flat, diffuse background such as white paper to provide good return and hence good phase

measurement in place of poor return and noisy phase measurement. This method was employed in the case of the sea shell as in Figure 29. The second option is to create a mask based on the target intensity in each SAL image and zero the phase of all points in the image outside of the continuous target region before phase unwrapping. This method was used in the case of the penny. In Figure 26 left, the image was used to create a mask prior to unwrapping.

### Post-Processing and MATLAB Code

The code used for two pass IFSAL collection was identical to that used to form SAL images – it just had to be run twice to form the two images for IFSAL. The one pass IFSAL code differs from that used for SAL image collection by adding the code to cut out two portions of range and allotting memory to save those two portions accordingly. The post processing is where the “interferometric” of IFSAL happens. The interference is a multiplication of one complex SAL image by the complex conjugate of the other. The phase information is then extracted using the angle function in MATLAB. The two steps necessary outside of the interference are image registration before interference and phase unwrapping after interference. The individual SAL images are focused prior to IFSAL processing.

### Image Registration

Image registration, or spatial alignment of two images, is vital to IFSAL. Each complex valued pixel in one SAL image has a phase value that needs to be interfered (i.e.

subtracted) from the same pixel in the second SAL image. The proper method is to register the two images before interfering them.

Extremely complex registration techniques are outlined in the literature [2]. The most basic method however, is to find the peak in the correlation of the intensity profile of the two SAL images. The location of this peak estimates the offset of one image to the other down to a pixel. This provided a first order estimate for registering the images using a Fourier based shifting method. Sub-pixel registration adjustments were performed with the same Fourier shifting technique with judgment of registration by eye. A metric judging the quality of the interferograms from a quantitative perspective may be a way of automating the registration process. The correlation and shifting code are provided in Appendix A.

### Two Dimensional Phase Unwrapping

Phase unwrapping is required to convert the interferogram phase information to a full topographic map. The interferogram values are “wrapped” between  $\pm\pi$ . Unwrapping this reveals the overall surface profile of the target. Unwrapping a one dimensional signal is well defined. Essentially whenever the wrapped signal changes by  $\pm\pi$ , the unwrapped signal is allowed to continue past those limits in a consistent manner [22].

Two dimensional phase unwrapping, however, is highly ambiguous. The root of this ambiguity is that unwrapping in two dimensions cannot be accomplished by unwrapping one dimension and then the other (i.e. the process is non-commutative). Textbooks have been written about two dimensional phase unwrapping (a problem not

limited to SAR and SAL application) [22]. The algorithms vary from semi-analytical to “network flow” and “genetic” algorithms. Two algorithms have been chosen from the large sample of literature to complete the task of two dimensional phase unwrapping for IFSAL data. The Least Squares method was chosen because it could be coded by the author (an educational experience). The Network Flow algorithm was chosen as a professional level example of modern unwrapping techniques. Together, the two provided some basis of comparison of different methods.

Least Squares A fast, yet still robust method for phase unwrapping was the Least Square formulation [2,22]. The program to carry out the algorithm was coded by the author in MATLAB from the above references and is included in Appendix A. The method derives a driving function based on the wrapped phase. With this driving function, the unwrapped phase solution is derived to be the least squares solution to Poisson’s Equation on a rectangular grid with Neumann boundary conditions. For a detailed review the reader should consult [2]. It should be emphasized that this method is one of the more transparent methods.

Network Flow The network flow approach uses advanced network flow algorithms to unwrap the phase. Code was used from an online source with experience in IFSAR unwrapping as a way to compare the unwrap result to the Least Squares method [23,24] . Overall, the Network Flow algorithm gave a cleaner result.

### Flat Earth Effect

The flat earth effect is caused by the target resting on a plane that bisects the ZPP at an angle – used to provide range diversity. Thus this plane has height variation that will manifest itself as fringes in the interferogram. Removing the slanted plane from the data reveals the height of the target from that plane instead of from the ZPP. The correct order of this process is subtracting a phase ramp out of each SAL image, filtering the phase as needed, and finally interfering the two images [1,2,22]. Estimation of the phase ramp needed for removal could be facilitated via collection geometry and Equation 6.2. Alternatively, Fourier analysis of the interferogram fringes could also make an estimate of the phase ramp. For the IFSAL image results in the next chapter, the phase ramp was quickly removed in an ad-hoc manner.

### Baseline Considerations

The measured phase difference is linearly related to the baseline magnitude by Equation 6.2. The baseline should be adjusted so that the phase sensitivity (i.e. a height difference of  $h$  between points causes a phase difference of  $\frac{2\pi Bh}{\lambda R_0}$ , Equation 6.2) is less than abrupt phase (surface height) changes. This constraint prevents phase ambiguities in a modulo  $(+/-)\pi$  sense. If a target has a slowly varying height, a larger baseline can increase the sensitivity of the phase measurement without concern that the height will abruptly vary too much and introduce the mentioned ambiguity. If the object has quickly varying height, a smaller baseline will be required to prevent the ambiguity.

Assuming 100 microns between pixel centers (typical for SAL images in this paper) the baseline should be chosen so that maximum height variation in a 100 micron distance would induce a phase variation of less than  $2\pi$  leaving  $B < \frac{\lambda R_0}{h} \xi$ , ( $\xi$  adjustable parameter). While the above derivation implies an upper limit of  $\xi$  of unity,  $\xi$  closer to one tenth was used completely avoid ambiguities and to decrease phase noise sensitivity.

Other points to consider about the baseline include registration and flat earth effects. Larger baselines will induce larger registration problems due to the larger difference in target perspective. This is one reason to keep the baseline below a value maxing out the sensitivity. The flat earth fringe frequency also put an upper limit on the baseline. If the flat earth fringes become so fast that they are occurring within a pixel, then the phase will become essentially random as the fringes will be under sampled and impossible to remove. In contrast to these upper limits on baseline, too small of a baseline will result in little or no phase variation and an unusable interferogram.

## IFSAL RESULTS

### Two Pass vs. One pass

The penny data was collected with a two pass collection system. The baseline was adjusted (with micron resolution up to 3cm) using a linear stage with an attached micrometer (stage necessary to create 2mm baseline for the penny). Despite this advantage, the two pass system required the time to take two SAL images and both suffered from different phase errors which affected phase coherence. The sea shell utilized a faster and more phase coherent one pass system with the fiber array. The drawback to the fiber array was the lack of baseline adjustability and 650 micron maximum baseline (phase sensitivity not enough for small penny height variation). The ideal IFSAL system would be one pass with an adjustable baseline.

### Target Considerations

The targets of interest for IFSAL differed from SAL. While the goal of SAL is generally a high contrast image, IFSAL benefits from a good return across a whole surface. A steady return from the surface will ensure valid phase measurement at all points and a better interferogram. A diffuse surface like a white spray painted metal or a chalky sea shell is a good option for this purpose. The drawback was the need to use the PRA instead of the PGA as the entirely diffuse targets were poor candidates for the PGA.

### Registration of SAL Images for Interference

Proper registration yielded the interferogram in Figure 26. In the case of the penny, the large baseline and two pass collection introduced serious registration errors that made the manual registration time consuming. The SAL images had to be shifted by tens of pixels in both dimensions to acquire reasonable interference. The smaller baseline of the seashell and one pass collection made registration task much easier with a shift of only a few pixels required.

### Lincoln Penny Results

The demonstration of IFSAL was the most exciting result of this thesis. The technique was written off by a visitor to Spectrum Lab in October of 2011 as impossible because, “The phase de-coherence would be too great.” The success of the technique is due to the mechanical stability of the synthetic aperture track and phase coherence of the CR system.

The penny was imaged with 168mW of optical power at a distance of 137 cm using the fiber circulator set up. A chirp bandwidth of 3 THz gave a range resolution of 50 microns. The baseline used was 2.905 mm yielding, from Equation 6.2, a phase-height sensitivity ratio of  $\sim 2\pi$  per 100microns height variation (100 microns is an estimate of maximum surface height variation). 2048 shots were taken during the collection process with 10 micron steps. A two-pass collection was used for the penny.

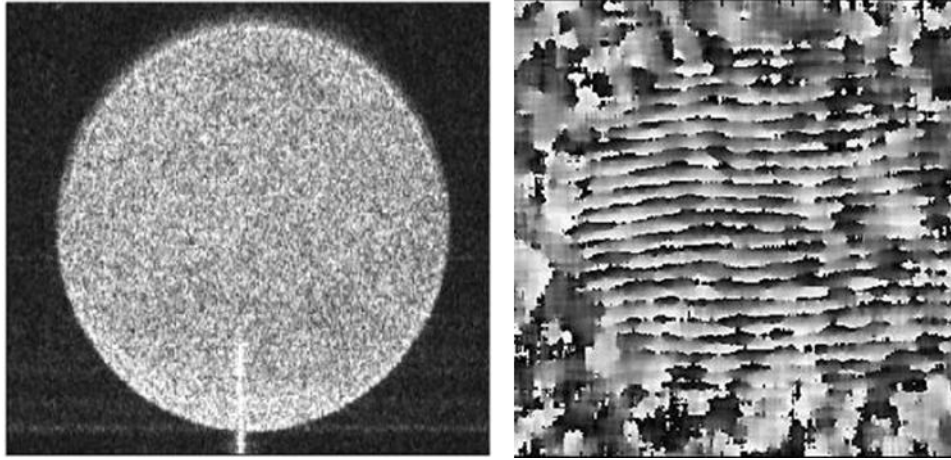


Figure 26: Penny Image and Interference Pattern Single SAL image of white painted Lincoln side of US penny to be used for IFSAL (left). Note the generally consistent return across the surface and poor return outside the penny. Interferogram of IFSAL data (right). The flat earth effect has not been removed and is responsible for the fast fringing. The penny information is contained in the deviations along those fringes.

### Multilook IFSAL Processing

A multilook approach was used to find the portion of the aperture with the best phase coherence to provide a quality interferogram. Interfering several images formed from quadrant subsections of the collected data (1024x1024 pixels each) had an averaging effect that helped to improve the image quality. This was necessary to average the noise in the Least Squares unwrap. The averaging came at the cost of halving resolution as the image was formed from four data subsets [1,2].

### IFSAL Unwrap Methods Results

Both unwrap methods outlined in the previous chapter were employed for comparison in the unwrapping of the penny. The least squares method had the advantage of taking only a few seconds to compute the unwrapped image. The network flow

algorithm took up to an hour to unwrap the image. The penny surface height variation (flat portion to the top of the Lincoln's head) was measured with calipers to be a maximum of 200 microns. The scaled topographical images below are then reasonable approximations to the penny topography with maximum height variation of about 150 microns calculated.

#### Least Squares IFSAL Unwrap Result

The result of the least squares method is shown in Figure 27. The waviness of the image around the edges of the penny can be attributed to the smooth solution the method tries to achieve in solving Poisson's Equation.

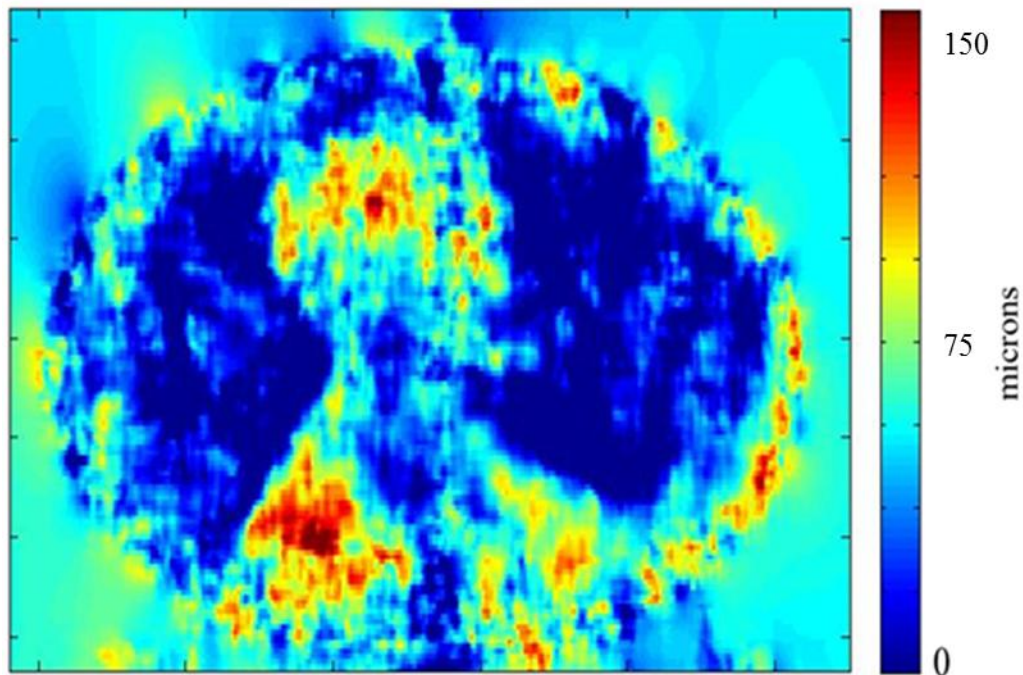


Figure 27: Least Squares Unwrapped The result of the least squares algorithm – the solution gives a wavy effect attempting to correct the ambiguous phase returns of the sharp penny edge. Lincoln's profile is still evident.

### Network Flow IFSAL Unwrap Result

The network flow algorithm provided better unwrapping results shown in Figure 28. This can be attributed to the cell by cell nature of the unwrapping which prevents noise in one portion of the image from affecting the unwrap in another portion as was the case with the least squares method. The smoothness of the image is also much better with elevated portions of the penny appearing as more continuous regions. This is in contrast to the oftentimes jagged nature of the least squares unwraps.

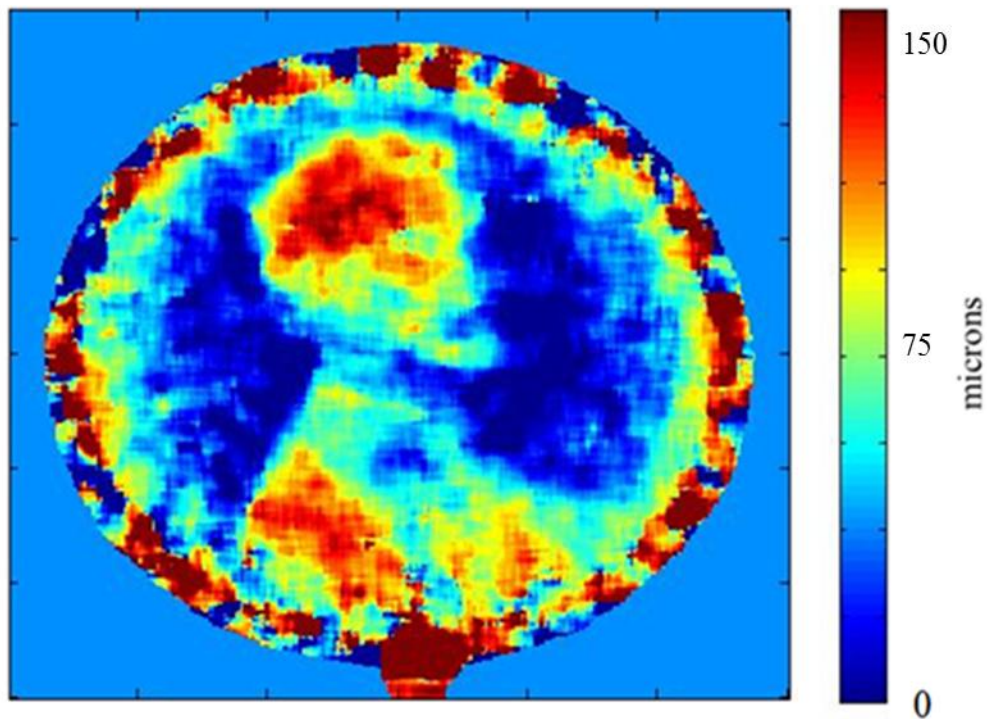


Figure 28: Network Flow Unwrapped Network flow unwrapped penny topographic map. The phase outside the penny / retro reflector (red spot at bottom) was zeroed out prior to unwrapping. The jagged effect at the penny edge is due to ambiguities from the height variation exceeding the baseline support. This shows a less distorted unwrap than the Least Squares method.

### Sea Shell Result

A sea shell, Figure 29, was also imaged using the IFSAL technique. This target was chosen for its diffuse chalky surface and its larger scale topography than the surface of the penny. The height variation ( $\sim 1$  cm maximum) of the surface lead to an estimate for a baseline of  $\sim 500$  microns. Luckily, the fiber array closely matched this specification and allowed a one pass configuration. The shell was imaged with a greater 900mW of optical power through the fiber array at a distance of 75 cm. The chirp bandwidth was the same as for the penny. The baseline was 650 microns giving a phase-height sensitivity ration of  $\sim 2\pi$  per 1 mm height variation. 2048 shots were taken during the collection process with 10 micron steps. The registration required to achieve a good interferogram was only a few pixels. The final IFSAL image computed using the Network Flow algorithm is shown in Figure 30. The Least Squares method was not attempted based on its poor performance for the penny.

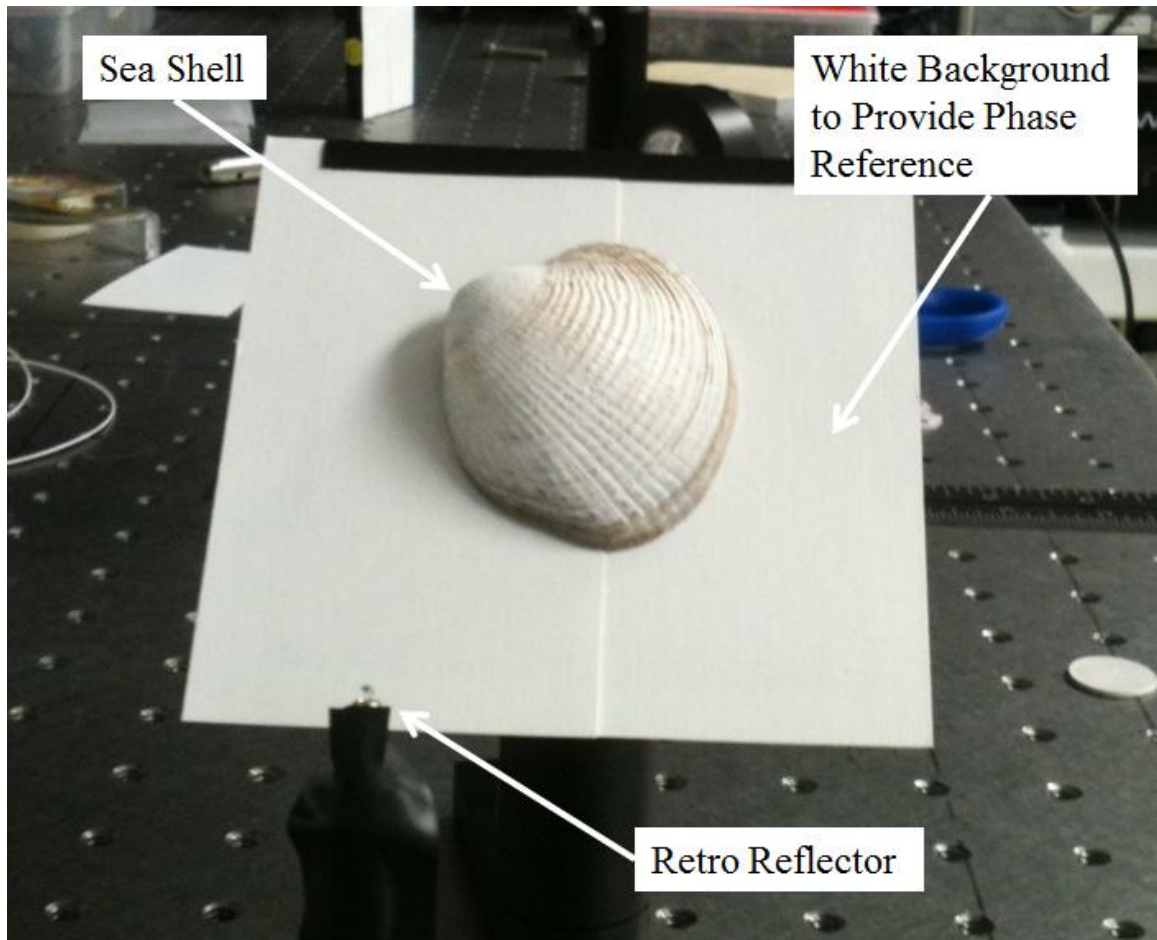


Figure 29: Sea Shell Photo The imaging configuration for the seashell.

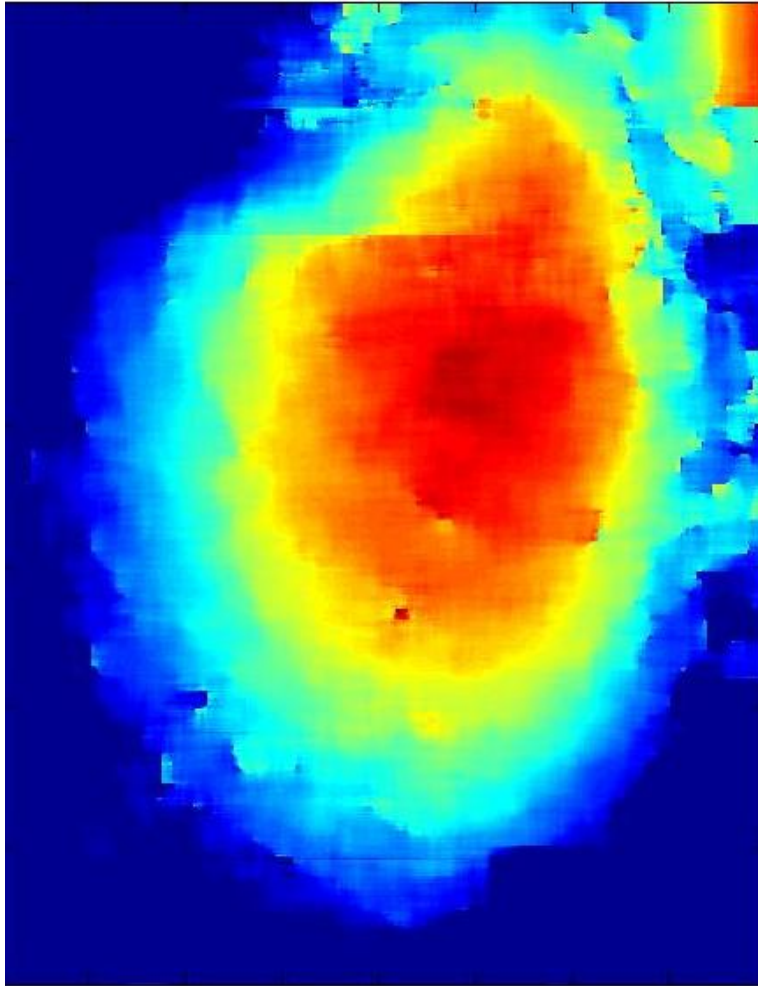


Figure 30: Sea Shell Unwrapped The topographic map of the sea shell. The vertical streaking can be attributed to the block by block nature of the network flow algorithm.

### Discussion

The demonstration of IFSAL was the first of its kind. At the onset, the possibility of coherence of the two images was not certain. Several basic experiments allowed the process of image collection and image registration to be fine-tuned before dealing with unwrapping the interferograms.

## PROJECTIVE SAL

### PSAL Concept

The success of IFSAL prompted the exploration of other three dimensional surface reconstruction techniques. One possibility is to exploit the projective nature of SAL images to serve a basis for reconstruction. This demonstration is meant to show a new way think about how to use SAL images as much as it is meant to prove the concept.

Why have SAR systems not sought to use the projective nature of SAL images? As seen below, Projective SAL (PSAL) requires at least two SAL images, one taken after rotating the set-up a quarter turn about the beam axis. Traditional SAR collection is done from airborne or space based platforms. The rotation requirement is difficult to overcome for reasons of time, feasibility (the satellite orbit is set), or safety (combat zone reconnaissance). These problems essentially come down to the vastly different scales of SAR and SAL. In the case of laboratory SAL demonstrations, the above constraints do not exist. The rotation of the scene about the beam axis only requires the addition of a rotation stage to the scene. Further, IFSAR is a powerful and well understood technique so there has been little effort to develop other 3-D surface reconstruction SAR imaging modes.

### SAL Images as Projections

A SAL image is a projection of the return from a three dimensional surface onto the plane containing the beam and aperture vectors, Figure 31. A single SAL image can

only measure range and cross range. The three dimensional surface is integrated (i.e. projected) over the third coordinate into the plane of the other two coordinates.

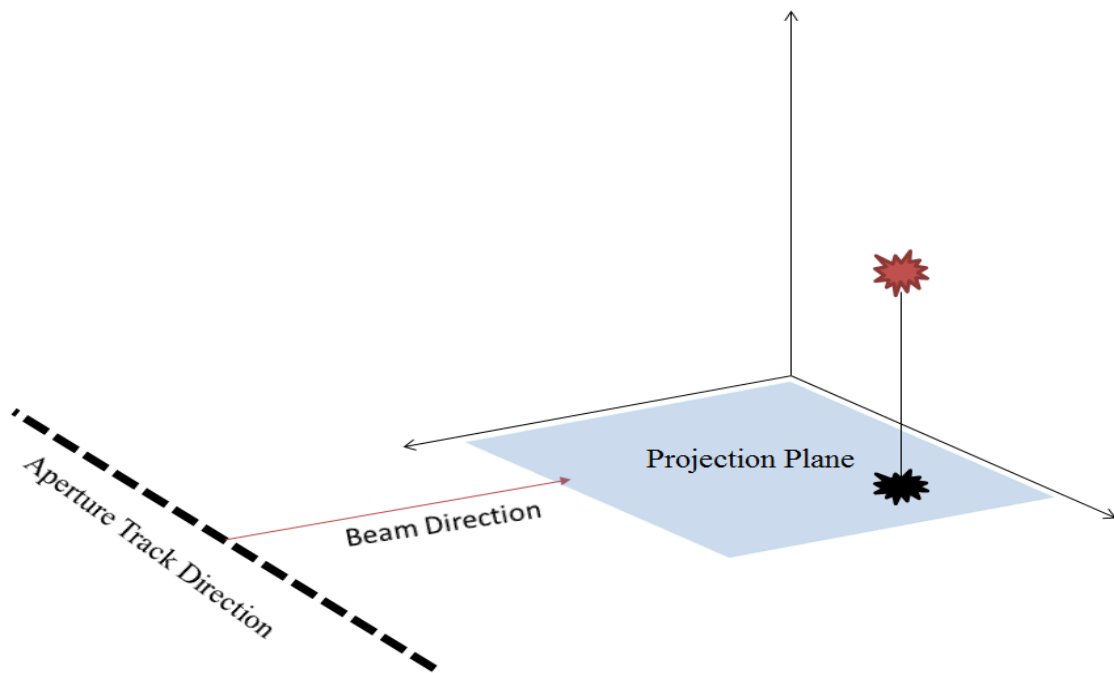


Figure 31: PSAL A The projection of a point scatterer onto the projection plane. The SAL image in the projection plane can only contain information about the cross range and range coordinates – the height off the plane is ambiguous and completely lost in the projection unless an IFSAL configuration uses the phase information.

### Surface Reconstruction from Projections

Operating under the assumption (not good for complex surfaces) that a three dimensional surface can be at least partially reconstructed from two or more orthogonal SAL images, a scheme was formed to prove this concept. The most basic model is that of a single point scatterer. A concept schematic is shown in Figure 32.

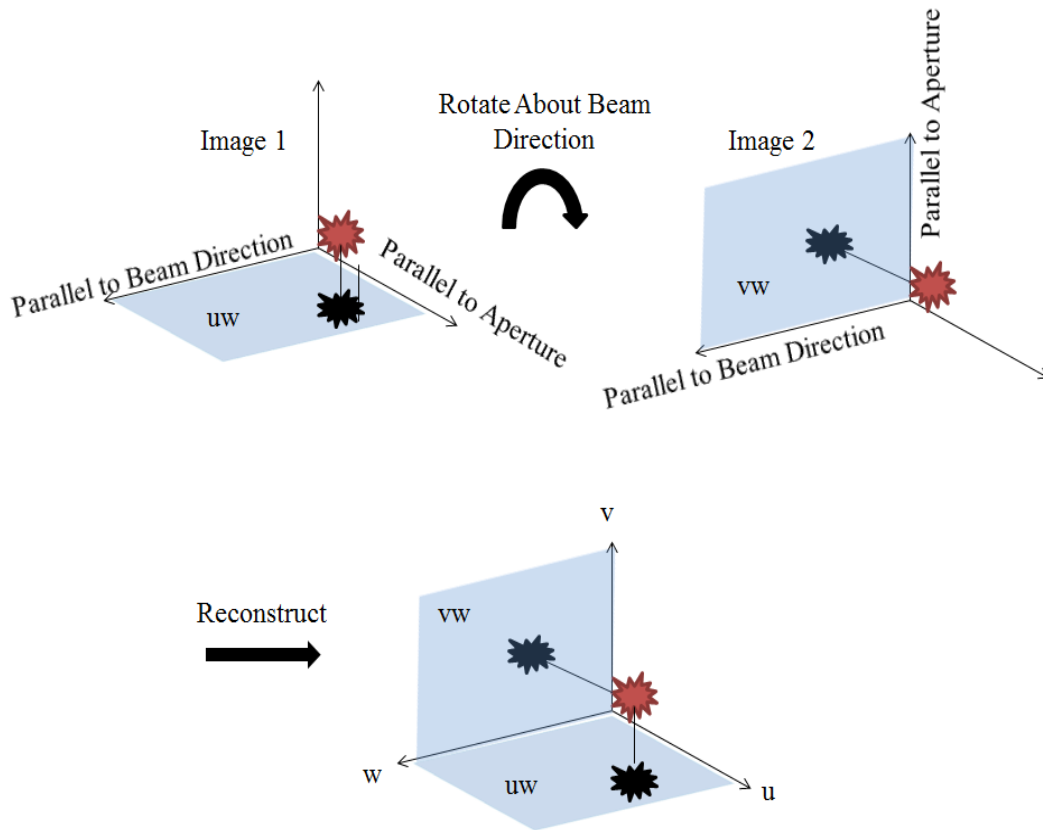


Figure 32: PSAL B Schematic of projection reconstruction concept. Two SAL images collect projections onto the  $u$ - $w$  and  $v$ - $w$  planes (black scatter). This information can then facilitate full reconstruction of the point scatterer location (red) as the  $u$ - $w$  plane provides the  $u$  coordinate, the  $v$ - $w$  plane the  $v$  coordinate, and the  $w$  coordinate is known from the range measurement in both planes.

### Proof of Concept

The concept was shown using a stick – an idealized “line” through three dimensional space. This is one of the most basic examples and avoids ambiguities that arise with curved surfaces. The stick was mounted on a stage that could rotate about the axis parallel to the beam direction as in Figure 33. Taking a SAL image, rotating the stage a quarter turn, and taking another SAL image constituted the collection of two

orthogonal SAL image projections. The two images should contain information to roughly reconstruct a straight line through three dimensions.

### Collection Geometry

The collection geometry described above is shown in the figure below. A way to perform three projections was not found and was not required for the toothpick demonstration. For the line like object, two dimensions were sufficient to show localization of a target in three dimensional space.

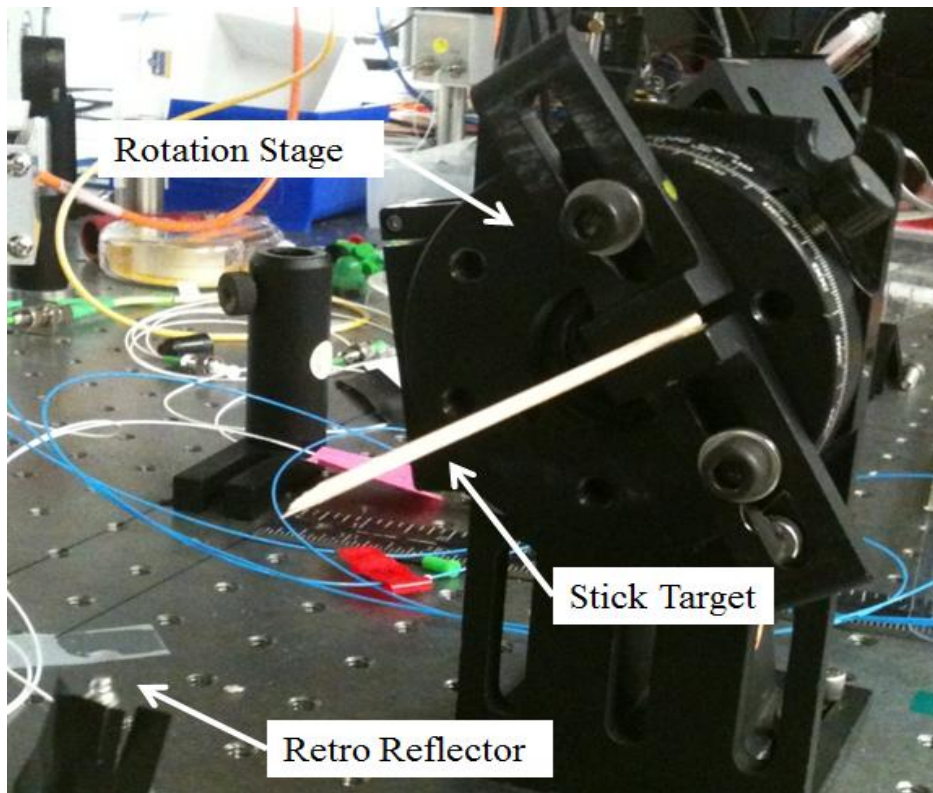


Figure 33: PSAL Photo The stick is mounted on a rotation stage so that two orthogonal projections can be performed.

### MATLAB Code

The MATLAB code used to reconstruct the image is included in Appendix A. The code is somewhat rudimentary as a result of the limited processing available at the time it was originally implemented. Later availability of heavier processing allowed for the higher resolution shown below.

### Result of Toothpick Demo

The stick section was crudely picked out of three dimensional space as shown below. This demonstration was limited by using only two orthogonal SAL projections. Also, the quality of the base SAL images was degraded by nonlinearities in the chirp laser sources that developed during the time the scans of the stick were taken. This explains the poor resolution of the image, Figure 34.

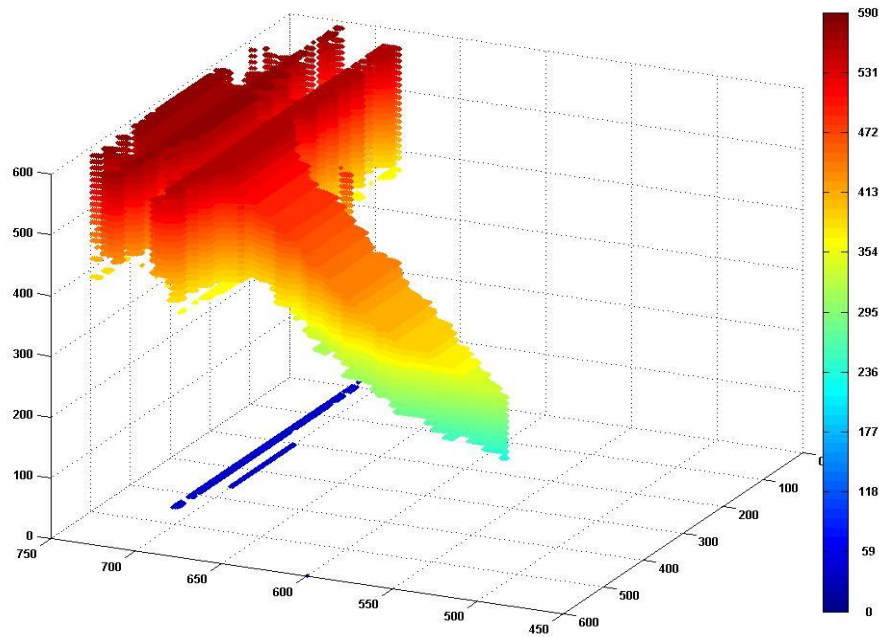


Figure 34: PSAL Result The stick with some of the mounting device showing up behind in the blocky red section in the upper left. The image somewhat captures the sharp point of the stick. The colormap corresponds to height of points in the image (i.e. vertical axis) and serves to visually enhance the 3D perspective. Useful plotting function (not part of standard MATLAB software) for colormapping height information from [25].

## SPOTLIGHT SAL

Overview

Spotlight collection is a popular technique in the SAR community. The primary reasons for this are the relaxation on the cross range resolution limitations which results in an improved photon budget – these two aspects will be discussed further below. While the work discussed in previous sections was performed using a stripmap set-up, this sections serves to verify the feasibility of spotlight mode and to explore some of the inherent advantages that have made it so attractive to the radar community. Spotlight mode experimentation was initially avoided due to the increased mechanical complexity of the set up.

Figure 35 from chapter three is provided again below to highlight the difference between stripmap and spotlight modes.

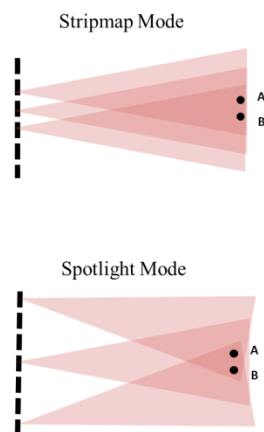


Figure 35: STRIPMAP VS SPOTLIGHT The difference between stripmap and spotlight collection is reproduced from chapter three for clarity.

The chief difference between stripmap and spotlight is that the portion of the angular spectrum sampled is not limited to the angular spread of the spot but instead limited by the ability of the system to view the target from varied angular perspectives [1,2]. This allows the spot size to be reduced as the spot size and angular spectrum available are no longer coupled. The spot size reduction has positive implications in the photon budget. This includes a larger collection aperture and less diffraction.

With the relaxed photon budget, it made sense to experiment with bistatic synthetic aperture configurations in tandem with the monostatic spotlight imaging experiments. A bi-static receive station was introduced along with the monostatic spotlight set so that both configurations could be studied simultaneously. The monostatic transmit/receive station was aboard the motion stage while the bistatic receive station was in a fixed location off of the stage. An extension of the model from chapter three, Figure 36 shows the geometry of the spotlight monostatic station and the fixed bi-static station.

Bistatic SAR is discussed very little in the literature. This is primarily because bistatic SAR's primary utility over a monostatic system is tactical and thus it is in the military's interest to mitigate discussion. The tactical advantage is usually that a passive receive station can remain quiet and operate in more dangerous combat zones while a transmit station maintains a safe stand-off distance. This may have many advantages including photon budget considerations and enhanced resolution with multiple bistatic stations.

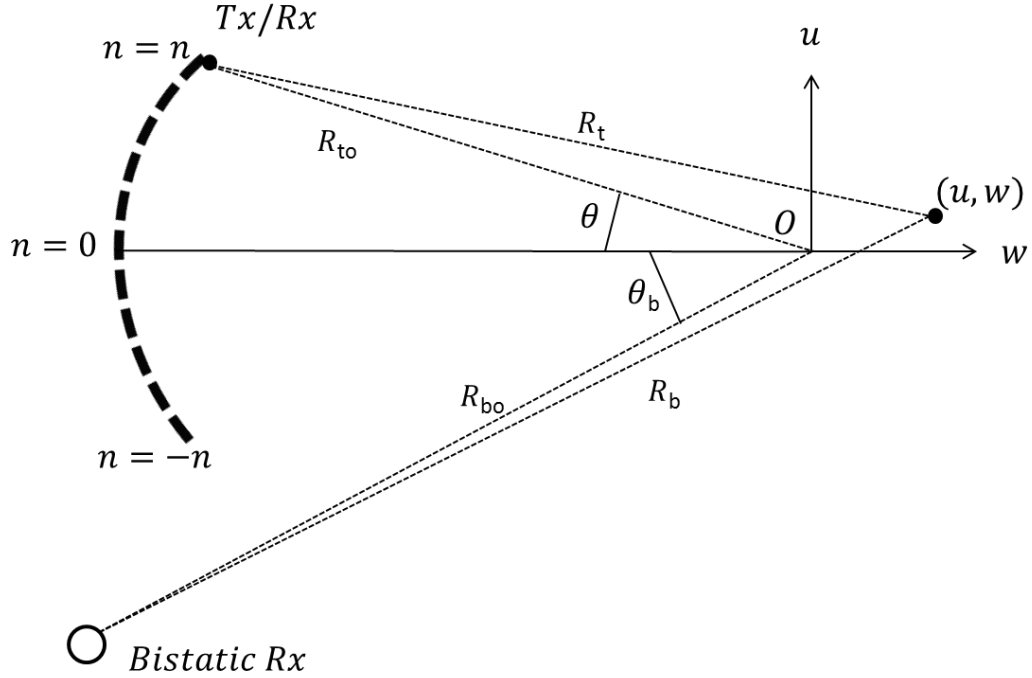


Figure 36: Stripmap/Bistatic Geometry Model for range evolution for a spotlight configuration and a spotlight configuration with a bistatic receive location.

From above, the two path lengths of interest were geometrically derived by the author in Equations 9.1 a,b. Including the range from the Tx/Rx station to the scatterer at  $(u, w)$ ,  $R_t$ , and the range from the bistatic station to the scatterer  $R_b$ .

$$R_t = \sqrt{(R_{to} \sin \theta - u)^2 + (R_{to} \cos \theta - w)^2} \quad (9.1a)$$

$$R_b = \sqrt{(R_{bo} \sin \theta_b - u)^2 + (R_{bo} \cos \theta_b - w)^2} \quad (9.1b)$$

As in previous derivations, the range from Tx/Rx station at position  $n$  to scatterer at  $(u, w)$  and the return or the range onward to the bistatic receiver location can be expressed as in Equations 9.2a,b .

$$R_{ix-rx,n} = 2\sqrt{(R_{io} \sin \theta_n - u)^2 + (R_{io} \cos \theta_n - w)^2} \quad (9.2a)$$

$$R_{ix-b,n} = \sqrt{(R_{io} \sin \theta_n - u)^2 + (R_{io} \cos \theta_n - w)^2} + \sqrt{(R_{bo} \sin \theta_b - u)^2 + (R_{bo} \cos \theta_b - w)^2} \quad (9.2b)$$

These two Equations can be expanded in terms small compared to  $R_i$  and  $R_b$ .

Then the constant terms are removed to leave the dynamic portion of the range evolution for the spotlight case and the bistatic spotlight case.

$$R_{ix-rx,n} \rightarrow 2(u \sin \theta_n + w \cos \theta_n) \approx 2(u \theta_n + w - w \frac{\theta_n^2}{2} + \dots) \quad (9.3a)$$

$$R_{ix-b,n} \rightarrow u \sin \theta_n + w \cos \theta_n + u \sin \theta_b + w \cos \theta_b \approx u \theta_n + w - w \frac{\theta_n^2}{2} + u \sin \theta_b + w \cos \theta_b \dots \quad (9.3b)$$

Finally the range term is plugged into Equation 3.5 and the signal summed over various point scatterers with index  $j$ . The two Equations are functions of  $n$  and  $t$  after having summed over all scatterers.

$$\text{SpotlightPhaseEvolution}(t, n) \approx \sum_j \exp\left\{-\frac{4i}{c}[u_j \theta_n \omega + \kappa t (w_j - w_j \frac{\theta_n^2}{2})]\right\} \quad (9.4a)$$

$$\begin{aligned} &\text{BistaticPhaseEvolution}(t, n) \approx \\ &\sum_j \exp\left\{-\frac{4i}{c}[u_j \theta_n \omega + \kappa t (w_j - w_j \frac{\theta_n^2}{2})]\right\} \exp\left[-\frac{2i}{c}(\omega + \kappa t)(u_j \sin \theta_b + w_j \cos \theta_b)\right] \end{aligned} \quad (9.4b)$$

The spotlight phase evolution bears a strong resemblance to the Fourier kernel of interest with the exception of the quadratic term in the stepped angle  $\theta_n$ . This is interpreted as quadratic range migration that can be corrected by polar formatting the range dimension.

The bistatic expression of Equation 9.4b has an added exponential, the last term, which includes a constant and a time dependent contribution from each point scatterer.

The time dependent portion seriously affects the range compression of scatterers.

Although there is no analytical way to remove this term, it can be noted that the term is the same for each shot index  $n$  and therefore is a good candidate for removal by PGA. The term introduces a cross range invariant PSF to the range dimension. The results of this assumption and application are seen in Figure 40.

### Considerations

#### Sampling

The cross range sample spacing constraint is identical to stripmap mode – one half of the width of the real aperture. However, with the relaxation of the spot size, the real aperture can be larger in spotlight mode. In general the step spacing is about five times that of the bare fiber stripmap mode collection yielding a spotlight step spacing of ~50 microns.

#### Polar Formatting

One downside of spotlight SAL is the requirement of polar formatting. As the sampling is performed to a polar grid, the Cartesian approximation is invalid. This requires post processing to resample the polar data to a rectangular set appropriate for compression by the 2D FFT. This step can be rather be computationally cumbersome and also require over sampling in cross range to better support interpolation in the formatting process [1,2].

#### Spotlight Cross Range Resolution

The cross range resolution is described by Equation 9.5. The fundamental

dependence is on the amount of angle sampled as in Chapter 3. However, the length of the synthetic aperture is independent of the constraint of the target remaining in the beam spot. Similar to the derivation in Chapter 3, the range dependence is removed yielding a limit on angular spectrum sampled – in this case the limit depends on the angle the spotlight beam sweeps out. The caveat again is that angular sampling rate corresponds to the angle subtended by half of the real aperture diameter- which sets the step spacing.

$$\rho = \frac{\lambda}{2\Delta\theta} \quad (9.5)$$

With the  $\sim 50$  micron range resolution of the CR system, less than 1 degree of angular variety is needed for commensurate cross range resolution. At 5 degrees, the cross range resolution is below 10 microns. One application of the ability to have much higher cross range resolution might be speckle averaging in that dimension. The increased resolution might also translate well to IFSAL.

### Photon Budget

As mentioned, the photon budget of spotlight mode is vastly improved. A spot size of 30 cm reduced to a 1 cm spot increases the amount of intensity delivered to the target nearly 1000 fold. The improved photon budget on the transmit side has the potential to increase SNR or to allow for greater ranges to target. The decreased spot size also translates to a larger real aperture. A real aperture size of one millimeter would improve the amount of collected light up to 10,000 fold. Taken together, the improvements on the Tx/Rx sides could provide up to 70 dB increase in SNR for an identical target! This in turn could provide dramatic increase in the range to target

possible with acceptable SNR – a graphical analysis of the possibilities is provided below.

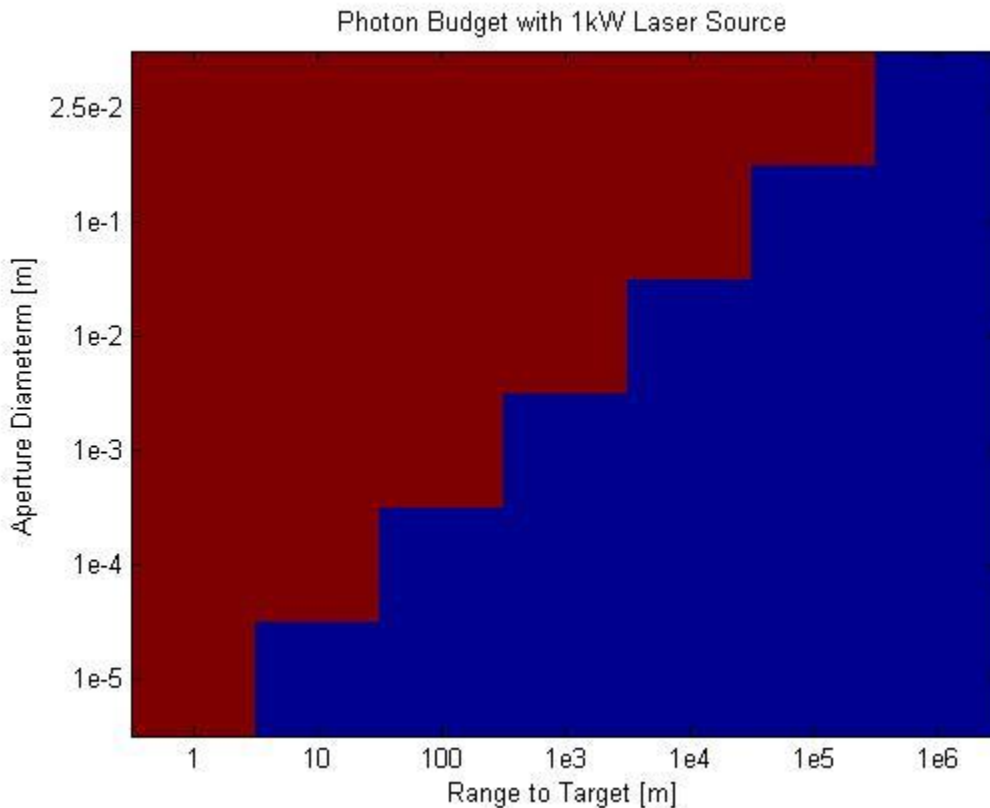


Figure 37: Photon Budget The red portion shows return above acceptable levels (commensurate with analysis in Chapter 3) while the blue is below that threshold. As can be seen there is a linear relationship between aperture diameter and range in the photon budget. Imaging of satellites from earth (500km) via spotlight SAL might require a 1m diameter aperture (with a 1 kW CW laser source). Graphic created with Equations 4.1 (a-c) provided in chapter 3.

### Polar Format Implementation

Polar formatting attempts to re-cast the polar gridded spotlight data as a Cartesian data set with minimal error. The relationship between the collected polar gridded and

desired Cartesian data is based on the real space collection geometry while the data sets themselves are in phase space. Thus a geometry driven algorithm is needed to make the correction.

Several different methods have been explored by the SAR community for years – each with varying degrees of computational cost and overall effectiveness. Two distinct methods are interpolation and scaling. Interpolation, while more intuitive, suffers from high computational cost, cumbersome implementation, and unwanted phase errors manifest in the resampled data. Scaling operations such as chirp scaling or the chirp-z transform avoid interpolation performance issues [26]. Sandia National Laboratory prefers the chirp z-transform for polar formatting as it, “Is a more direct and exact method of calculating a spectral zoom as opposed to zero padding a DFT and interpolating desired point locations [27].”

The cleanest method available from SAR papers was reformatting using the spectral zoom properties of the chirp z-transform. With the collection geometry as the basis for the algorithm, this unique tool allows the quadratic range migration to be corrected by zooming in on different portions of the return phase history at each shot. The majority of descriptions of the chirp z-transform describe “spiral contours” but the zoom operation limits contour values to unity and merely adjusts the starting location and spacings in the kernel relative to a discrete Fourier transform implementation. More thorough discussion can be found in [28].

### Spotlight Mode Experiment

The most difficult aspect of the spotlight mode experiment was to illuminate a single spot at the center of an arc while sweeping out an angular portion of that arc. The collection set-up described below has been effective on the optical table but would be difficult in a real world setting.

The eased constraint on the real aperture size allowed for the spot to be more focused on the target. A spot size of  $\sim 3\text{cm}$  diameter was used at a 4.6m standoff distance. This was achieved using a fiber collimator and a secondary lens ( $f = 35\text{mm}$ ) to slightly spread the semi-collimated fiber output beam. The system was mounted on a cage system for stability. The set-up yields a real aperture diameter of  $\sim 100$  microns. These numbers match with observed step spacing requirements (roughly half of the aperture diameter) to avoid aliasing issues.

### Spotlight Collection Mechanics

The spotlight collection geometry is shown in Figure 38. The stack of the two linear stages and the rotation stage, when connected to the central rotation stage by the constraint arm, allow the transmit/receive station to sweep out an arc while maintaining the spot on the axis of rotation. The linear stage (long line representing the lead screw driven by stepper motor) can reasonably be stepped in equal increments in the small angle approximation.

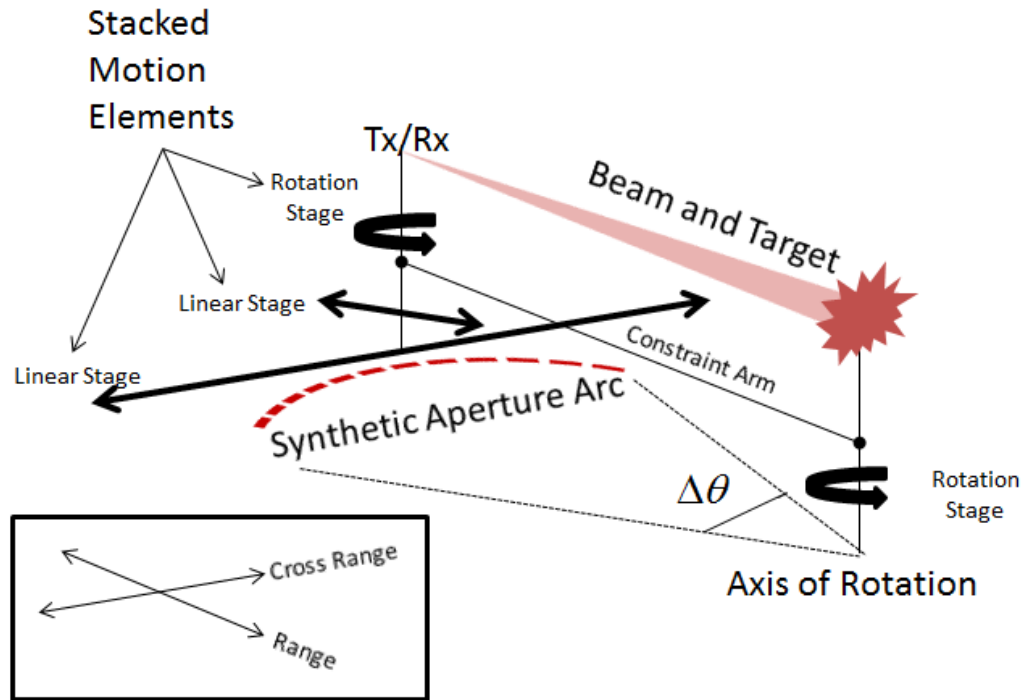


Figure 38: Spotlight Mechanics The spotlight collection mechanics are shown. Several mechanics must be stacked in order to facilitate proper beam steering. The rotation stage under the target fixes the rotation axis of the system (line drawn through target) to go through the target (in an imaginary sense) so that the beam does not “walk across” the target during the scan but is also focused on the target center.

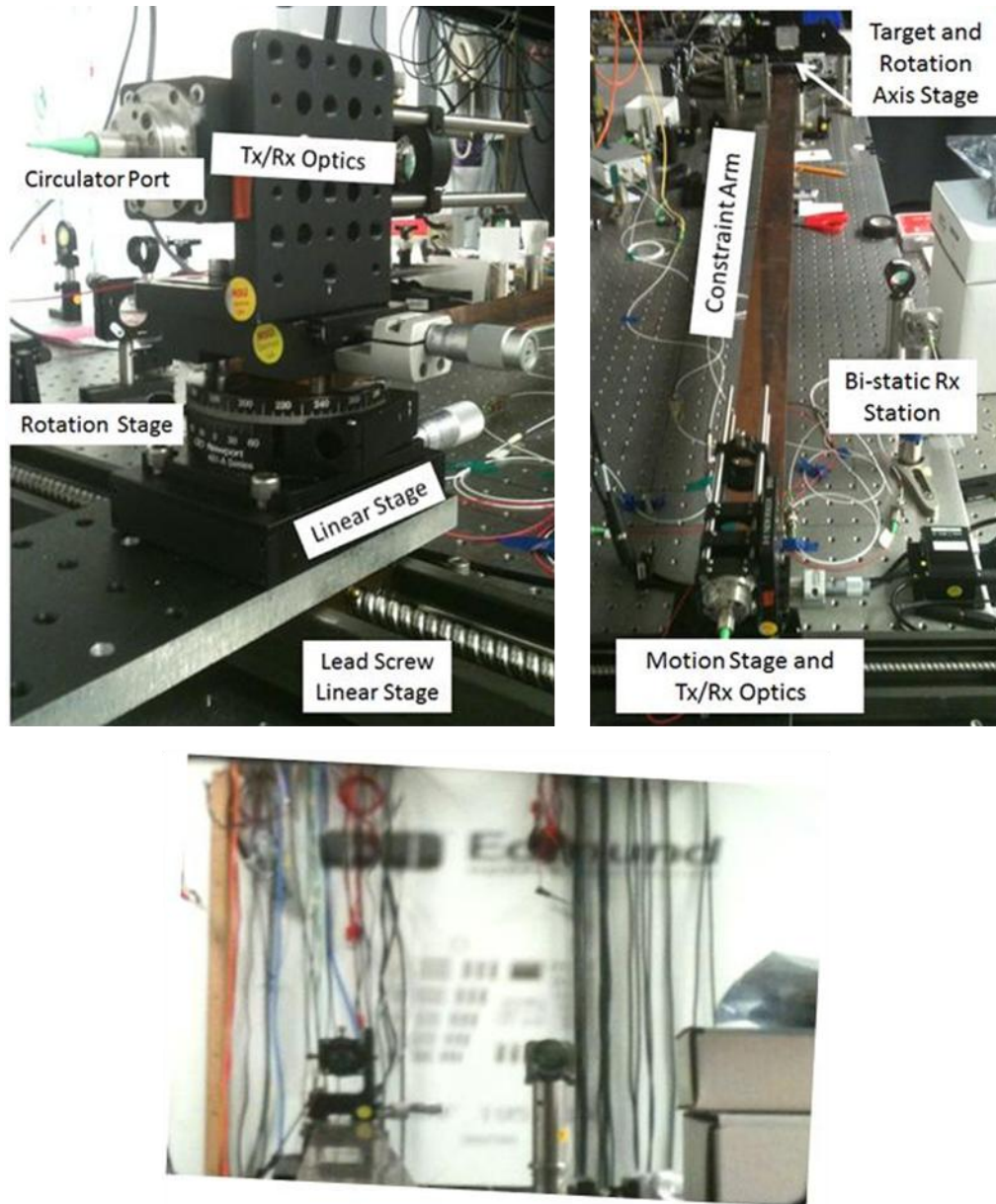


Figure 39: Spotlight Photos Tx/Rx station and required mechanics for arc motion (top left). Overhead view showing Tx/Rx station, bistatic station, constraint arm for arc motion and at the top the target and rotation axis state (top right). Overhead picture of bar target with Tx/Rx station and bistatic station in the mirror reflection (bottom).

### MATLAB Code Used

The MATLAB code used for data collection is largely identical save changing the step size from 10 microns to 50 microns. The majority of the differences for spotlight and bistatic SAL come in the post processing steps – code is provided for these in Appendix A.

### Spotlight Results

Some example images are shown in Figure 40 and Figure 41. Top left in Figure 40 is a bistatic image created with approximately 8 degrees of offset by only using the PGA on the cross range dimension and it shows good cross range focus but poor range correction. The image at bottom right has been range corrected with both the CZT Polar Format algorithm to correct quadratic range migration and the PGA in range to correct the degrading phase term in Equation 9.4b. The polar format and PGA corrections made have been effective in greatly increasing the range resolution. The remaining blurriness is likely due to multipath effects in range from the thickness of the chrome on glass target with paper behind acting as the scatterer. The bar target establishes ~100 micron cross range and ~300 micron range resolution (the calculated physical limit was sub 50 microns in each dimension). This was acceptable considering the increase in mechanical and processing complexity over the stripmap system and the greatly improved photon budget.

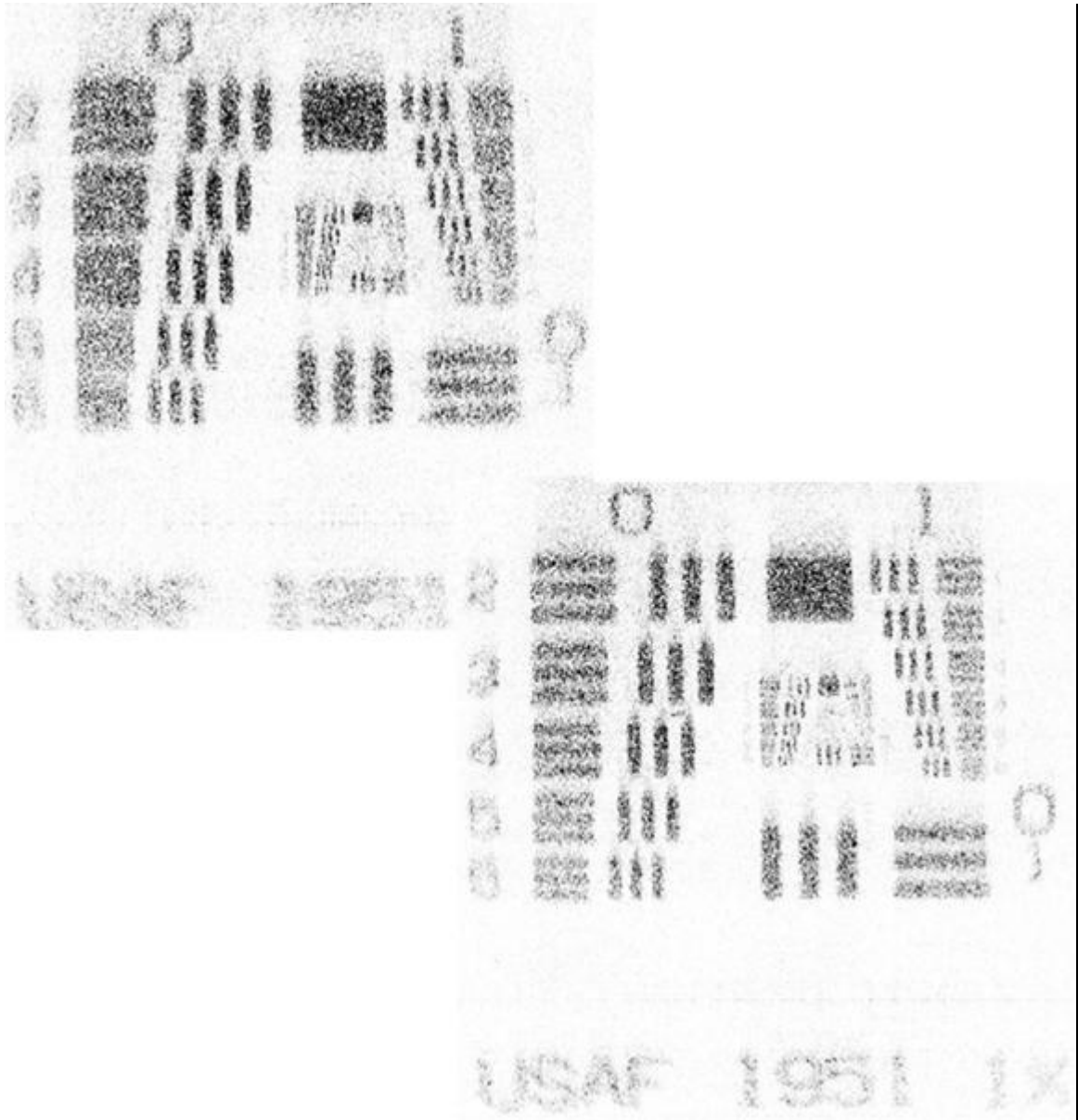


Figure 40: Bar Target Results No range correction processing (top left). Range correction processing with CZT Polar Format and PGA for range (bottom right). Both are bistatic spotlight SAR images. Colors inverted for clarity – black shows strongest return.

Figure 41 shows an example of the high resolution possible with the spotlight system and some advantages of the improved photon budget over stripmap mode. The improved photon budget is enough to image features not seen in stripmap mode such as the lettering on top of each integrated circuit.

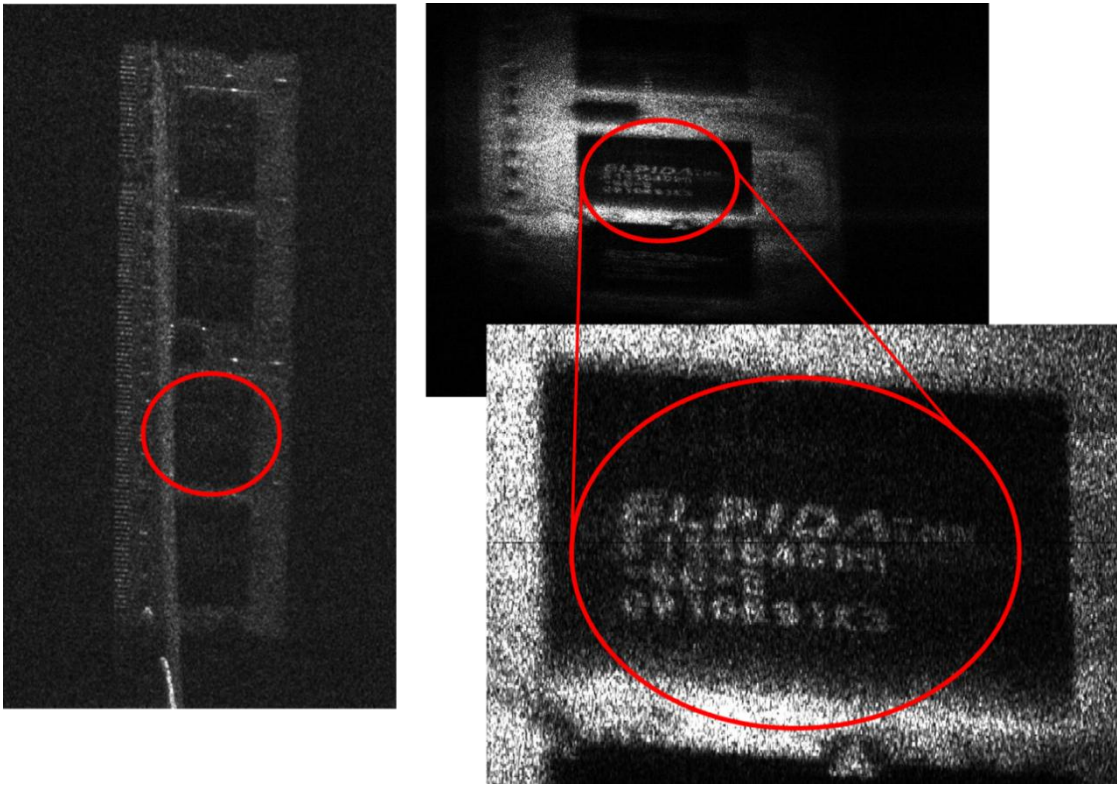


Figure 41: RAM Chip Spotlight Left, the stripmap image of the RAM chip from spotlight mode is shown again for comparison. While the coverage area is much larger, the contrast is lower (lower SNR) and the resolution at the center of the target is poorer than the spotlight image at top right. The spotlight image shows the “spotlight” nature of the illumination and suggests a more complicated focusing (phase error) situation as discussed above with uneven focus over the surface. Bottom right shows a zoom of the spotlight image portion circled in red, the resolution and contrast is enough to read the part number on the top of the integrated circuit! The analogous portion in the stripmap image is circled in red for comparison – no lettering is evident.

## CONCLUSION

### Successes

The success of the PGA algorithm on a diffuse target, the first demonstration of IFSAL, the proof of concept of projective SAL, and spotlight mode demonstrations each provided an excellent learning experience. The foundation of these techniques is the chirp ranging system – the best of its kind. The ability to take the chirp ranging system for granted allowed for a degree of focus on the processing of the collected data.

### Shortcomings

The success of the work in this thesis is limited to the realm of demonstration and study of SAL on an optical bench. A myriad of obstacles exist that prevent SAL from currently performing its stated application in a metrology system. Chief among these is the stripmap photon budget that would require the need for huge optical power to image anything but a small target on an optical bench. While the photon budget for spotlight mode is much more attractive, the mechanics of this system are also more complex. The frequencies employed in SAL make SAL imaging more susceptible to atmospheric conditions than SAR systems. Another shortcoming is the small diversity of targets studied and the long data collection times. The long data collection times could be overcome by using large fiber arrays and faster chirps (some systems with similar bandwidths are now in the 100's of Hz range).

### Prospects for SAL

The future of SAL could be in space reconnaissance as a way to perform high resolution imaging of unknown, foreign satellites. Needless to say this application is far from reality. The basic idea would be to use the wobble of geosynchronous satellites to operate a SAL system in a spotlight mode. SAR systems cannot operate in spotlight mode using the satellite wobble as the provided angles are not large enough. The huge ranges required would allow for a much larger real aperture to be used to collect the data. Even with eased requirement, the optical power required would still be on the order of 1 kW CW laser power.

More practical and short term would be to integrate SAL techniques into a broader industrial metrology system. Bistatic SAL, using multiple receive stations, could be used as a registration tool in large scale metrology systems. A multistatic situation with multiple transmit locations and a means to digitally “stitch” datasets into a larger sampled sets could be a very interesting area for further exploration. The Fractional Fourier Transform operation (which is supported digitally) is a growing area of research that will likely find wider application in synthetic aperture systems. Hopefully the work of this thesis will provide the support necessary for further research to realize how SAL will best be deployed.

## REFERENCES CITED

1. W. G. Carrara, R. S. Goodman, and R. M. Majewski, *Spotlight Synthetic Aperture Radar Signal Processing Algorithms* (Artech House, 1995).
2. Charles V. Jakowatz, Daniel E. Wahl, Paul H. Eichel, Dennis C. Ghiglia, and Paul A. Thompson, *Spotlight-Mode Synthetic Aperture Radar: A Signal Processing Approach* (Springer, 1996).
3. M. Bashkansky, R. L. Lucke, E. Funk, L. J. Rickard, and J. Reintjes, "Two-dimensional synthetic aperture imaging in the optical domain," *Opt. Lett.* **27**, 1983–1985 (2002).
4. P. A. Roos, R. R. Reibel, T. Berg, B. Kaylor, Z. W. Barber, and W. R. Babbitt, "Ultrabroadband optical chirp linearization for precision metrology applications," *Opt. Lett.* **34**, 3692–3694 (2009).
5. Z. Barber, "GOALI: Accurate, High Resolution Ladar for 3D Metrology at Large Standoff Distances," (n.d.).
6. O. M. Ozaktas, Z. Zalevsky, and A. M. Kutay, *The Fractional Fourier Transform with Applications in Optics and Signal Processing*, First (John Wiley and Sons, Ltd., 2001).
7. R. N. Bracewell, *The Fourier Transform and Its Applications*, Third (McGraw Hill, 2000).
8. K. Riley, M. Hobson, and S. Bence, *Math Methods for Physics and Engineering*, Third (Cambridge University Press, 2006).
9. *MATLAB* (Mathworks).
10. B. W. Krause, J. Buck, C. Ryan, D. Hwang, P. Kondratko, A. Malm, A. Gleason, and S. Ashby, "Synthetic aperture ladar flight demonstration," in *Lasers and Electro-Optics (CLEO), 2011 Conference On* (2011), pp. 1–2.
11. Z. W. Barber, C. J. Renner, W. R. Babbitt, R. R. Reibel, P. A. Roos, T. Berg, B. Kaylor, and N. Greenfield, "Linearization of ultra-broadband optical chirps for precision length metrology," in *2010 Conference on Lasers and Electro-Optics (CLEO) and Quantum Electronics and Laser Science Conference (QELS)* (IEEE, 2010), pp. 1–2.

12. S. M. Beck, J. R. Buck, W. F. Buell, R. P. Dickinson, D. A. Kozlowski, N. J. Marechal, and T. J. Wright, "Synthetic-aperture imaging laser radar: laboratory demonstration and signal processing," *Appl. Opt.* **44**, 7621–7629 (2005).
13. M. Bashkansky, "Synthetic aperture imaging at 1.5 $\mu$ : laboratory demonstration and potential application to planet surface studies," in (SPIE, 2002), Vol. 4849, pp. 48–56.
14. Goodman, Joseph W., *Introduction to Fourier Optics*, Third (Viva Books Private Limited, 2007).
15. P. Hobbs, *Applied Optics* **36**, 903–920 (1997).
16. P. Hobbs, "Reaching the Shot Noise Limit for \$10," *Optics and Photonics News* (1991).
17. A. V. Jelalian, *Laser Radar Systems* (Artech House, 1992).
18. M. Budge, "EE 710 - ST: Radar Waveforms and Signal Processing," (Spring 2011).
19. Wikipedia contributors, "Aluminium," *Wikipedia, the free encyclopedia* (2012).
20. Wikipedia contributors, "Fused quartz," *Wikipedia, the free encyclopedia* (2012).
21. J. R. Fienup and J. J. Miller, "Aberration correction by maximizing generalized sharpness metrics," *J. Opt. Soc. Am. A* **20**, 609–620 (2003).
22. Dennis C. Ghiglia and Mark D. Pritt, *Two-Dimensional Phase Unwrapping: Theory, Algorithms, and Software* (Wiley-Interscience, 1998).
23. B. Luong, *Contantini's 2D Unwrapping Based on Minimum Network Flow* (ESA, 2009).
24. M. Costantini, "A novel phase unwrapping method based on network programming," *Geoscience and Remote Sensing, IEEE Transactions on* **36**, 813 – 821 (1998).
25. K. Garrard, *Plot3k* (2005).
26. David A. Yocky, D. E. Wahl, and C. V. Jakowatz Jr., "Spotlight-Mode SAR Image Formation Utilizing the Chirp Z-Transform in Two Dimension," (2006).
27. G. D. Martin, "Chirp Z-Transform Spectral Zoom Optimization with MATLAB," (2005).

28. R. L. Allen and D. W. Mills, *Signal Analysis - Time, Frequency, Scale, and Structure* (Wiley - IEEE Press, 2004).

APPENDIX A

MATLAB CODE

## APPENDIX A: MATLAB CODE

Note – all code written in MATLAB release 2011b or previous.

SAL Data Collection Code (With Fiber Array)

Used for the data collection process of taking a SAL image.

```

% SAL Data Capture and Image Processor - Collection for fiber array
% Zeb Barber / Stephen Crouch
% 1/18/12
%
% Scene is stepped with a Zaber stepper motor - some basic data processing is done during this part
%
% Post processing to be done in other m files

% Suggestion: Use RealTimeRange_for_peaking to estimate the range
% window of the scene to use in range_index_min/max
%% Open Serial Port to Zaber Motor and Initialize
%Zaber has an extensive wiki supporting their stepper motor controllers
%including the model used, the T-MCA see zaber.com/wiki/Manuals

%See if the port is already open
if exist('sr1','var')
    fclose(sr1)
    display("Serial initialized")
    clear
end

%Open Serial Port
sr1 = serial('com6','BaudRate',9600,'RequestToSend','off','TimeOut',5); %usb to serial is com6
fopen(sr1);
StepSize = 128;

%Various Zaber serial Commands
command_renumber = [0 2 0 0 0 0];
command_set_res1 = [1 37 StepSize 0 0 0];
command_home1 = [1 1 0 0 0 0];
command_store_pos1 = [1 16 3 0 0 0];
command_goto_stored1 = [1 18 3 0 0 0];
command_store_pos = [1 16 3 0 0 0];
command_stop = [1 23 0 0 0 0];

%Set device mode
fwrite(sr1,command_renumber,'int8');
pause(1)
fwrite(sr1,[1 40 0 8 0 0]);

fwrite(sr1,command_set_res1,'int8');
```

```

%set running current 38, hold current 39, target speed 42,
%and acceleration 43
pause(1);
fwrite(sr1,[1 38 80 0 0 0], 'int8');
fwrite(sr1,[1 39 1 0 0 0], 'int8');
fwrite(sr1,[1 42 255 8 0 0], 'int8');
fwrite(sr1,[1 43 16 0 0 0], 'int8');

%Move to set position
CurPos1 = Move_Absolute_Dev(500000,sr1,1);

%if the ports get clogged up try "delete(instrfindall)" might help?
%% Set up Variables
% *Some other basic setup...*

%here are the 2 important parameters to check number of shots and cross
%range spacing between them step_spacing is the number of microns
%the stage will shift in cross range so think about these to make
%sure the stage wont crash...

%number of shots and the step size
N_shots = 2048;
step_spacing = 26; %step_spacing times 390nm gives the step (in this case roughly 10 micron steps)

cj = sqrt(-1); % imaginary number

DTIN.Tread = 300e-3;
DTIN.fs_ADC = 5e6/3; % sample rate (Hz)
DTIN.VertRange = 1; % Peak to Peak voltage
DTIN.N_Read = DTIN.Tread*DTIN.fs_ADC;
boolsave = 0;

t = (1:DTIN.N_Read)/DTIN.fs_ADC; %time axis

f = linspace(0,DTIN.fs_ADC/2,DTIN.N_Read/2);
f = [f -f(end:-1:1)]; %freq axis

R = f/10e12*3e8/2; %range axis

pad_length=2^(ceil(log2(DTIN.N_Read)));

%where is the hcn peak in time (upper and lower lims) ??? this can be viewed in
RealTimeRane_for_peaking
hcn1 = .017;
hcn2 = .019;

%setup the appx location where the scene(s) will be in the range - we will
%only want to include this subset in the pre-processed data

length_index_scale=length(R)/R(end/2)/2; %points in R divided by max range

```

```

range_index_min_1=6.0e4;           %closest scene point (in indices)for first fiber array
range_index_min_2=5.95e4;        %closest to second channel fiber array scene locations

range_index_max=range_index_min + 2048;           %furthest scene point
range_index_width=2^(ceil(log2(range_index_max-range_index_min))); %2^n length section of range to
keep

RR = R;
R_1=R(range_index_min_1:(range_index_min_1+range_index_width-1));
R_2=R(range_index_min_2:(range_index_min_2+range_index_width-1));
%% Put the Zaber in Position
%it is important in this step to keep an eye on the zaber to make sure it does not self destruct!!
%it sets a current position and then moves the entire distance of the scan,
%in the next cell the program will step back across this distance to the
%saved "current position"

%during this it will move appx 25.64*step_spacing*10e-3 (this will give
%distance in mm it will travel)
zC = 1;
%some more zaber initials - moving to where the scan will start
MoveAmountX = +1;
saveData = 0;
reply = setPosition(500000, sr1,1);
CurPos1 = 500000;
CurPos1 = Move_Absolute_Dev(500000-round(zC*step_spacing*N_shots/2)-1000,sr1,1)
CurPos1 = Move_Absolute_Dev(500000-round(zC*step_spacing*N_shots/2),sr1,1)
pause(.75)
%CurPos1 = Move_Absolute_Dev(back to above number if needed...,64,sr1,1)

%% Collect the Data (this will take at least (N_Shots/60) minutes)

%Window for the big range profile (hann) and pre-allocation of memory for
%saving data
hwin = hann(DTIN.N_Read-2e4);
Range_Comp_Mat = zeros(2048,N_shots,2);
HCN_all = zeros(length((find(t>=hcn1,1,'first')-1e4):(find(t>=hcn2,1,'first')+1e4)),N_shots);

for kk=1:N_shots;

    %step counter ... to keep you from going crazy...
    if(mod(kk,10) == 0)
        kk
    end

    %Data collection
    BothCh = FastAcDualCh(DTIN.N_Read,['test','bin'],boolsave,DTIN.VertRange,DTIN.fs_ADC,1);
    Trigger_HCN = BothCh(1:DTIN.N_Read); %series of peaks in HCN spect. one will be used as
trigger
    Range = BothCh(DTIN.N_Read+1:end); %return signal on the detector

    %step the motor to move to the next aperture location...this is done while

```

```

    %some FFTs can take place...
    try
        CurPos1 = Move_Absolute_Dev(500000-
round(zC*step_spacing*N_shots/2)+round(zC*step_spacing*kk),sr1,1);
    catch

    end

    % everything below is processing this shot while the zaber is moving...

    %Find index of HCN Peak using a fit to a Lorentzian function
    HCNfit = Trigger_HCN(find(t>=hcn1,1):find(t<=hcn2,1,'last'));
    tfit = 10000*(t(find(t>=hcn1,1):find(t<=hcn2,1,'last'))-hcn1);

    [beta_V,rV,JV] = fitnonlin(tfit,HCNfit,'lorentzfit',[tfit(find(HCNfit == max(HCNfit),1)) 0 max(HCNfit)
.25e12/10e12]);
    delta_beta_V = nlpardelta(beta_V,rV,JV);

    Tpeak_V(kk) = beta_V(1)/10000+hcn1;
    Shift(kk) = -(floor(Tpeak_V(kk)*DTIN.fs_ADC)-find(t>=hcn1,1));
    HCNfit1 = lorentzfit(beta_V,tfit);

    %plot the HCN peak to see if it is fitting ok...
    if kk==1;
        figure(40)
        clf
        H40a = line(tfit, HCNfit);
        H40b = line(tfit, HCNfit1);
        drawnow
    else
        set(H40a, 'ydata', HCNfit);
        set(H40b, 'ydata', HCNfit1);
        drawnow expose
    end

    %Circshift to align this range data with the HCN peak...
    Range = circshift(Range,Shift(kk));

    %Keep trigger_hcn data for later analysis...if there is a problem with
    %phasing it could be caused by the HCN fit not working so this would be
    %what to look at to check...
    Trigger_HCN = circshift(Trigger_HCN, Shift(kk));
    HCN_all(:,kk) = Trigger_HCN((find(t>=hcn1,1,'first')-1e4):(find(t>=hcn2,1,'first')+1e4));

    % Shift and Cut out range portion
    Range_Comp = fft(Range((1e4+1):end-1e4).*hann(length(Range((1e4+1):end-1e4))));

```

```

%cut out the range data of interest for the two channels
Range_Comp_1=Range_Comp((range_index_min_1):(range_index_min_1+range_index_width-1));
Range_Comp_2=Range_Comp((range_index_min_2):(range_index_min_2+range_index_width-1));

%Plot the cut out Range data to make sure we are capturing the sections
%of interest
if kk==1;
figure(59)
clf
R59 = line(R_1, 20*log10(abs(Range_Comp_1)));
drawnow
else
set(R59, 'ydata', 20*log10(abs(Range_Comp_1)));
drawnow expose
end

if kk==1;
figure(60)
clf
R59 = line(R_2, 20*log10(abs(Range_Comp_2)));
drawnow
else
set(R59, 'ydata', 20*log10(abs(Range_Comp_2)));
drawnow expose
end

%keep range compressed data for post processing
Range_Comp_Mat(:,kk,1) = Range_Comp_1;
Range_Comp_Mat(:,kk,2) = Range_Comp_2;

pause(.5)
end
%%
Return

```

### Phase to Retro Code

Used for phase correction of scenes with retro-reflector cooperative targets.

```

%Import the raw data
S1 = Range_Comp_Mat(:,1:2048,1);
S2 = Range_Comp_Mat(:,1:2048,2);
S1 = R1(:,1025:end);
S2 = R2(:,1025:end);
% delete R1 R2;

%Make a copy of each dataset
S1p = S1;
for nn = 1:n
    %Find the peak of the retro in each shot and zero everything but that
    %point in the copy dataset
    [k,l] = max(S1p(:,nn));
    S1p(1:l-2,nn) = 0;
    S1p(l+2:end,nn) = 0;
end
%FT the set and its copy, divide the two and FT back. This process makes
%the phase at each retro point the same for all shots
S1 = fft(fft(S1,[],1)./exp(1i.*angle(fft(S1p,[],1))),[],1);

S2p = S2;
for nn = 1:n
    [k,l] = max(S2p(:,nn));
    S2p(1:l-2,nn) = 0;
    S2p(l+2:end,nn) = 0;
end
S2 = fft(fft(S2,[],1)./exp(1i.*angle(fft(S2p,[],1))),[],1);

%Compress the image in cross range, it is now focused
S1 = fftshift(fft(S1,[],2));
S2 = fftshift(fft(S2,[],2));

```

## Phase Gradient Autofocus Code

Used for phase correction of non-cooperative scenes.

```

function [imag, fimag, PhiTotal] = PGAforSAL(fScene2,lr,ur,maxiter,hwin)
% [imag, fimag, PhiTotal] = PGAforSAL(fScene2,lr,ur,maxiter,hwin)
% imag = corrected complex image
% fimag = range-compressed data of corrected image
% PhiTotal = total phase correction
% fScene2 = range-compressed (not cross range compressed) data of uncorrected image
% the range dimension has to be in the rows and the crossrange in the
% columns so that imagesc gives vertical for range domain and horizontal
% for crossrange domain
% lr = lower range of area of scene to use for PGA
% ur = upper range of area of scene to use for PGA
% maxiter = maximum number of iterations
% hwin = initial window size
% This function runs the PGA algorithm on a SAL scene that has already had
% its range migration fixed

Scene2 = fftshift(fft(fScene2,[],2),2); % form the unfocused image
[N,M] = size(Scene2); %get the size of the dataset
hwid = floor(M/4);
Scene3 = Scene2*0; %make an empty matrix with dimensions of the dataset
i=sqrt(-1);

for nn = 1:maxiter %iterates until a max phase correction is met

    [r,m] = max(abs(Scene2.')); %find the brightest scatterer at each range

    for jj = 1:N
        %shift all scatterers to the center
        Scene3(jj,:) = fftshift(circshift(Scene2(jj,:),[0 (-m(jj))]));
    end

    if nn == 1
        hwid = hwin;
    else
        hwid = floor(hwid/2); % cuts the window width in half for next iteration
    end

    if hwid < 4 %break the iteration if the window size is getting too small
        disp('hwid < 4')
        break
    end

    Scene3(:,[1:(M/2-hwid) (M/2+hwid):end]) = 0; % window down the circshifted data

    Scene3(:,(M/2-hwid):(M/2+hwid)) = Scene3(:,(M/2-hwid):(M/2+hwid));

```

```

fScene4 = fft(fftshift(Scene3,2),[],2); % FT the windowed data
%compute the derivative across the cross range dim, sum in range, and
%find the angle
DPhi = angle(sum(conj(fScene4(lr:ur,1:(end-1))).*fScene4(lr:ur,2:end)));

%   DPhi = DPhi-mean(DPhi);

PhiComp = [0 cumsum(DPhi)]; % integrate to find the phase estimate
%attempt to remove the linear shift
PhiComp = PhiComp - polyval(polyfit([1 M],PhiComp([1 M]),1),1,1:M);

if nn == 1
    PhiTotal = PhiComp;
else
    PhiTotal = unwrap(PhiTotal + PhiComp); %find the unwrapped cumulative phase correction
end

if (max(PhiComp)-min(PhiComp)) < pi/10
    disp('Phase Correction less than pi/10') %break if the correction is too small
    break
end

for kk = 1:M
    fScene4(:,kk) = fScene2(:,kk).*exp(-i*PhiComp(kk)); %apply the phase correction
end

Scene4 = fftshift(iff(fScene4,[],2),2); %form the new focused image

Scene2 = Scene4;
fScene2 = fScene4;
%display the iteration number
nn
end
imag = Scene4; %the image and the FT of the image for export...
fimag = fScene4;

```

Correlation for Registration Code

Used to register SAL images for IFSAL processing.

```

%Imag intensity
S1a = abs(S1).^2;
S2a = abs(S2).^2;
%Correlation
S12a = ifft2(fft2(S1a).*conj(fft2(S2a)));
%Estimate shift for proper registration shift
[row,col] = find(fftshift(abs(S12a).^2) == max(max(abs(S12a).^2)))

```

Shift for Registration Code

Used to shift SAL images for IFSAL processing.

```

function [imgshift] = imagshift(img,x,y)

[n,m] = size(img); %image size
fimg = fft2(img); %transform of image

[M,N] = meshgrid(1:m,1:n); %set up matrix for shift

fimgshift = fimg.*exp(-1i*2*pi*x*N/n).*exp(-1i*2*pi*y*M/m); %shift the matrix in frequency domain
imgshift = ifft2(fimgshift); %Transform back

```

IFSAL Code

Used to remove flat earth effect, interfere, and filter images for IFSAL processing.

```

%Forming the Interferogram
[M,N] = size(S1);

%Tilting in x and y to remove flat earth effect
scale_x = .154; %x scale
x = scale_x.*(0:M-1)';
scale_y = -0.003;
y = scale_y.*(0:N-1); % y scale
ramp = repmat(exp(1i*2*pi.*x),1,N).*repmat(exp(1i*2*pi.*y),M,1); %tilt operation
%ramp = 1; %useful to form interferogram without flat earth removed

% Interfere and then filter the phase according to Ghiglia's suggestion
A = angle(S1.*ramp.*conj(imagshift(S2,.8,.5))); % interfere
IM = imfilter(sin(A),ones(10,10));%filter this and next three lines
RE = imfilter(cos(A),ones(10,10));
Wrapped = atan2(IM,RE);
Wrapped = fliplr(Wrapped);

```

## Least Squares Unwrap Code

Used to unwrap IFSAL interferograms.

```
%Least Squares formulation for Phase Unwrapping (Ghiglia / Jakowatz)
```

```
% Load stuff
% Wrapped = load('mat');
% Wrapped = Wrapped.Wrapped;
% Wrapped = wrapToPi(wrapToPi(peaks')); %%% to prove that this works
```

```
%Computes the driving function from the wrapped phase and finds the least
%squares solutions (unwrapped phase) as a discrete solution to Poissons
%Equation
```

```
[M,N] = size(Wrapped);
```

```
% take a bunch of derived matrices based on the Ghiglia / Jakowatz write
% ups
```

```
Del_X_ij = wrapToPi ( circshift(Wrapped, [0 2]) - circshift(Wrapped, [0 1]));
Del_X_imj = wrapToPi ( circshift(Wrapped, [0 1]) - circshift(Wrapped, [0 0]));
Del_Y_ij = (wrapToPi ( (circshift(Wrapped, [2 0]) - circshift(Wrapped, [1 0]))));
Del_Y_imj = (wrapToPi ( (circshift(Wrapped, [1 0]) - circshift(Wrapped, [0 0]))));
```

```
%zero the borders of the dels...as the algorithm describes
```

```
Del_X_ij(1,:) = 0 ;Del_X_ij(end,:) = 0;
Del_X_imj(1,:) = 0 ;Del_X_imj(end,:) = 0;
Del_Y_ij(:,1) = 0 ;Del_Y_ij(:,end) = 0;
Del_Y_imj(:,1) = 0 ;Del_Y_imj(:,end) = 0;
```

```
%%% find the driving function and 2DDCT
```

```
pij = (Del_X_ij - Del_X_imj) + (Del_Y_ij - Del_Y_imj);
```

```
pij = dct2(pij);
```

```
% modify the driving function accordingly
```

```
ii = 1:M;
jj = 1:N; jj = jj';
Mod = repmat(cos(pi.*ii/M),N,1)+ repmat(cos(pi.*jj/N),1,M) - 2;
pij = pij./2./Mod';
```

```
% inverse transform to find the unwrapped phase
```

```
Unwrapped = idct2(pij);
```

Projective SAL Code

Used to for PSAL image from two projections.

```
%% Form the Image
```

```
%After previous focusing and registration steps, the images can be formed
%The gist here is to keep points in three dimensions that would project
%into BOTH of the SAL images
%This unfortunately is done with a series of ugly for loops but
%does not take more than few minutes to computer on a quad core
```

```
[m,n] = size(Flat_1);
```

```
%allote some space for this large matrix
```

```
Scatter = zeros(m,n,50);
```

```
for kk = 1:m
```

```
  for jj = 1:n
```

```
    if Flat_1(kk,jj)==1; %Does it project into the flat plane?
```

```
      bb=0;
```

```
      for gg=10:10:n
```

```
        if Side_1(kk,gg)>0 %Does it project into the side plane?
```

```
          bb=bb+1;
```

```
          Scatter(kk,jj,bb)=gg; %Given the flat plane coordinates, keep the height in the side plane
```

```
        end
```

```
      end
```

```
    end
```

```
  end
```

```
end
```

```
% Save the x,y, and z locations in three corresponding arrays to plot
```

```
Px=[];
```

```
Py=[];
```

```
Pz=[];
```

```
count=0;
```

```
for kk = 1:m
```

```
  for jj = 1:n
```

```
    for bb=1:50;
```

```
      if Flat_1(kk,jj)>0;
```

```
        count=count+1;
```

```
        %save xyz coordinates of nonzero points
```

```
        Px(count)=kk;
```

```
        Py(count)=jj;
```

```
        Pz(count)=Scatter(kk,jj,bb);
```

```
      end
```

```
    end
```

```
  end
```

```
end
```

```
figure(1);  
hold off
```

```
%plot using plot3k - a nice mathworks contributed file for plotting  
plot3k([Px ; Py ; Pz])  
grid on
```

## Chirp Z-Transform Polar Format / Bistatic Correction Code

Used to polar format and correct Monostatic / Bistatic Spotlight images.

```

%Upload data and uncompress range dimension
Polar = (fft(Range_Comp_Mat(:,1),[],1));

%Pick out middle half of shots - they are less affected
Polar = Polar(:, 512:(1023+512));

[R,C] = size(Polar);

theta = -1.*asin(((511:1:512)).*54e-6./1.57); %step spacing - shot times step increment divided by range
to target 30 micron orig.
Rfront = 1.57-700.*3e8/2/1.5224e12+.01; %front of the scene in range
Rback = Rfront+(R-700).*3e8/2/1.5224e12-.01; %number of range indices times pixel res to get furthest
range possible (the back of the scene)

%Range Migration Correction Loop

%central frequency that serves as the starting point of the contour for the chirp z
ffront = R*Rfront/(Rback*cos(theta(512))-Rfront*cos(theta(512)));

for nn = 1:C;

    f1 = R*(Rfront)/(Rfront.*(cos((theta(nn)-theta_B)/2))-Rback.*cos((theta(nn)-theta_B)/2)); %scaled front
    frequency
    f2 = R*(Rback)/(Rfront.*(cos((theta(nn)-theta_B)/2))-Rback.*cos((theta(nn)-theta_B)/2)); %scaled back
    frequency

    Polar(:,nn) = czt(Polar(:,nn), R, exp(-1i*2*pi*(f2-f1)/(R*R)),exp(1i*2*pi*2*ffront)); %use the czt to
    zoom between two freqs above
end

figure(55);
imagesc(abs(Polar)) %plot to make sure things didn't get crazy!
%% PGA Loop - Cross Range then Range, two times...
%Cross range is the typical PGA
%Range PGA corrects the bistatic issues discussed in spotlight chapter...

[PGA_Image, fPGA_Image] = PGAforSAL (Polar, 735, 930, 55, 511);
[PGA_Image2, fPGA_Image, dphi] = PGAforSAL (fft(PGA_Image',[],2), 1, 1024, 55, 1023);
[PGA_Image2, fPGA_Image, dphi] = PGAforSAL (fftshift(fft(PGA_Image2',[],2),1), 735, 930, 55, 511);
[PGA_Image2, fPGA_Image, dphi] = PGAforSAL (fftshift(fft(PGA_Image2',[],2),1), 1, 1024, 55, 1023);

%take a look at the image
figure(156); imagesc((fftshift(imfilter(abs(PGA_Image2').^2,ones(1,1)),1)),[0 6e4]); colormap gray; axis
xy

```